

# RARE-EARTH AND TRACE ELEMENTS OF THE LOWER CAMBRIAN–LOWER CRETACEOUS SILICICLASTIC SUCCESSION OF NE GONDWANA IN JORDAN: FROM PROVENANCE TO METASOMATISM

Belal S. AMIREH<sup>1,\*</sup> , Ghazi A. SAFFARINI<sup>1</sup> , Mazen N. AMAIREH<sup>2</sup> ,  
Ghaleb H. JARRAR<sup>1</sup>  & Abdulkader M. ABED<sup>1,3</sup> 

<sup>1</sup> Department of Geology, University of Jordan, Amman, 11942 Jordan;

e-mails: [bamireh@ju.edu.jo](mailto:bamireh@ju.edu.jo); [ghasaff@ju.edu.jo](mailto:ghasaff@ju.edu.jo); [ghalebjarrar@ju.edu.jo](mailto:ghalebjarrar@ju.edu.jo)

<sup>2</sup> Department of Mining Engineering, Tafila Technical University, Tafila, Jordan;

e-mail: [mazenamaireh@ttu.edu.jo](mailto:mazenamaireh@ttu.edu.jo)

<sup>3</sup> Passed away on August 8, 2021

\* Corresponding author

Amireh, B. S., Saffarini, G. A., Amaireh, M. N., Jarrar, G. H. & Abed, A. M., 2022. Rare-earth and trace elements of the lower Cambrian–Lower Cretaceous siliciclastic succession of NE Gondwana in Jordan: from provenance to metasomatism. *Annales Societatis Geologorum Poloniae*, 92: 109–158.

**Abstract:** The present bulk-rock geochemical study aims to answer some questions concerning the distribution and variability of trace elements (TEs) and rare earth elements (REEs) in the lower Cambrian–Lower Cretaceous sandstones and mudstones of NE Gondwana in Jordan. The study proved that the REE and the TE distribution patterns in both detrital and authigenic, light and heavy minerals are controlled principally by the source-rock provenance, followed by an interplay of many factors: chemical weathering, recycling, hydraulic sorting, locally low-temperature, hydrothermal metasomatism, depositional environment and redox conditions, and diagenesis. On the basis of specific trace elements, trace-element ratios, and petrographic proxies, the provenance is constrained to be mainly felsic-, rarely mafic granitoids of the Arabian-Nubian Shield, and less commonly, recycled Palaeozoic and Mesozoic siliciclastic strata. REEs are hosted mainly in zircon, Ti-bearing minerals, and partly in clay minerals. They were depleted by both chemical weathering and recycling; nevertheless, they were enriched by subsequent hydraulic sorting and low-temperature, hydrothermal metasomatism. Chemical weathering initially depleted zirconium. However, this was counteracted by subsequent enrichment through recycling, hydraulic sorting, and low-temperature, hydrothermal metasomatism. The fractionation of the other TEs, due to these sedimentological factors during the genesis of subarkosic arenites, quartz arenites and mudstones, is discussed and some conclusions are derived. The Eu negative anomaly was enhanced significantly by recycling and low-temperature, hydrothermal metasomatism. Scandium abundance increased with decreasing grain size from coarse sand to the mud fraction. The recorded REE and TE fractionation might also apply to siliciclastics in similar, geological environments.

**Key words:** Jordan, NE Gondwana, rare-earth and trace elements, fractionation, provenance proxies, Arabian-Nubian Shield, siliciclastics.

*Manuscript received 29 May 2021, accepted 30 March 2022*

## INTRODUCTION

The chemical composition of siliciclastic sediments and sedimentary rocks in general and the concentrations of rare-earth elements (REEs) and trace elements (TEs) in particular are controlled by several factors. These are important factors, such as provenance source rocks and tectonic setting, climate-dependent weathering, recycling, hydraulic sorting during transport and deposition, depositional

environment and redox conditions, diagenesis, very low-grade metamorphism and low-temperature, hydrothermal metasomatism.

The elements with high field strength, Zr, Hf, Y, Nb, Th, and U, and the REEs are incompatible elements that preferentially partitioned into melts during crystallization and anatexis (magmatic processes; Feng and Kerrich, 1990) and

consequently they are enriched in felsic rocks. On the other hand, the transition metals, Cr, V, Co, Ni and Sc, behave compatibly during processes of magmatic fractionation and become enriched in mafic to ultramafic rocks. Therefore, the ratio of incompatible to compatible elements, such as Zr/Sc, La/Sc, Th/Sc, and Th/Co, heavy REE/ light REE, and the value of the negative Eu anomaly can be used as proxies for sediment provenance (Cullers, 1995). Ali *et al.* (2014) recently have confirmed this inference, assuming that the ratios of the trace elements, Zr, Hf, Sc, Y, Cr, Th and Co and REEs, in siliciclastic, sedimentary rocks behaved as a closed system during weathering, transport, deposition, and diagenesis, and can be used to recognize the tectonic setting and provenance of their host rocks. This implicit assumption will be taken into consideration in the present study.

From another point of view, during weathering, some of the elements might be mutually fractionated (Feng and Kerrich, 1990), thus impairing their use as provenance proxies. Those elements that are very mobile during weathering, transportation, and sedimentation are the large ion, lithophile elements, Rb, Cs, Ba, and Sr, besides Ca, Na, K, Mg, and Si. On the other hand, other elements are relatively immobile in the water-rock system during weathering, transportation, and deposition. Immobility of elements means that they are not mobilized during chemical weathering and therefore are retained in the refractory minerals, such as zircon and rutile, or are absorbed by clay minerals, accumulating in the weathering residue. These immobile elements include the elements of high field strength (Zr, Hf, Y, Nb), some transition elements (Cr, V, Co, Ni, Sc, Ta), and the REEs. These elements were generally transported (within their hosting minerals) from the sites of weathering of the source rocks to the sites of deposition as a suspended load (in the solid phase) with little chemical alteration. Therefore, taking into account the above-mentioned assumption, they can be used for the interpretation of provenance (Taylor and McLennan, 1985; Bhatia and Crook, 1986; Roser and Korsch, 1986, 1988; Condie, 1993; Ali *et al.*, 2014).

Many questions remain unanswered regarding the distribution of the REEs and TEs in siliciclastic, sedimentary rocks. Among these, is the bulk of REEs accommodated in the clay and silt size fractions (Taylor and McLennan, 1985; Condie, 1991)? Are significant amounts of REEs and some TEs contained in zircon and other minor heavy minerals (Cullers *et al.*, 1979)? Do the REE content, pattern, and Eu anomaly values of sandstones differ from those of mudstones (Cullers, 1994; Lawrence *et al.*, 2011)? Is there a difference in the REE and TE contents of sedimentary rocks adjacent to uplifted continental blocks and the shelf siliciclastics, distal with respect to these blocks (Cullers, 1994; Basu *et al.*, 2016)?

The lower Cambrian–Lower Cretaceous siliciclastic succession of Jordan represents the basis for a unique case study to assess the factors, controlling the REE and TE contents of sandstones and mudstones. This is because it has a large thickness (ca. 2,000 m), spans a long, geologic time interval from the early Cambrian to the Late Cretaceous, and received detritus from several provenance terranes under different tectonic settings and climates, and was deposited

in numerous environments. Only a few studies have dealt with some of the REEs and TEs in different parts of this siliciclastic succession (Amireh, 1993; Amireh *et al.*, 1998; Jarrar *et al.*, 2000). Thus, the present study represents the first, systematic documentation of the concentration of REEs and TEs in the lower Cambrian–Lower Cretaceous siliciclastic succession of Jordan. Recently, Amireh (2020) published a detailed study of the petrography and major-element geochemistry of this siliciclastic succession. However, he noted that the provenance was mainly the Neoproterozoic Arabian Shield, without constraining the actual types of the provenance source rocks.

Therefore, the present work aims to interpret the fractionation of REEs and TEs in the sandstones and mudstones in terms of chemical weathering, recycling, hydraulic sorting, diagenesis and very low-grade metamorphism/low-temperature, hydrothermal metasomatism, with reference to the lower Cambrian–Lower Cretaceous siliciclastic succession of Jordan. Determining where the REEs and the TEs occur and how to constrain the types of provenance source rocks, utilizing the REEs and the TEs content, thus complementing the results of major-element geochemistry (Amireh, 2020), represent other aims of the study.

## GEOLOGICAL SETTING

About 2,000-metre thick, the lower Cambrian–Lower Cretaceous siliciclastic succession with subordinate carbonates and evaporites crops out in certain parts of Jordan (Fig. 1). The siliciclastic succession consists of the lower Palaeozoic strata (Cambrian and Ordovician systems, and Silurian Llandovery Series), and the Lower Cretaceous. The lower part of this succession constitutes a segment of the immense lower Palaeozoic siliciclastic sheet, bordering most of the northern Gondwana margin (Amireh, 2018).

The Cambrian System rests unconformably on the late Neoproterozoic basement rocks of the Aqaba and the Araba complexes of the Arabian Shield, formed during the Pan-African thermo-tectonic event of the Neoproterozoic Gondwana amalgamation. The Cambrian deposits consist mainly of fluvial sandstone, deposited by northward-flowing, braided rivers (Fig. 1), with subordinate, shallow-marine, fine sandstones (Amireh *et al.*, 1994a; Amireh, 2018). The conformable Ordovician System starts with fluvial sandstones, deposited by similar, northward-flowing, braided rivers with interbedded, shallow-marine sandstones, containing *Cruziana* and *Skolithos* (Amireh *et al.*, 2001). Deeper, marine deposits, fluctuating between the intertidal, shoreface and offshore zones, characterize the middle and upper parts of the Ordovician and lower part of the Silurian System. Glacial sediments were deposited in the Late Ordovician during a regional, glacial event (Abed *et al.*, 1993). The other parts of the Silurian System as well as the Devonian and the Carboniferous systems are not present in Jordan (Bender, 1968), owing to their truncation during the Carboniferous Hercynian orogeny (Saint-Marc, 1978).

The Triassic and Jurassic Systems consist of carbonates and evaporites, with minor, fluvial and shallow-marine sandstones and mudstones, from which some mudstone samples were taken. The Lower Cretaceous Kurnub Group consists

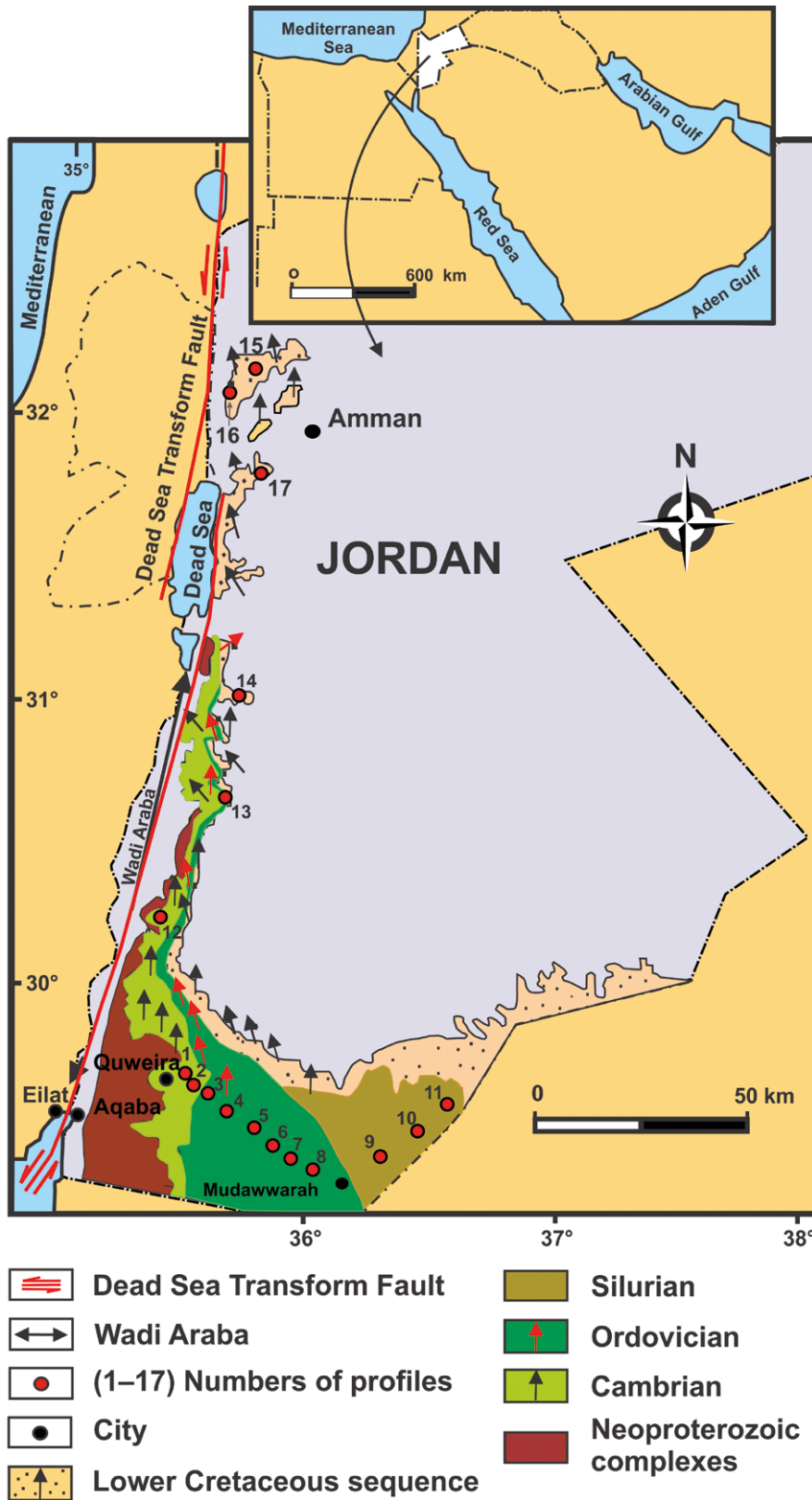


**Fig. 1.** Simplified geological map of Jordan showing positions of the studied profiles (1–17), and palaeocurrent directions in the Cambrian and Ordovician Systems, and the Lower Cretaceous Series. 1 – Salab Fm in Salab mud flat (SR1-10), 2 – Umm Ishrin Fm (UI1-17), 3 – Disi Fm in Disi mud flat (DS1-15), 4 – Umm Saham Fm in Umm Saham area (US1-12), 5 – Hiswa Fm in Wadi Hiswa (H1-9), 6 – Dubaydib Fm in Dubaydib area (D3-23), and Mizrab area (DMZ 1-13), 7 – Tubailiyat Mb of the Mudawwarah Fm in Tubailiyat area (TB1-13), 8 – Ammar Mb of the Mudawwarah Fm in Jabal Ammar area (AM1-8), 9 – Batra Mb of the Mudawwarah Fm (BT2-6), and Bir Fa’as Fm of the Kurnub Group (KG) in Batra area (BF10S), 10 – Ratya Mb of the Mudawwarah Fm in Ratya area (RS3-11). 11 – Khusha Fm in Khusha area (KH1-3), 12 – Abu Khusha Fm in Wadi Abu Khusha (AK2-15), 13 – Salab Fm in Dana area (SD1-9), 14 – Karak Fm of the KG in Wadi el Karak (K1-3), 15 – Jarash Fm (J25) and Bir Fa’as Fm (BF1) in Jarash area, 16 – Ramel Fm of the KG in Arda area, 17 – Hammat Fm of the KG in Mai’n area (HM8).

of fluvial sandstones, deposited by a braided, low sinuosity, meandering river, flowing northward from the Arabian Shield to the Neo-Tethys and overlain by shallow-marine sandstones and carbonates (Amireh, 1997, 2000; Amireh and Abed, 1999). Carbonates, evaporites, bedded cherts, bituminous limestones, and phosphorites constitute the Upper Cretaceous–upper Eocene series.

The tectonic development of Jordan began with the late Neoproterozoic Pan African thermo-tectonic event that was terminated by an extensional rifting phase and isostatic uplift with associated erosion of parts of the late Neoproterozoic Aqaba and Araba complexes, giving rise to the regional Rum Unconformity (Powell *et al.*, 2014). Tectonic quiescence characterized the study area from the middle Cambrian to middle Carboniferous. However, a thermo-tectonic event is documented west of the study area in the Middle/Late Devonian (Segev *et al.*, 1995; Vermeesch *et al.*, 2009). In the late Carboniferous, Jordan was affected by another regional, thermo-tectonic event that gave rise to a giant, domal uplift, “the Geanticline of Heletz” (Gvirtzman and Weissbrod, 1984). It was associated with rifting and concomitant erosion, responsible for the truncation of the entire Carboniferous and Devonian, and parts of the Silurian and Ordovician, and giving rise to a N–S-oriented strip of outcrops of the Cambrian–Ordovician in Jordan (Fig. 1). Rifting, associated with the opening of the Neo-Tethys Ocean (Stephenson and Powell, 2013) as well as several tectonic uplifts associated with erosion, affected the study area between the Permian and the Late Jurassic and were responsible for several unconformities (Amireh, 2018); meanwhile, in the Early Cretaceous, tectonic quiescence predominated.

## METHODS AND TERMINOLOGY

Fifty-eight friable and semi-indurated sandstone samples, representing the lower Cambrian–Lower Cretaceous siliciclastic succession, and 12 mudstone samples were collected from 17 profiles (Fig. 1). The easting and northing of each sample using GPS map 60CSx are listed in Table 1. Some samples have the same GPS coordinates, since they are taken from the same profile but at different elevations (or vertical positions). It is emphasized that the samples were completely fresh and not affected by recent weathering, which was achieved by removing the outer weathering surface in all cases. This was to assure that the samples were not affected by present-day weathering that would otherwise interfere with the inferred weathering conditions at the time of deposition, revealed by calculating the index of chemical alteration (CIA).

Fifty-eight thin sections were prepared from the consolidated and the semi-consolidated sandstone samples after impregnation with epoxy resin for use in modal analysis and microscopic measurement of grain size. All the thin sections were stained with alizarin red-S and K-ferricyanide pigments to distinguish between calcite and dolomite. Modal analyses of the 58 sandstone samples were carried out, using a LEICA DMLP research polarized-light microscope, and the results are listed in Supplementary Table 2. Scanning electron microscopy (SEM) was carried out for sandstone chips

and individual heavy mineral grains, employing the FEI-Inspect F50 model (field emission gun) after coating them with platinum, using an Emitec K550X coater. Elemental microanalysis was accomplished by an EDS (Bruker SDD detector) attached to the SEM. All these instruments are housed at the Faculty of Science, the University of Jordan.

The friable sandstone samples were sieved through the  $1\Phi$  interval, starting from  $-1\Phi$  to  $4\Phi$ , to determine the graphic mean grain size ( $M_1\Phi$ , Tab. 1), and for the separation of heavy minerals. The partly consolidated sandstone samples were disaggregated gently, using a glass rod, and further sieved. On the other hand, the well-consolidated sandstone samples were only thin-sectioned, and the grain size was determined by measuring the long axes of 500 grains. The data obtained were converted to sieve grain-size distribution by employing Friedman’s special chart (Müller, 1967).

The sand fraction of 63 to 250  $\mu\text{m}$  from all of the 58 sandstone samples was employed to obtain the heavy minerals, using the heavy liquid tetrabromoethane of specific gravity 2.96. The heavy minerals separated were then mounted on a glass slide, using epoxy resin and covered with a thin glass-cover for study under the polarized-light microscope; 500 grains were identified and counted in each grain mount. The results are summarized in Supplementary Table 3.

The sample fraction less than 0.063  $\mu\text{m}$  ( $<4\Phi$ ), concentrated in the shaker pan below the last sieve ( $4\Phi$ ), is considered to be the detrital matrix in all sandstone samples. Part of the matrix of 27 sandstone samples that contain more than 5% modal matrix (Supplementary Tab. 2), was used to prepare a random powder mount to be run in the XRD unit from 2 to 65° 2 $\theta$ , using a scanning rate of 2°/min., a range of  $4\times 10^3$ , and a chart speed of 2 cm/min. For example, an XRD chart of a random powder mount of sample H6 can be seen in Fig. 4A. The used XRD unit is Philips Xpert MPD, housed in the Geology Department, the University of Jordan. The other part of the matrix underwent gravitational settling following Stoke’s law to obtain the clay-sized fraction. From this clay-sized fraction, as well as from the 12 mudstone samples, four types of smear clay mounts were prepared: normal oriented, glycolated, heated to 350 °C, and heated to 550 °C, and they were run in the XRD unit. The XRD charts for all samples are available upon request from the first author. From the heights of the peaks, the relative abundance of the clay and other minerals was established (Biscaye, 1965; Moore and Reynolds, 1989).

The clay minerals, occurring as a cement filling the pore spaces, interstitial between the framework components, were identified in the thin sections according to their homogeneity, purity, and clarity, so as to be distinguished from the detrital matrix, consisting of inhomogeneous, impure, very fine-grained particles that are unidentifiable at the resolution of the polarized microscope.

Another portion of all the 58 sandstone and all the 12 mudstone samples were ground, using an agate ball mill after drying. To get representative sandstone and mudstone samples, two hundred grams of each bulk sample were ground to ensure that the entire components of the sandstone, which are the framework grains, matrix, and cements, were represented without bias in each powder sample. Three

Table 1

Summary of sample number, suite, location, age, depositional environment, mean grain size ( $M_{\phi}$ ), sandstone type, major elements, rare-earth elements, and trace elements.

Sample No.	GPS coordinates		Age	Dep. env.	$M_{\phi}$	Sst type	Major elements (oxides)	$\Sigma$ REEs	$\Sigma$ LREEs	$\Sigma$ HREEs	Trace elements
	E	N									
Sandstone suite 1 (n = 9)											
SR1	35.67067	30.4733	Camb.	Fl.	0.03	SA	Si, Al, K, Fe, Ti, Mg, Ca, Na, P	289.98	262.4	27.58	Zr, Th, Ba, Sr, Rb, V, Nb, Zn, Y, Cr, Ni, Co, U, Ga, Pb, Sc, Hf, Sn, W, Cu, Ta
SR5	35.67067	30.4733	Camb.	Fl.	2	SA	Si, Al, K, Ca, Ti	96.11	90.31	5.8	Ba, Sr, Zr, Rb, V, Cr, Y, Nb, Pb, Th
SD1	36.11633	31.3893	Camb.	Fl.	-0.1	SA	Si, Al, K, Ti, Ca, Fe	169.15	161.73	7.42	Ba, Zr, Sr, Cr, Rb, Th, V, Cu, Nb, Zn, Y, Ni
SD3	36.11633	31.3893	Camb.	Fl.	0.57	SA	Si, Al, K, Fe, Ti, Ca	69.87	66.37	3.5	Ba, Zr, Sr, Th, Rb, V, Cr, Cu, Pb, Zn, Nb
SD7	36.11633	31.3893	Camb.	Fl.	0.57	SA	Si, Al, K, Ca, Ti, Fe, Mg	125.51	117.24	8.27	Ba, Sr, Zr, Rb, V, Y, Th, Y, Cr, Zn, Nb, Ga
SD9	36.11633	31.3893	Camb.	Fl.	0.2	SA	Si, Al, K, Ca, Fe, Ti	103.51	99.63	3.88	Ba, Sr, Zr, Rb, V, Zn, Cu, Cr, Th, Y, Ga
AK2	35.58267	30.4477	Camb.	Sh.M.	2.13	SA	Si, Al, K, Ti	43.33	40.22	3.11	Zr, Ba, Sr, Rb, Cu, Cr, V, Zn
AK6	35.58267	30.4477	Camb.	Sh.M.	2.7	SA	Si, Al, K, Ca, Ti, Fe	49.82	46	3.82	Ba, Zr, Sr, Rb, Cu, Cr, V, Zn, Pb, Y, Hf, Ga
AK11	35.58267	30.4477	Camb.	Sh.M.	2.63	SA	Si, Al, K, Ti, Fe, Ca, Mg, Na	97.47	88.02	9.45	Zr, Ba, Sr, Rb, Cu, Hf, V, Y, Pb, Th, Nb, Cr, Zn, Ga
Sandstone suite 2 (n = 14)											
SR10	35.63067	30.4363	Camb.	Fl.	1.3	SA	Si, Al, Fe, Ca	27.72	24.73	2.99	Zr, Sr, Cr, Ba, Zn, Ni
AK15	35.58267	30.4477	Camb.	Fl.	1.3		Si, Al, Ca, Ti	122.9	109.96	12.94	
UI1	36.326	29.9087	Camb.	Fl.	1.5	QA	Si, Al, Ca, Fe	38.7	35.27	3.43	Zr, Sr, Ba, Cr, Pb, Zn, V
UI5	36.374	29.9087	Camb.	Fl.	1.67	QA	Si, Al, Ca, Fe, Ti	67.39	60.45	6.94	Zr, Sr, Ba, Cr, Y, Pb, V, Zn
UI9B	35.95733	30.4410	Camb.	Fl.	1.87	QA	Si, Al, Ca, Ti	68.86	60.71	8.15	Zr, Sr, Ba, V, Y, Cr, Hf, Th
UI17	36.127	29.9853	Camb.	Fl.	1.23	QA	Si, Al, Ca, Fe, Mg	39.53	36.55	2.98	Sr, Zr, Cr, Ba, V, Zn, Pb, Ni
DS1	36.38167	30.2330	Ord.	Fl.	1.6	QA	Si, Al	56.11	50.72	5.39	Zr, Sr, Ba, V, Cr, Y, Pb
DS2	36.38067	30.2440	Ord.	Fl.	1.67	QA	Si, Al, Ca, Ti	54.27	48.6	5.67	Zr, Sr, Ba, Cr, Y, V, Ni, Th, Hf
DS6	36.31967	29.8530	Ord.	Fl.	1.9	QA	Si, Al, Ti	58.02	52.5	5.52	Zr, Sr, Ba, V, Cr, Pb, Y, Ni
DS15	35.948	30.0010	Ord.	Fl.	1.9	QA	Si, Ca, Al	329.58	255.3	74.28	Sr, Zr, Ba, Y, Zn, Rb, Ga, Cr, Nb, Hf, Ni, Pb, V, Sn, Cu
US1	36.15333	29.7273	Ord.	Fl.	0.7	QA	Si, Ca, Al, Ti	41.97	38.24	3.73	Zr, Sr, Ba, Cr, Pb, Zn, V, Y, Ni
US4	36.08133	29.6853	Ord.	Fl.	1.3	QA	Si, Al, K, Fe, Ti	36.35	33.7	2.65	Zr, Sr, Ba, Cr, Ni
US10	36.39633	30.0880	Ord.	Fl.	2	QA	Si, Al	34.16	32.52	1.64	Zr, Sr, Cr, Ba, V, Pb, Ni
US12	36.39633	30.0880	Ord.	Fl.	2.5	QA	Si, Al, Ca, Ti	49.53	47.36	2.17	Zr, Pb, Sr, Cr, Ba, Ni, V
Sandstone suite 3 (n = 24)											
H6	36.48733	29.6777	Ord.	Sh.M.	3.5	SA	Si, Al, Fe, K, Mg, Ti, Na, Ca, P	224.31	204.68	19.63	Ba, Zr, Rb, Sr, Zn, V, Cr, Ni, Y, Cu, Ga, Co, Nb, Sc, Pb, Th, Hf, Cs
H9	36.48733	29.6777	Ord.	Sh.M.	3	SA	Si, Al, K, Fe, Ca, Mg, Ti, Na	114.87	107.94	6.92	Ba, Zr, Sr, Rb, Zn, V, Cr, Pb, Ni, Y, Ga, Cu

Sample No.	GPS coordinates		Age	Dep. env.	M $\phi$	Sst type	Major elements (oxides)	$\Sigma$ REEs	$\Sigma$ LREEs	$\Sigma$ HREEs	Trace elements
	E	N									
D3	36.48733	29.6777	Ord.	Sh.M.	3	SA	Si, Al, K, Ti, Fe, Ca, Mg	141.17	133.04	8.13	Zr, Ba, Sr, Rb, Cr, V, Zn, Hf, Th, Y, Pb, Ni, Nb
D5A	36.483	29.5997	Ord.	Sh.M.	3.43	SA	Si, Al, K, Ti, Fe, Mg	392.2	366.38	25.82	Zr, Ba, Sr, Cr, Rb, Hf, Y, Th, V, Zn, Nb, Pb, Ni, U
D10	36.439	29.6287	Ord.	Sh.M.	3	SA	Si, Al, K, Ti, Fe, Mg, Na	203.95	191.04	12.91	Zr, Ba, Sr, Cr, Rb, Hf, V, Th, Y, Zn, Nb, Ni, Pb, Ga
D19	36.05033	29.6763	Ord.	Sh.M.	2	SA	Si, Al, K, Ti, Na, Ca, Mg, Fe	72.85	69.37	3.48	Ba, Zr, Sr, Rb, Cr, V, Ni, Pb, Zn, Cu
D23	36.09933	29.7643	Ord.	Sh.M.	2.9	SA	Si, Al, K, Na, Fe, Ca, Mg, Ti	81.36	73.15	8.21	Ba, Zr, Sr, Rb, Cr, V, Y, Pb, Ni, Ga, Hf, Th, Nb
DZ1	36.408	29.8070	Ord.	Sh.M.	3.13	SA	Si, Ca, Al, K, Fe, Ti, Mg, Ca	191.45	180.6	10.85	Zr, Ba, Sr, Cr, Rb, V, Hf, Th, Zn, Y, Cu, Ga
DZ10	36.35233	29.9087	Ord.	Sh.M.	3.03	SA	Si, Al, K, Fe, Mg, Ti, Mn	97.84	90.2	7.64	Ba, Zr, Sr, Rb, Cr, Pb, V, Zn, Y, Ni, Hf
DZ12	36.35233	29.9087	Ord.	Sh.M.	3.1	SA	Si, Al, K, Fe, Ti, Ca, Mg, Na	174.59	158.04	16.55	Ba, Zr, Sr, Rb, Cr, V, Zn, Pb, Th, Ni, Hf, Ga, Nb, Cu
DZ13	36.35233	29.9087	Ord.	Sh.M.	3.1	SA	Si, Al, K, Ti, Fe, Ca, Mg	207.74	195.12	12.62	Zr, Ba, Sr, Rb, Cr, V, Hf, Th, Y, Zn, Nb, Ni, Pb, Ga, Cu
TB1	36.66267	30.4597	Ord.	Sh.M.	2.77	SA	Si, Al, K, Ca, Fe, Na, Mg	87.42	84.08	3.34	Ba, Sr, Rb, Zr, Cr, Pb, Zn, V, Cu, Ni
TB4	36.66267	30.4597	Ord.	Sh.M.	3.4	SA	Si, Al, Fe, K, Na, Mg, Ca, Ti	97.12	85.26	11.86	Ba, Zr, Sr, Rb, V, Cr, Zn, Ni, Cu, Y, Ga, Pb, Th, Hf, Sc, Co
TB9	36.72933	30.5090	Ord.	Sh.M.	2.2	SA	Si, Al, K, Ca, Fe, P, Ti	114.05	90.73	23.32	Ba, Zr, Sr, Rb, Y, Cr, Ni, Pb, Cu
AM1	36.65933	29.6817	Ord.	Sh.M.	2.8	SA	Si, Al, K, Fe, Na, Mg, Ti, Ca	129.69	117.33	12.36	Ba, Zr, Sr, Rb, V, Cr, Zn, Ni, Y, Pb, Ga, Cu, Hf, Nb, Th, Sc, Co
AM5	36.169	30.1440	Ord.	Sh.M.	2.5	SA	Si, Al, K, Fe, Ti, Mg, Na	93.62	85.49	8.13	Zr, Ba, Sr, Rb, Ni, V, Cr, Zn, Y, Hf, Pb, Th, Ga
AM8	36.169	30.1440	Ord.	Sh.M.	2.87	SA	Si, Al, K, Fe, Ti, Ca	72.47	67.32	5.15	Ba, Zr, Sr, Rb, Cr, V, Zn, Ni, Pb, Y, Hf, Ga
BT2	36.001	30.1290	L.Sil.	Sh.M.	3.17	SA	Si, Al, K, Fe, Ti, Mg, Na, Ca	80.81	75	5.81	Ba, Zr, Sr, Rb, V, Zn, Cr, Pb, Ni, Ga, Y, Cu
RS3	36.55833	30.4860	L.Sil.	Sh.M.	3.5	SA	Si, Al, Ca, K, Mg, Fe, Na, Ti, Mn	177.53	149.73	27.8	Ba, Zr, Sr, Rb, Cr, Y, V, Zn, Hf, Th, Nb, Ni, Pb, Ga, Sc, Cu
RS5	36.55833	30.4860	L.Sil.	Sh.M.	3.7	SA	Si, Al, K, Fe, Na, Mg, Ti, Ca	99.57	87.28	12.29	Ba, Zr, Zn, Cr, V, Y, Pb, Ga, Ni, Nb, Hf, Th, Cu, Sc
RS11	36.79917	29.7430	L.Sil.	Sh.M.	3.9	SA	Si, Al, Ca, K, Fe, Ti, Na, Mg	217.07	190.5	26.57	Ba, Zr, Sr, Rb, Cr, Y, V, Hf, Zn, Th, Pb, Nb, Ni, Ga
KH1	36.131	29.8137	L.Sil.	Sh.M.	4.4	SA	Si, Al, K, Fe, Ti, Na, Mg	227.18	193.11	34.07	Zr, Ba, Sr, Rb, Cr, Y, Zn, V, Nb, Pb, Th, Ni, Ga, Cu, Sc, Co
KH2	36.131	29.8137	L.Sil.	Sh.M.	3.5	SA	Si, Al, K, Ti, Na, Fe, Ca, P	468	403.23	64.77	Ba, Zr, Sr, Y, Rb, Cr, Hf, Th, V, Zn, Nb, Pb, Ni, Cu, U, Ga, Sc
KH4	36.131	29.8137	L.Sil.	Sh.M.	3.8	SA	Si, Al, K, Ca, Fe, Ti, Na, Mg	185.39	158.36	27.03	Zr, Ba, Sr, Rb, Cr, Y, Zn, V, Nb, Pb, Hf, Th, Ni, Ga, Cu, Sc, Co
Sandstone suite 4 (n = 11)											
TB13	36.77033	30.5090	Ord.	Sh.M.	2.5	QA	Si, Al, K, Ca, Fe	86.48	80.37	6.11	Ba, Zr, Sr, Rb, Cr, Zn, Y, V, Pb,
K1	35.515	31.2881	L.Cre.	Fl.	1.77	QA	Si, Al, Fe	22.08	20.51	1.57	Zr, Ba, Sr, Cr, Zn, V, Ni
K3	35.515	31.2881	L.Cre.	Fl.	2.53	QA	Si, Fe, Al, Ti	31.26	28.05	3.21	Zr, Ba, Sr, Cr, Zn, V, Hf
K6	35.515	31.2881	L.Cre.	Fl.	1.9	QA	Si, Al, K, Fe	30.95	28.49	2.46	Zr, Ba, Sr, Cr, Zn, V
HM8	35.6103	31.6094	L.Cre.	Fl.	1.7	QA	Si, Al, Fe, Ti	50.76	45.87	4.89	Zr, Ba, Sr, Cr, V, Zn, Y, Ni, Pb, Hf

Sample No.	GPS coordinates		Age	Dep. env.	M <sub>f</sub> φ	Sst type	Major elements (oxides)	ΣREEs	ΣLREEs	ΣHREEs	Trace elements
	E	N									
R1	35.71667	32.1500	L.Cre.	Fl.	0.9	QA	Si, Al, Ti, Fe, K, Mg	91.42	80.66	10.76	Zr, Sr, Zn, V, Cr, Ni, Ba, Co, Nb, Y, Hf, Rb, Ga, Sc, Th, Pb
R4	35.71667	32.1500	L.Cre.	Fl.	1.17	QA	Si, Al	26.18	23.7	2.48	Zr, Sr, Ba, Cr, Zn, V
R9	35.71667	32.1500	L.Cre.	Fl.	1.5	QA	Si	23.09	20.96	2.13	Zr, Sr, Cr, Ba, Zn, V
J25	35.8882	32.2700	L.Cre.	Fl.	1.8	QA	Si, Al	15.46	14.26	1.2	Zr, Ba, Cr, Sr, Zn
BF1	35.8882	32.2700	L.Cre.	Sh.M.	3.1	QA	Si, Al, Ti, K, Fe	180.92	158.51	22.41	Zr, Ba, Sr, Cr, V, Y, Zn, Nb, Rb, Hf, Pb, Th, Ga, Cu, Sc, Ni
B10S	36.09667	30.1857	L.Cre.	Sh.M.	3.7	QA	Si, Al, Fe, Ti, K	113.38	100.32	13.06	Zr, Ba, Sr, V, Cr, Hf, Y, Zn, Th, Nb, Pb, Rb, Sc, Ga, Ni
Mudstone suite (n = 12)											
H1	36.43	30.3383	Ord.	Sh.M.	Mud	Muds	Si, Al, K, Fe, Ti, Na, Mg, P	327.06	301.94	25.12	Ba, V, Cr, Sr, Zn, Ni, Zr, Rb, Pb, Cu, Ga, Y, Sc, Th, Nb, U
BT6	37.09867	30.1857	L.Sil.	Sh.M.	Mud	Muds	Si, Al, Fe, K, Ti, Mg, P, Na	386.4	367.73	18.67	Ba, Zr, Sr, Rb, Cr, V, Zn, Pb, Ga, Ni, Cu, Y, Sc, Th, Cs, Co
LO28	36.15333	29.7273	Ord.	Sh.M.	Mud	Muds	Si, Al, Ti, Ca, Fe, Na, P	n.d.	n.d.	n.d.	Sr, Zr, Ba, V, Zn, Cu, Y, Sc, Ni, Co
MO12	36.43	30.3383	Ord.	Sh.M.	Mud	Muds	Si, Al, Fe, K, Mg, Na, P	n.d.	n.d.	n.d.	Sr, Ba, V, Zn, Zr, Cu, Ni, Sc, Y, Co
LS8	36.48733	29.6777	L.Sil.	Sh.M.	Mud	Muds	Si, Al, Fe, K, Mg, Ti, Na, Ca	n.d.	n.d.	n.d.	Ba, Zr, V, Zn, Sr, Cu, Ni, Co, Y, Sc
PTA1	35.565	31.6183	L.Tri.	Fl.	Mud	Muds	Si, Al, Fe, Ti, Na	n.d.	n.d.	n.d.	Ba, Zr, V, Sr, Ni, Zn, Co, Cu, Y
TM7	35.8833	31.2833	Tri.	Sh.M.	Mud	Muds	Si, Al, Fe, K, Ti, Mg, Ca, Na	n.d.	n.d.	n.d.	Zr, V, Ba, Y, Ni, Zn, Sr, Co, Se, Cu
TM40	35.8833	31.2833	Tri.	Sh.M.	Mud	Muds	Si, Al, K, Fe, Ti, Mg, Na, Ca, P	n.d.	n.d.	n.d.	Zr, Ba, V, Sr, Y, Zn, Co, Ni, Se, Cu
TA13	35.7167	32.1500	Tri.	Sh.M.	Mud	Muds	Si, Al, Fe, Ti, K, Mg, Ca, Na	n.d.	n.d.	n.d.	Ba, Zr, V, Sr, Zn, Ni, Co, Y, Cu, Sc
JH17	35.5417	32.1156	Jura.	Sh.M.	Mud	Muds	Si, Al, Fe, Ti, Mg, K, Ca, Na, P, Mn	n.d.	n.d.	n.d.	Zr, Zn, Sr, V, Ba, Co, Y, Ni, Se, Cu
JA10B	35.7167	32.1500	Jura.	Sh.M.	Mud	Muds	Si, Al, K, Fe, Ti	n.d.	n.d.	n.d.	Zr, V, Sr, Ba, Zn, Ni, Y, Co, Cu, Sc
CrZ7	35.5417	32.1156	L.Cre.	Fl.	Mud	Muds	Si, Al, Fe, Ti, K, Mg, Ca, Na, P	n.d.	n.d.	n.d.	Sr, Zr, Ba, V, Co, Zn, Cu, Ni, Sc

Sample No. – sample number, Sst – sandstone, Camb. – Cambrian, Ord. – Ordovician, L.Sil. – Lower Silurian, L.Cre. – Lower Cretaceous, Tri. – Triassic, Jura. – Jurassic, Fl. – Fluvial, Sh.M. – Shallow marine, M<sub>f</sub>φ – mean grain size in phi units, SA – subarkosic arenite, QA – quartz arenite, TEs are arranged in decreasing abundance ending at 5 ppm, major element oxides are arranged in decreasing abundance ending at 0.1%. n.d. – not determined.

Table 2

Trace element abundance (in ppm) for all the individual samples in suites, the means of TEs in grain sizes, suites, and standards and reference rocks.

Element	Ba	Co	Cr	Cs	Cu	Ga	Hf	Nb	Ni	Pb	Rb	Sc	Sn	Sr	Ta	Th	U	V	W	Y	Zn	Zr
An. Pre.	0.5	0.5	10	0.05	5	0.1	0.2	0.1	5	5	0.2	0.1	1	0.1	0.1	0.05	0.05	5	1	0.5	5	2
Sandstone suite 1 (n = 9)																						
SR1	450	34.1	40	1.97	8	17.9	13.8	76	37	16	165	14.1	10	344	5.8	504	32	111	10	48.8	67	515
SR5	168	0.7	10	0.53	b.d.	4.5	3.1	5.2	b.d.	5	38.5	1.5	b.d.	133.5	0.4	4.93	1.48	12	1	8.4	b.d.	115
SD1	195.5	1.4	110	0.44	27	4.8	4.8	26	5	10	42.5	4.3	4	145	2.2	38.5	2.45	34	1	10.5	21	185
SD3	128.5	0.9	20	0.31	11	3.5	2.7	6.9	b.d.	9	32.9	2.7	b.d.	60.1	0.6	39.4	0.9	21	1	4.8	7	88
SD7	304	1.1	10	0.56	6	5.3	2.3	5.7	b.d.	9	59.1	2.5	b.d.	109	0.5	10.75	1.57	20	b.d.	12.6	8	78
SD9	329	1.4	10	0.59	12	5.6	2.8	4.6	b.d.	8	50.2	2.7	b.d.	118.5	0.4	6.42	0.81	21	1	5.9	18	92
AK2	115	b.d.	10	0.26	18	3.1	3.9	2.6	b.d.	b.d.	23	1.1	b.d.	65.6	0.2	4.81	1.03	9	b.d.	4.6	5	153
AK6	234	0.7	10	0.54	22	5.2	5.9	4.7	b.d.	7	43.7	1.3	b.d.	69.6	0.4	4.63	1.06	10	b.d.	6.2	8	230
AK11	448	1.3	10	0.77	33	6.6	21.2	11.9	b.d.	13	62.9	2.2	b.d.	168	0.9	12.6	3.3	17	1	14.6	9	766
Mean	263.6	5.2	25.6	0.7	17.1	6.3	6.7	16	21	9.6	57.5	3.6	7	134.8	1.3	69.6	5	28.3	2.5	12.9	17.9	246.9
Sandstone suite 2 (n = 14)																						
SR10	9.7	0.5	20	0.05	b.d.	2.8	2.2	2.4	5	b.d.	0.8	b.d.	b.d.	28.9	0.2	2.43	0.66	b.d.	2	4.3	6	80
AK15	>10000	b.d.	10	b.d.	21	4.1	4.5	4.1	b.d.	11	0.4	0.6	b.d.	600	0.4	5.98	2.72	5	b.d.	19	8	175
UI1	10.7	0.5	10	0.16	b.d.	2.9	2.4	3.5	b.d.	6	1.8	0.6	b.d.	55.6	0.3	2.91	1.28	5	b.d.	4.6	5	75
UI5	32.5	b.d.	20	b.d.	b.d.	2.6	3.6	4.2	5	10	0.2	1.1	b.d.	419	0.4	4.54	1.38	9	b.d.	11.3	6	132
UI9B	27	b.d.	10	0.03	b.d.	3.5	7	4.5	b.d.	7	0.9	1.7	b.d.	61.2	0.6	6.15	1.24	13	b.d.	12	b.d.	243
UI17	17.3	0.5	20	0.03	b.d.	2.1	2.4	3	5	7	0.2	2	b.d.	118.5	0.2	2.86	1.08	16	b.d.	3.5	9	81
DS1	12.6	b.d.	10	0.02	b.d.	2.1	1.9	1.7	b.d.	6	0.2	1.7	b.d.	55.2	0.1	3.73	0.96	13	b.d.	7.6	b.d.	61
DS2	13.5	b.d.	10	0.23	b.d.	2.5	3.7	3.2	5	8	2.4	1	b.d.	53.8	0.3	4.56	1.02	8	b.d.	8.9	b.d.	136
DS6	17.7	b.d.	10	0.05	b.d.	3.3	3.1	2.6	6	8	1	2.3	b.d.	132.5	0.2	2.86	1.54	18	b.d.	7.7	5	120
DS15	313	2.5	20	1.46	5	36	11.1	13.9	9	9	56.1	0.8	6	1210	0.8	1.29	0.76	6	b.d.	119.5	101	564
US1	17.6	0.7	20	0.09	b.d.	1.1	2.4	1.3	5	18	1.8	0.9	b.d.	39.9	0.1	2.97	0.82	7	b.d.	5.3	8	87
US4	13.7	b.d.	10	0.03	b.d.	0.8	4.1	1.8	6	21	0.2	b.d.	b.d.	37.1	0.2	2.79	0.86	b.d.	b.d.	3.4	b.d.	168
US10	14.5	b.d.	20	0.02	b.d.	2.2	1.5	1	7	8	0.4	1	b.d.	27	0.1	1.19	0.38	8	b.d.	1.9	b.d.	57
US12	17.8	b.d.	20	0.03	b.d.	1.3	4.1	1.9	9	34	0.3	0.6	b.d.	32.6	0.2	2.3	0.56	5	b.d.	2.5	b.d.	162
Mean	39.8	0.9	15	0.2	13	4.8	3.9	3.5	6.2	12.5	4.8	1.2	6	205.1	0.3	3.3	1.1	9.4	2	15.1	18.5	152.9

Element	Ba	Co	Cr	Cs	Cu	Ga	Hf	Nb	Ni	Pb	Rb	Sc	Sn	Sr	Ta	Th	U	V	W	Y	Zn	Zr
Sandstone suite 3 (n = 24)																						
H6	882	19	110	5.06	26	27.9	6	16.6	50	14	165	15.1	4	145	1.2	12.8	3.35	119	1	30.8	134	217
H9	1135	1.6	20	0.77	6	8	4.6	4.9	11	16	83.9	3.1	b.d.	155	0.4	4.82	0.99	24	b.d.	8.7	31	180
D3	559	2.1	30	0.43	b.d.	4.8	14.3	6.6	9	9	41.6	3.2	b.d.	93.2	0.5	11.15	2.19	25	1	11	24	577
D5A	493	2.1	50	0.34	b.d.	4.1	37.8	17.2	8	9	38.1	3.4	1	134.5	1.5	36.2	6.79	27	1	37	19	1530
D10	616	2.6	50	0.41	b.d.	5.9	35.4	13.5	11	9	46	3.8	1	117	1.1	23.3	4.19	30	1	18.1	17	1490
D19	376	1.6	20	0.7	6	4.1	2.5	3.2	9	8	40.4	2	b.d.	77.8	0.2	2.87	0.65	16	b.d.	4.7	7	97
D23	629	2	20	0.91	6	8.3	7.2	5.4	10	10	73.4	2.2	1	108	0.4	5.8	1.27	17	1	13.2	12	281
DMZ1	466	3.3	40	0.41	6	5.7	25.1	8.6	11	8	36.9	4.2	1	91.6	0.7	17.9	3.25	33	1	14.1	16	1030
DM10	423	1.4	20	0.27	b.d.	2.7	6	2.9	7	14	27.9	1.7	b.d.	120	0.2	3.39	1.34	13	b.d.	10.5	12	241
DM12	999	2.8	40	1.12	6	8.6	10.8	7.5	11	15	102	3.6	1	133.5	0.6	11.85	2.35	28	1	24.3	16	433
DM13	551	2.9	30	0.61	5	5.2	26.7	10	9	9	45.6	3.6	1	101	0.8	19.85	4.21	28	1	17.2	13	1070
TB1	639	1.6	20	0.72	7	4.6	1.6	1.5	6	13	75.7	0.9	b.d.	156.5	0.1	1.92	0.39	7	b.d.	3.7	8	64
TB4	605	6.7	50	2.11	12	16.2	7.3	9.8	21	14	96.9	6.9	2	203	0.7	7.3	2.21	54	1	19.7	41	289
TB9	436	2.3	20	0.55	5	3.4	4.3	2.7	12	9	48.7	0.9	b.d.	161.5	0.2	2.54	1.34	7	b.d.	47.3	b.d.	169
AM1	588	6.4	50	2.2	12	14	8.8	8.8	23	14	96	7.1	1	171	0.7	8.14	1.98	56	1	18.8	45	356
AM5	366	3.3	20	0.76	b.d.	5	9.5	4.4	22	8	43.2	2.7	b.d.	133.5	0.4	5.27	1.35	21	b.d.	11.8	19	398
AM8	565	3.1	30	0.79	b.d.	5.8	6.2	3.9	13	13	63.9	3.1	b.d.	142.5	0.3	4.07	1.47	24	b.d.	7.3	17	247
BT2	856	2.9	20	1.34	6	9.2	4.6	4.7	11	14	99.9	3.7	1	168	0.3	4.43	0.77	29	1	8.7	23	181
RS3	847	2	50	0.74	5	8.3	19.3	11.1	11	11	76.5	5.3	1	303	0.8	14.7	3.16	42	1	48.7	26	743
RS5	1085	3.2	50	1.5	6	12.9	7.9	9.6	14	16	109.5	5.7	1	167.5	0.6	7.85	1.56	45	1	21.7	87	299
RS11	1015	1.9	50	0.83	b.d.	8.8	20.8	11.9	11	13	89.2	4.6	1	147.5	0.8	15.25	3.3	36	1	45.7	16	836
KH1	755	5.4	70	1.71	9	11.6	23.6	26.1	18	25	96.1	7.1	2	112.5	1.7	19.1	4.37	56	2	60.9	59	918
KH2	>10000	1.6	70	1.05	9	5.7	56.1	25.7	11	16	77	5.2	2	327	1.9	43.5	8.21	41	2	108	31	2100
KH4	794	6.5	60	1.27	42	8.7	21.3	18	22	14	95	4.7	1	170	1.2	16.35	3.53	37	1	46.5	25	849
Mean	681.7	3.7	41.3	1.1	10.2	8.3	15.3	9.8	14.2	12.5	73.7	4.3	1.4	151.7	0.7	12.5	2.7	34	1.1	26.6	30.3	608.1
Sandstone suite 4 (n = 11)																						
TB13	221	1.3	10	0.27	b.d.	2	2.2	1.7	b.d.	7	24.2	1	b.d.	132	0.1	2.12	0.29	8	b.d.	8.7	10	82
K1	16.8	0.7	10	0.03	b.d.	0.8	3.4	0.6	5	b.d.	0.4	1.3	b.d.	10.2	0	1.68	0.47	10	b.d.	2.1	10	138
K3	33.6	b.d.	20	0.02	b.d.	1.3	5.1	2.9	b.d.	5	0.4	1.3	b.d.	13.7	0.2	2.72	0.66	10	b.d.	4.7	11	184
K6	31.8	1	20	0.25	b.d.	2.5	2.4	2.1	b.d.	b.d.	1.6	1.4	b.d.	14.5	0.2	1.86	0.42	11	b.d.	3.2	13	90
HM8	17.8	0.9	20	0.1	b.d.	2.4	5.7	4.3	6	6	1.1	2.3	b.d.	17.3	0.3	3.28	0.9	18	b.d.	6.8	14	219
R1	29.3	24.5	50	0.86	b.d.	7.4	13	20	33	5	7.7	7	1	89	1.3	5.39	2.25	55	1	18.3	80	569
R4	10	0.5	10	0.03	b.d.	0.9	1.8	2.1	b.d.	b.d.	0.4	0.8	b.d.	19.3	0.2	1.33	0.53	6	b.d.	3.7	7	68

Element	Ba	Co	Cr	Cs	Cu	Ga	Hf	Nb	Ni	Pb	Rb	Sc	Sn	Sr	Ta	Th	U	V	W	Y	Zn	Zr
R9	9.7	0.7	10	0.01	b.d.	0.8	2.3	2.9	b.d.	b.d.	0.2	0.6	b.d.	14.8	0.4	1.07	0.49	5	b.d.	3	7	84
J25	10.5	b.d.	10	0.01	b.d.	0.9	1.6	0.6	b.d.	b.d.	0.2	b.d.	b.d.	8.9	0.1	0.89	0.34	b.d.	b.d.	1.6	7	57
BF1	166.5	0.8	60	1.71	8	9.6	21.1	21.9	5	17	21.1	6.4	2	97.4	1.6	14.65	3.98	50	1	35.8	25	796
BF10S	98.9	0.7	50	0.98	b.d.	5.9	20.4	13.1	5	10	7	6.5	1	59.4	1	11	2.36	51	1	19.5	15	751
Mean	58.7	3.5	24.5	0.4	8	3.1	7.2	6.6	10.8	8.3	5.8	2.9	1.3	43.3	0.5	4.2	1.2	22.4	1	9.8	18.1	276.2
Mudstone suite (n = 12)																						
H1	190	2.7	140	3.44	38	36.3	3.1	17.6	112	80	98	20.8	4	138	1.4	18.75	6.94	164	2	29.8	119	101
BT6	326	5.5	160	8.94	33	38.1	3.6	19.2	37	44	93.4	19.6	4	498	1.4	15.05	3.43	154	2	20.9	78	125
LO28	97	14	n.d.	n.d.	39	n.d.	n.d.	n.d.	15	n.d.	n.d.	30.6	n.d.	769	n.d.	n.d.	n.d.	241	n.d.	33	58	313
MO12	223	14	n.d.	n.d.	39	n.d.	n.d.	n.d.	29	n.d.	n.d.	18.4	n.d.	501	n.d.	n.d.	n.d.	145	n.d.	17	130	58
LS8	637	33	n.d.	n.d.	56	n.d.	n.d.	n.d.	48	n.d.	n.d.	16.1	n.d.	69	n.d.	n.d.	n.d.	127	n.d.	23	97	153
PTA1	698	17	n.d.	n.d.	12	n.d.	n.d.	n.d.	30	n.d.	n.d.	28.1	n.d.	96	n.d.	n.d.	n.d.	221	n.d.	7	23	229
TM7	77	30	n.d.	n.d.	3	n.d.	n.d.	n.d.	74	n.d.	n.d.	25.2	n.d.	60	n.d.	n.d.	n.d.	198	n.d.	78	74	604
TMK40	332	30	n.d.	n.d.	11	n.d.	n.d.	n.d.	28	n.d.	n.d.	14	n.d.	108	n.d.	n.d.	n.d.	110	n.d.	63	60	393
TAR13	1136	29	n.d.	n.d.	18	n.d.	n.d.	n.d.	33	n.d.	n.d.	14.7	n.d.	80	n.d.	n.d.	n.d.	116	n.d.	25	49	400
JH17	108	97	n.d.	n.d.	23	n.d.	n.d.	n.d.	46	n.d.	n.d.	36	n.d.	342	n.d.	n.d.	n.d.	283	n.d.	46	357	546
JAI0B	109	35	n.d.	n.d.	33	n.d.	n.d.	n.d.	40	n.d.	n.d.	22.1	n.d.	150	n.d.	n.d.	n.d.	174	n.d.	38	64	450
CrZ7	227	79	n.d.	n.d.	53	n.d.	n.d.	n.d.	36	n.d.	n.d.	18.3	n.d.	275	n.d.	n.d.	n.d.	144	n.d.	22	61	262
Mean	346.7	32.2	150	6.19	30	37.2	3.3	18.4	44	62	95.7	22	4	257.2	1.4	16.9	5.19	173	2	33.6	98	303
Averages																						
CS	207.7	9.2	37	0.69	13	6.5	6	20.1	20	11	51.3	4.9	5	129.4	1.6	86.78	5.83	38	3	15.2	30	231
US1	17.6	0.7	20	0.09		1.1	2.4	1.3	5	18	1.8	0.9	b.d.	39.9	0.1	2.97	0.82	7	b.d.	5.3	8	87
MS	59.1	0.9	14	0.2	11	4.1	3.5	3.4	6	9	7.4	1.3	6	154.8	0.3	2.96	0.96	11	2	11.9	15	138
FS	440.2	2.4	23	0.63	14	5.3	9	5.2	13	12	48.5	2.3	1	114.7	0.4	6.41	1.47	18	1	12.1	17	356
VFS	669.1	4	51	1.32	12	9.4	19.7	13.4	14	14	74	5.5	1	155.1	1	16.01	3.42	43	1	34.3	35	768
Av. S	343.1	3.6	29	0.68	12	6.2	9.7	8.6	12	12	41.7	3.2	2	141.4	0.7	17.57	2.36	26	1	18.5	24	379
Av. M	346.7	32.2	150	6.19	30	37.2	3.4	18.4	44	62	95.7	22	4	257.2	1.4	16.9	5.19	173	2	33.6	98	303
SAS1M	263.6	5.2	26	0.66	17	6.3	6.7	16	21	10	57.5	3.6	4	134.8	1.3	69.56	4.96	28	3	12.9	18	247
QAS2M	39.8	0.9	15	0.17	13	4.8	3.9	3.5	6	13	4.8	1.2	6	205.1	0.3	3.33	1.09	9	2	15.1	19	153
SAS3M	681.7	3.7	41	1.11	10	8.3	15.3	9.8	14	13	73.7	4.3	1	151.7	0.7	12.51	2.68	34	1	26.6	30	608
QAS4M	58.7	3.5	25	0.39	8	3.1	7.2	6.6	11	8	5.9	2.9	1	43.3	0.5	4.18	1.15	22	1	9.8	18	276
SAM	564.1	4.1	37	0.99	12	7.8	13	11.5	15	12	69.2	4.1	2	147.1	0.9	28.07	3.3	32	1	22.9	27	510
QAM	48.5	2.6	19	0.27	11	4.1	5.3	4.9	8	11	5.2	2	3	133.9	0.4	3.7	1.12	15	1	12.8	18	207

Element	Ba	Co	Cr	Cs	Cu	Ga	Hf	Nb	Ni	Pb	Rb	Sc	Sn	Sr	Ta	Th	U	V	W	Y	Zn	Zr
Standards and reference rocks																						
UCC	550	17	83	4.6	25	17	5.8	12	44	17	112	13.6	6	350	1	10.7	2.8	107	2	22	71	190
PAAS	650	20	100	6	50	n.r.	5	18	60	20	160	17.8	n.r.	200	1.3	14.6	3.1	140	n.r.	27	n.r.	240
NASC	636	25.7	125	5.16	n.r.	n.r.	6.3	n.r.	58	n.r.	125	n.r.	n.r.	n.r.	1.1	12.3	2.66	n.r.	2.1	n.r.	310	200
Phan Sh	551	20	104	n.r.	n.r.	n.r.	4.6	15.4	54	22	163	14.9	n.r.	136	1.4	13.5	2.9	117	n.r.	33	n.r.	210
Rah St	796	n.r.	6	1.1	5	19	4	6	8	75	86	2.8	2	525	n.r.	5	2	22	n.r.	10	n.r.	200
Fein St	227	n.r.	n.r.	2.12	12	18	6	25	5	23	142	2.2	2	56	n.r.	21	4	17	n.r.	32	n.r.	201
Av. AC.	353.4	n.r.	6	1.89	10	18.2	5.6	20.8	6	35	129.6	2.3	2	160.2	n.r.	17.44	3.56	18	n.r.	27.1	39	211
Duheil	288	n.r.	352	1	70	19	1	8	95	10	35	38	3	430	n.r.	1	1	299	n.r.	23	32	99
ArabM	808	n.r.	82	2.74	77	20	5	16	49	14	74	10.2	1	708	n.r.	5	1	80	n.r.	22	41	243
Monzg	1520	n.r.	32	n.r.	n.r.	21	n.r.	5	19	n.r.	80	17.9	n.r.	1178	n.r.	n.r.	n.r.	141	n.r.	18	104	98

Means are calculated only from the individual samples having values above the detection limit; thus, the means of Sn and W are insignificant. An. Pre. – analytical precision, M – mean, St – suite, Av. – average, S. – sand, MS – mudstone, SA – subarkosic arenite, QA – quartz arenite, Phan Sh – Phanerozoic Shale, Rah St – Rahma Suite, Fein St – Feinan Suite, Av. AC. – average Aqaba Complex, Duheil – Duheila Suite, ArabM – Araba Mafic Suite, Monzg – Monzogabbro Suite. For sample symbols, see caption of Figure 1. The data for standards come from Taylor and McLennan (1985), and McLennan (2001) for the UCC, Nance and Taylor (1976) for the Post-Archaean Australian shales (PAAS) and the North American shale composite (NASC), Condie (1993) for the Phanerozoic shale. For reference rocks, Jarrar et al. (2003) for Rahma Suite and Hummat Feinan Suite of the Aqaba Complex, Araba mafic to intermediate Suite of the Aqaba Complex, and Ghanem and Jarrar (2013) for the Monzogabbro.

**Table 3**

Concentrations of REEs (in ppm) in individual samples of the various sand size grades, the mudstone, means of suites, standards, and reference rocks.

Element	La	Ce	Pr	Nd	Sm	Eu	Gd	Tb	Dy	Ho	Er	Tm	Yb	Lu	ΣREEs	ΣLREEs	ΣHREEs	Eu/Eu*
An. Prec	0.5	0.5	0.03	0.1	0.03	0.03	0.05	0.01	0.05	0.01	0.03	0.01	0.03	0.01				
Sandstone suite 1 (n = 9)																		
SR1	69.7	124	13.2	44.7	9.41	1.39	8.26	1.37	6.82	1.43	4.44	0.64	3.96	0.66	289.98	262.4	27.58	0.48
SR5	23.2	42.1	4.8	16.6	2.96	0.65	1.92	0.27	1.2	0.28	0.91	0.14	0.92	0.16	96.11	90.31	5.8	0.83
SD1	33.4	92.9	6.42	23.7	4.51	0.8	2.51	0.35	1.61	0.34	1.11	0.17	1.14	0.19	169.15	161.73	7.42	0.72
SD3	23.1	25.4	3.91	11.9	1.78	0.28	1.19	0.17	0.76	0.17	0.54	0.08	0.5	0.09	69.87	66.37	3.5	0.59
SD7	32.7	49.1	6.59	23.6	4.41	0.84	2.97	0.4	1.8	0.42	1.26	0.18	1.07	0.17	125.51	117.24	8.27	0.71
SD9	32	43.5	5.08	16.3	2.35	0.4	1.21	0.17	0.81	0.19	0.65	0.1	0.64	0.11	103.51	99.63	3.88	0.72
AK2	9.5	18.6	2.2	8.1	1.49	0.33	1.01	0.14	0.65	0.15	0.49	0.08	0.5	0.09	43.33	40.22	3.11	0.82

Element	La	Ce	Pr	Nd	Sm	Eu	Gd	Tb	Dy	Ho	Er	Tm	Yb	Lu	ΣREEs	ΣLREEs	ΣHREEs	Eu/Eu*
AK6	11	22	2.42	8.7	1.55	0.33	0.98	0.15	0.82	0.2	0.67	0.15	0.72	0.13	49.82	46	3.82	0.82
AK11	19.8	41.2	4.71	17.7	3.65	0.96	2.78	0.42	2.05	0.47	1.63	0.24	1.57	0.29	97.47	88.02	9.45	0.92
Mean	28.3	51	5.48	19	3.57	0.66	2.54	0.38	1.84	0.41	1.3	0.2	1.22	0.21	116.08	107.99	8.09	0.73
Sandstone suite 2 (n = 14)																		
SR10	5.7	11.4	1.32	5.2	0.9	0.21	0.74	0.12	0.75	0.16	0.48	0.09	0.57	0.08	27.72	24.73	2.99	0.78
AK15	24.9	50	6.07	22.8	5.05	1.14	4.92	0.69	2.98	0.6	1.78	0.25	1.49	0.23	122.9	109.96	12.94	0.7
UI1	8.4	16.7	1.85	6.9	1.16	0.26	0.93	0.14	0.9	0.17	0.52	0.09	0.58	0.1	38.7	35.27	3.43	0.76
UI5	14	28.1	3.2	12.1	2.49	0.56	2.03	0.33	1.73	0.38	1.16	0.16	0.99	0.16	67.39	60.45	6.94	0.76
UI9B	13.6	29.1	3.25	12.1	2.17	0.49	1.99	0.37	2.24	0.46	1.38	0.19	1.32	0.2	68.86	60.71	8.15	0.72
UI17	7.8	17.8	1.89	7.4	1.36	0.3	1.02	0.13	0.7	0.13	0.41	0.07	0.45	0.07	39.53	36.55	2.98	0.78
DS1	11	24.1	2.64	10.6	1.9	0.48	1.6	0.25	1.51	0.27	0.77	0.13	0.75	0.11	56.11	50.72	5.39	0.84
DS2	10.8	24	2.55	9.3	1.61	0.34	1.56	0.27	1.57	0.3	0.85	0.13	0.86	0.13	54.27	48.6	5.67	0.65
DS6	11.2	25	2.73	11	2.12	0.45	1.96	0.26	1.4	0.24	0.69	0.1	0.76	0.11	58.02	52.5	5.52	0.67
DS15	54.9	117	14.35	55.2	11.85	2	14	2.61	18.65	4.33	14.3	2.39	15.85	2.15	329.58	255.3	74.28	0.47
US1	8.3	18.9	1.99	7.4	1.37	0.28	1.14	0.16	0.94	0.17	0.54	0.08	0.61	0.09	41.97	38.24	3.73	0.68
US4	7.3	16.8	1.7	6.5	1.19	0.21	0.89	0.11	0.64	0.12	0.35	0.05	0.43	0.06	36.35	33.7	2.65	0.62
US10	7.8	16.4	1.69	5.6	0.86	0.17	0.57	0.07	0.39	0.07	0.21	0.03	0.26	0.04	34.16	32.52	1.64	0.74
US12	11	23.1	2.48	9	1.56	0.22	0.83	0.1	0.51	0.09	0.26	0.04	0.29	0.05	49.53	47.36	2.17	0.59
Mean	14.1	29.9	3.41	12.9	2.54	0.51	2.44	0.4	2.49	0.54	1.69	0.27	1.8	0.26	73.22	63.33	9.89	0.7
Sandstone suite 3 (n = 24)																		
H6	46.8	97.8	10.75	40.5	7.36	1.47	5.67	0.84	5.21	1.03	3.01	0.45	2.97	0.45	224.31	204.68	19.63	0.69
H9	23.7	52	5.74	21.7	3.95	0.86	2.62	0.33	1.68	0.3	0.85	0.13	0.88	0.13	114.87	107.95	6.92	0.81
D3	32.2	65.1	6.76	24.4	3.98	0.6	2.71	0.34	1.92	0.38	1.1	0.18	1.28	0.22	141.17	133.04	8.13	0.56
D5A	86	178.5	18.75	69.5	11.95	1.68	8.57	1.13	6.17	1.2	3.61	0.56	3.94	0.64	392.2	366.38	25.82	0.51
D10	45.6	92.8	9.94	35.9	6.08	0.72	4.28	0.54	3.01	0.56	1.74	0.28	2.13	0.37	203.95	191.04	12.91	0.43
D19	16.5	34.2	3.45	12.7	2.1	0.42	1.22	0.16	0.84	0.16	0.46	0.07	0.5	0.07	72.85	69.37	3.48	0.8
D23	16.5	34.8	3.85	14.6	2.74	0.66	2.34	0.35	2.14	0.43	1.25	0.19	1.31	0.2	81.36	73.15	8.21	0.79
DMZ1	43.3	88.1	9.32	33.6	5.53	0.75	3.8	0.48	2.52	0.47	1.42	0.21	1.67	0.28	191.45	180.6	10.85	0.5
DMZ10	21.4	43.7	4.46	16.8	3.11	0.73	2.64	0.36	1.99	0.37	1.02	0.14	0.97	0.15	97.84	90.2	7.64	0.78
DMZ12	36.1	75.8	8.19	30.9	5.85	1.2	5.05	0.78	4.52	0.84	2.34	0.34	2.34	0.34	174.59	158.04	16.55	0.67
DMZ13	46	95.4	10.15	36.6	6.15	0.82	4.29	0.54	2.97	0.58	1.69	0.26	1.95	0.34	207.74	195.12	12.62	0.49
TBI	17.7	40.7	4.63	17.4	2.96	0.69	1.42	0.14	0.7	0.14	0.38	0.06	0.43	0.07	87.42	84.08	3.34	1.03
TB4	20.1	40	4.53	16.7	3.24	0.69	2.95	0.48	3.09	0.65	1.93	0.31	2.13	0.32	97.12	85.26	11.86	0.68



Element	La	Ce	Pr	Nd	Sm	Eu	Gd	Tb	Dy	Ho	Er	Tm	Yb	Lu	ΣREEs	ΣLREEs	ΣHREEs	Eu/Eu*
TA13	n.d.	n.d.	n.d.	n.d.	n.d.	n.d.	n.d.	n.d.	n.d.	n.d.	n.d.	n.d.	n.d.	n.d.	n.d.	n.d.	n.d.	n.d.
JH17	n.d.	n.d.	n.d.	n.d.	n.d.	n.d.	n.d.	n.d.	n.d.	n.d.	n.d.	n.d.	n.d.	n.d.	n.d.	n.d.	n.d.	n.d.
JA10B	n.d.	n.d.	n.d.	n.d.	n.d.	n.d.	n.d.	n.d.	n.d.	n.d.	n.d.	n.d.	n.d.	n.d.	n.d.	n.d.	n.d.	n.d.
CrZ7	n.d.	n.d.	n.d.	n.d.	n.d.	n.d.	n.d.	n.d.	n.d.	n.d.	n.d.	n.d.	n.d.	n.d.	n.d.	n.d.	n.d.	n.d.
Mean	72.5	157	19.23	71	12.73	2.44	8.47	1.01	5.15	0.94	2.71	0.41	2.81	0.41	356.73	334.84	21.9	0.72
Averages																		
CS M	31.3	56.2	5.89	20.3	3.76	0.64	2.82	0.43	2.21	0.47	1.49	0.22	1.44	0.24	127.34	118.04	9.31	0.64
US1	8.3	18.9	1.99	7.4	1.37	0.28	1.14	0.16	0.94	0.17	0.54	0.08	0.61	0.09	41.97	38.24	3.73	0.68
MSM	12.8	26.3	2.98	11.1	2.15	0.43	1.97	0.32	1.96	0.42	1.33	0.21	1.4	0.2	63.55	55.72	7.83	0.67
FS M	19.6	41.3	4.39	16.4	3.03	0.65	2.45	0.34	1.94	0.39	1.14	0.17	1.14	0.18	93.1	85.34	7.76	0.75
VFS M	40.4	83.1	9.16	34.4	6.5	1.19	5.66	0.88	5.48	1.12	3.41	0.52	3.56	0.55	195.94	174.77	21.17	0.64
Mud M	72.5	157	19.23	71	12.73	2.44	8.47	1.01	5.15	0.94	2.71	0.41	2.81	0.41	356.73	334.84	21.9	0.72
Av S M	24.4	49.4	5.4	20	3.77	0.72	3.21	0.49	2.96	0.61	1.87	0.29	1.93	0.3	115.42	103.75	11.67	0.68
SAS1M	28.3	51	5.48	19	3.57	0.66	2.54	0.38	1.84	0.41	1.3	0.2	1.22	0.21	116.08	107.99	8.09	0.73
QAS12M	14.1	30	3.41	12.9	2.54	0.51	2.44	0.4	2.49	0.54	1.69	0.27	1.8	0.26	73.22	63.33	9.89	0.7
SAS13M	33.9	71	7.73	29.1	5.45	1.04	4.66	0.69	4.26	0.86	2.55	0.39	2.66	0.41	164.68	148.21	16.47	0.69
QAS14M	13.6	26.1	2.8	10	1.85	0.34	1.6	0.26	1.63	0.33	1.1	0.17	1.11	0.19	61.09	54.7	6.39	0.58
SAM	32.4	65.5	7.11	26.4	4.93	0.94	4.08	0.61	3.6	0.74	2.21	0.34	2.27	0.35	151.42	137.24	14.18	0.7
QAM	13.9	28.2	3.14	11.7	2.24	0.43	2.07	0.34	2.11	0.45	1.43	0.23	1.5	0.23	67.88	59.53	8.35	0.65
Standards and reference rocks																		
UCC	30	64	7.1	26	4.5	0.88	3.8	0.64	3.5	0.8	2.3	0.33	2.2	0.32	146.37	132.48	13.89	0.65
PAAS	38.2	79.6	8.83	33.9	5.55	1.08	4.66	0.77	4.68	0.99	2.85	0.4	2.82	0.43	184.76	167.16	17.6	0.65
NASC	31	67	n.r.	27.4	5.6	1.2	5.2	0.85	n.r.	n.r.	n.r.	n.r.	3.1	0.46	141.81	132.2	9.61	0.68
Phan Sh	38.8	82	n.r.	32.3	5.75	1.14	5.22	0.81	n.r.	n.r.	n.r.	n.r.	2.95	0.47	169.44	159.99	9.45	0.68
Rah St	20.1	48	7.2	20.2	3.5	1	2.1	0.3	1.7	0.3	0.8	0.1	1	0.1	106.4	100	6.4	n.r.
Fein St	37.3	78	8.7	29.5	5.7	0.4	5.1	0.7	4.5	0.8	2.2	0.4	2.8	0.5	176.6	159.6	17	n.r.
Av. AC	33.5	71.3	8.37	27.4	5.21	0.53	4.43	0.61	3.88	0.69	1.89	0.33	2.4	0.41	160.99	146.35	14.64	n.r.
Duheil	30.6	47.3	6.5	26	6.1	1.6	5.4	0.9	4.7	0.9	2.3	0.3	2.8	0.3	135.7	118.1	17.6	n.r.
ArabM	25.9	60.2	7.4	28.6	5.9	1.8	5.3	0.8	3.8	0.7	1.9	0.2	2.1	0.3	144.9	129.8	15.1	n.r.
Monzg	39.9	86.7	10.9	45.4	8.55	2.39	6.57	0.98	3.93	0.64	1.67	0.23	1.42	0.19	209.47	193.84	15.63	n.r.

n.d. – not determined, n.r. – not recorded in the reference, other abbreviations are in Table 2.

grams of each ground sandstone and mudstone sample were sent to the laboratories of the Australian Laboratory Services Arabia (ALS Arabia) in Jeddah, Saudi Arabia, for chemical analysis.

Thirty-eight TEs and REEs were analyzed by means of an Inductively Coupled Plasma Mass Spectrometer (ICP-MS) following lithium borate fusion, whereas the major elements were analyzed using an Inductively Coupled Plasma-Atomic Emission Spectroscopy (ICP-AES). Loss on ignition (LOI) was determined at 1,000 °C using LECO TGA ANALYZER apparatus. International reference standards were used, and duplicate analyses were carried out to monitor precision and accuracy (~1% for major elements and < 5% for trace elements).

The abundance of the TEs and the various REEs, the  $\Sigma$ REEs,  $\Sigma$ LREEs,  $\Sigma$ HREEs and Eu/Eu\* for individual samples of each suite, means of values for the grain-size grades, the means of the average sandstone and mudstone, the standards and the reference rocks are listed in Table 2 and Table 3, respectively. In addition, the major elements abundance is taken from Amireh (2020) and listed in Supplementary Table 1 and represented in box-whisker diagrams (Fig. 8). The reasons of this overlap will be mentioned below in the geochemistry section.

Silver and tellurium attained values above the detection limit only in sample SR1, located immediately above the Rum Unconformity. Scandium was calculated on the basis of the ratio of Sc/V (0.13) in the upper continental crust (UCC), using data from Taylor and McLennan (1985), and McLennan (2001), after considering the ratios of Sc/Ti, Sc/Y, Sc/La, and Sc/Al, where the ratio of Sc/V gave the closest data to the actual values, measured in 7 reference standard rocks. The latter are the upper continental crust (UCC), analyzed by Rudnick and Gao (2003); the UCC, analyzed by Wedepohl (1995); the Late Proterozoic basalt, analyzed by Condie (1993); the Post Archaean Australian shales (PAAS), analyzed by Nance and Taylor (1976); the North American shale composite (NASC), and Phanerozoic shale and sandstone, analyzed by Condie (1993). Taylor and McLennan (1985) and McLennan (2001) used a similar approach in their Sc calculations.

To assess the influence of the provenance controlling the REE and TE content of the sandstones and mudstones, the siliciclastic succession investigated was split into four sandstone suites: subarkosic arenite suites 1 and 3, quartz arenite suites 2 and 4, and one mudstone suite (Tab. 1). Each sandstone suite has a specific stratigraphic position, mineral, and chemical composition (Tab. 1). Moreover, to evaluate the influence of hydraulic sorting during transport and deposition, the siliciclastics studied were grouped on the basis of decreasing mean grain size ( $M_1\Phi$ ) into 5 size-grade groups: coarse sand (0–1 $\Phi$ ), medium sand (1–2 $\Phi$ ), fine sand (2–3 $\Phi$ ), very fine sand (3–4 $\Phi$ ), and mud (silt to clay; >8 $\Phi$ ). The coarse sand group consisted of 7 samples: SD1, SD3, SD7, SD9, SR1, US1 and R1. The medium sand group consisted of 20 samples: R4, UI17, SR10, AK15, US4, R9, UI1, DS1, UI5, DS2, HM8, K1, J25, UI9B, K6, DS6, DS15, SR5, US10 and D19. The fine sand group consisted of 15 samples: AK2, TB9, US12, TB13, AM5, K3, AK11, AK6, TB1, AM1, AM8, D23, H9, D3, and D10. The very fine sand

group consisted of 16 samples: DMZ10, DMZ12, DMZ13, BF1, DMZ1, BT2, TB4, D5A, H6, RS3, KH2, BFS10, RS5, KH4, RS11, and KH1. The mud group consisted of 12 samples: H1, BT6, LOM28, MOM12, LS8, PTK1, TM7, TMK40, TAR13, JH17, JA10B, and CrZ7. The mean grain size of each sample ( $M_1\Phi$ ) can be seen in Table 1.

To model the interrelationships between the studied major, trace, and REE elements, and some petrographic parameters (mica, opaque heavy minerals, and garnet), Pearson's product moment correlation coefficient was used to construct a correlation matrix (Supplementary Tabs 4, 5), using Microsoft Office 365 Edition Excel sheet statistical functions. In general, for 58 measured data points with -2 degrees of freedom, the significant correlation coefficient value at the 95% significance level is  $\geq 0.26$ . The description of the correlation coefficients employed here is as follows: excellent correlation, if  $r$  is above 0.9; very good, if  $r$  ranges between 0.8 and 0.89; good, if  $r$  ranges between 0.7 and 0.79; fairly good, if  $r$  ranges between 0.5 and 0.69; and weak correlation, if  $r$  ranges between 0.26 and 0.49. Correlations of less than < 0.26 are insignificant.

Moreover, correlation coefficient matrices were constructed for each of the subarkosic arenites (33 samples) and the quartz arenites (25 samples) separately, since each group has the same mineral composition, thus there should be a significance for the correlation coefficients between the major elements, TEs, REEs, and modal parameters for each group. Because of the space limitations on this paper, the correlation matrices for all elements in the subarkosic arenites and quartz arenites can be supplied upon request. The significant correlation value at the 95% significance level for the subarkosic arenites ( $n = 33$ ) should be equal to or greater than 0.35 and for the quartz arenites ( $n = 25$ ) should be equal to or greater than 0.40.

Positive correlations indicate proportional relationships and negative correlation indicates inversely proportional relationships. In most cases, the correlation coefficients between elements, belonging to the two types of sandstone, are almost identical to the corresponding correlations, belonging to all of the suites together, unless otherwise stated.

The possible effect of the authigenic minerals on the correlation coefficients between the TEs and REEs contained in detrital minerals can be ruled out. This is due to the low amounts of TEs and REEs in these authigenic minerals that in turn have a very small, modal abundance in comparison with those of the detrital minerals (Supplementary Tabs 2, 3). This recorded correlation between the various TEs, REEs, major elements, and few modal abundances of certain minerals gives consistent and justifiable results, concerning their distribution in the different hosting minerals.

The index of chemical alteration (CIA) was calculated, using the formula:

$$CIA = 100 \times [Al_2O_3 / (Al_2O_3 + CaO^* + Na_2O + K_2O)],$$

where these oxides are represented as molar concentration and CaO\* represents the CaO value in the silicate minerals, calculated after correction for CaO in the carbonates and apatite, K<sub>2</sub>O in authigenic illite, and P<sub>2</sub>O<sub>5</sub> in apatite. The calculated CIA values are listed in Supplementary Table 1. The Eu/Eu\* =  $Eu_n / (Eu_n \times Gd_n)^{1/2}$  value was used after Condie (1993).

**Table 4**

Element abundance (ppm), element oxides abundance (in wt.%), and elemental ratios characteristic for standard felsic, mafic, recycled source rocks, UCC, and their values in the investigated sandstone (58 samples).

Element/ Elemental ratio	Mean of			UCC Taylor and McLennan (1985), McLennan (2001)
	felsic source rocks	mafic source rocks	sandstone studied (n = 58)	
Ba	652.5	209.5	343.13	550
Cr	14.4	211.56	29.31	83
Hf	6.5	2.24	9.68	5.8
Ni	9.33	81.56	12.17	44
Rb	140.75	36.01	41.68	112
Th	22.18	1.36	17.57	10.7
Zn	36.5	96.27	23.76	71
Zr	194	100.28	379.24	190
Cu	8.5	75.07	12.32	25
Sc	3.77	35.88	3.25	13.6
TiO <sub>2</sub>	0.22	1.24	0.41	0.68
Th/Sc	6.2	0.04	3.92	0.75
Cr/Th	1.1	361.53	5.02	7.76
Al <sub>2</sub> O <sub>3</sub> /TiO <sub>2</sub>	66.79	13.07	16.47	22.21
Ba/Sr	3.94	0.8	2.71	1.57
Y/Ni	3.55	0.46	2.2	0.5
Ce/Th	6.57	28.63	8.43	5.98
Ti/La×20	2.06	37.13	4.56	6.83
Ti/Zr	7.94	76.15	7.21	21.58
Cr/Ni	0.98	2.45	3.82	1.89
SiO <sub>2</sub>	73.84	50.22	89.19	65.89

The mean of felsic source rocks is compiled from: Proterozoic granite (Condie, 1993), Rahma Suite and Hummat Feinan Suite of the Aqaba Complex (Jarrar *et al.*, 2003), and the Danburg granite (Cullers, 1988). The mean of mafic source rocks is compiled from average mid oceanic ridge basalt (AMORB, White and Klein, 2013), Late Proterozoic basalt (Condie, 1993), Duheila hornblendic Suite (Jarrar *et al.*, 2003), Qunai monzogabbro (Ghanem and Jarrar, 2013), Araba mafic to intermediate Suite of the Aqaba Complex (Jarrar *et al.*, 2003), and the ultramafic Wet Mts. amphibolite (Cullers, 1994).

The term mud is used to include the clay-sized minerals, mainly clay minerals, plus the silt-sized detrital minerals, including quartz and the heavy minerals. This definition of mud and mudstone follows Tucker (2001). The terms for diagenetic processes, namely cementation, authigenesis, and neof ormation are used in the sense of Füchtbauer (1974). The abbreviations of the mineral names are followed after Warr (2021).

## RESULTS AND INTERPRETATIONS

### Modal composition

The modal analyses of the 58 sandstone samples, representing the four sandstone suites, are summarized in Supplementary Tables 2 and 3. The components of the sandstone consist of framework grains, detrital matrix, and cements. The framework grains are composed mainly of quartz: non-undulose, monocrystalline (Fig. 2A, C, D),

undulose, monocrystalline, and polycrystalline quartz. The first type of quartz is the major type, occurring in all samples of the four sandstone suites. The second and third types of quartz exist in variable amounts (modes) in the four sandstone suites. Next to quartz in abundance is K-feldspar, occurring mainly as orthoclase (Fig. 2B) in the samples of sandstone suites 1 and 3, less commonly as microcline (Fig. 2B), and very rarely as plagioclase in the same sandstone suites. Occasional, lithic fragments (Supplementary Tab. 2), detrital biotite (Fig. 2D), muscovite and chlorite, and transparent and opaque heavy minerals (thorite; Fig. 2E) are present in samples of sandstone suites 1 and 3.

The detrital matrix is mainly fine-grained, clayey, and reddish-brown-coloured, owing to detrital iron oxyhydroxides (Fig. 4E; Supplementary Tab. 2). However, XRD analysis of the powder random mounts reveals the following components: major illite and kaolinite (Fig. 4A), and less common montmorillonite and smectite/illite (S/I) as mixed layers (Supplementary Tab. 2). Furthermore, the detrital

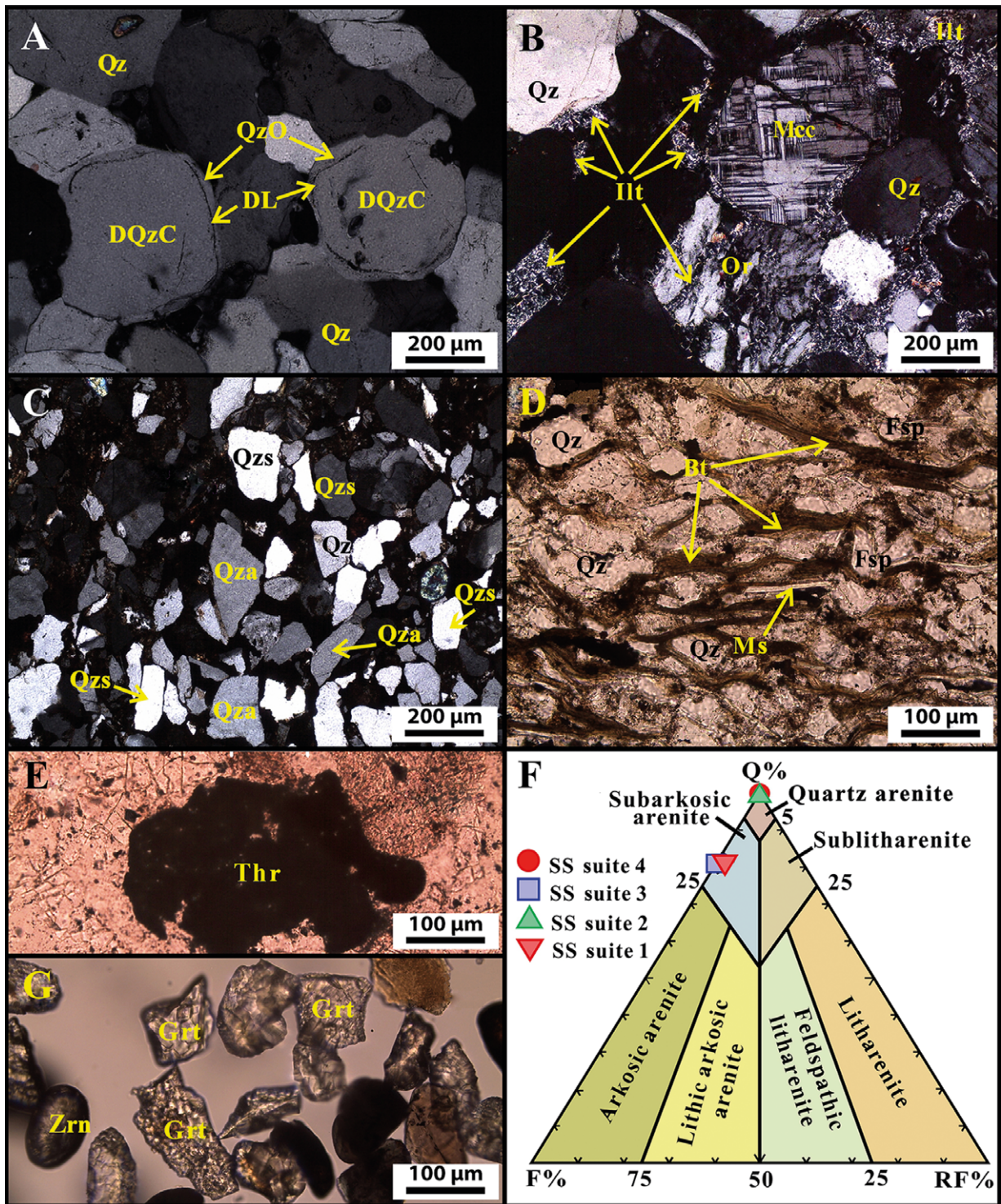


**Fig. 2.** Photomicrographs and a triangular diagram illustrating: **A.** Photomicrograph of quartz arenite of suite 4, composed of non-undulose, monocrystalline quartz. Note the well-rounded grains, the quartz overgrowth (QzO) separated from detrital quartz core (DQzC) by the dust line (DL). Thin section, quartz arenite suite 4, K6, XPL. **B.** Photomicrograph of subarkosic arenite of suite 1 composed of quartz (Qz), orthoclase (Or), microcline (Mcc) and detrital illitic matrix (Ilt). Note that illite replaced the orthoclase along cleavage planes. Thin section, subarkosic arenite suite 1, SD1, XPL. **C.** Photomicrograph of quartz arenite of suite 2, consisting of angular, detrital quartz grains (Qza), and subangular to subrounded quartz grains (Qzs). Thin section, DS6, XPL. **D.** Photomicrograph, illustrating detrital biotite flakes (Bt) with less common muscovite (Ms) in the subarkosic suite 3, consisting mainly of quartz (Qz) and less common feldspar (Fsp). Thin section, H6, PLL. **E.** Photomicrograph, illustrating thorite (Thr) replacing possibly a detrital monazite in the coarse sandstone directly overlying the Rum Unconformity. Thin section, SR1, subarkosic arenite suite, PLL. **F.** Classification of the four sandstone suites as quartz arenite suites 2 and 4, subarkosic arenite suites 1 and 3, following the Q-F-RF (quartz-feldspar-rock fragments) classification of Amireh (2018). **G.** Photomicrograph, showing detrital garnet grains (Grt) in subarkosic arenite suite 3. Note the sharp edges of the garnet grains and the surface marking features, due to intrastratal solution, whereas this diagenetic process does not affect the zircon grain (Zrn). Grain mount, sample D19, PPL.

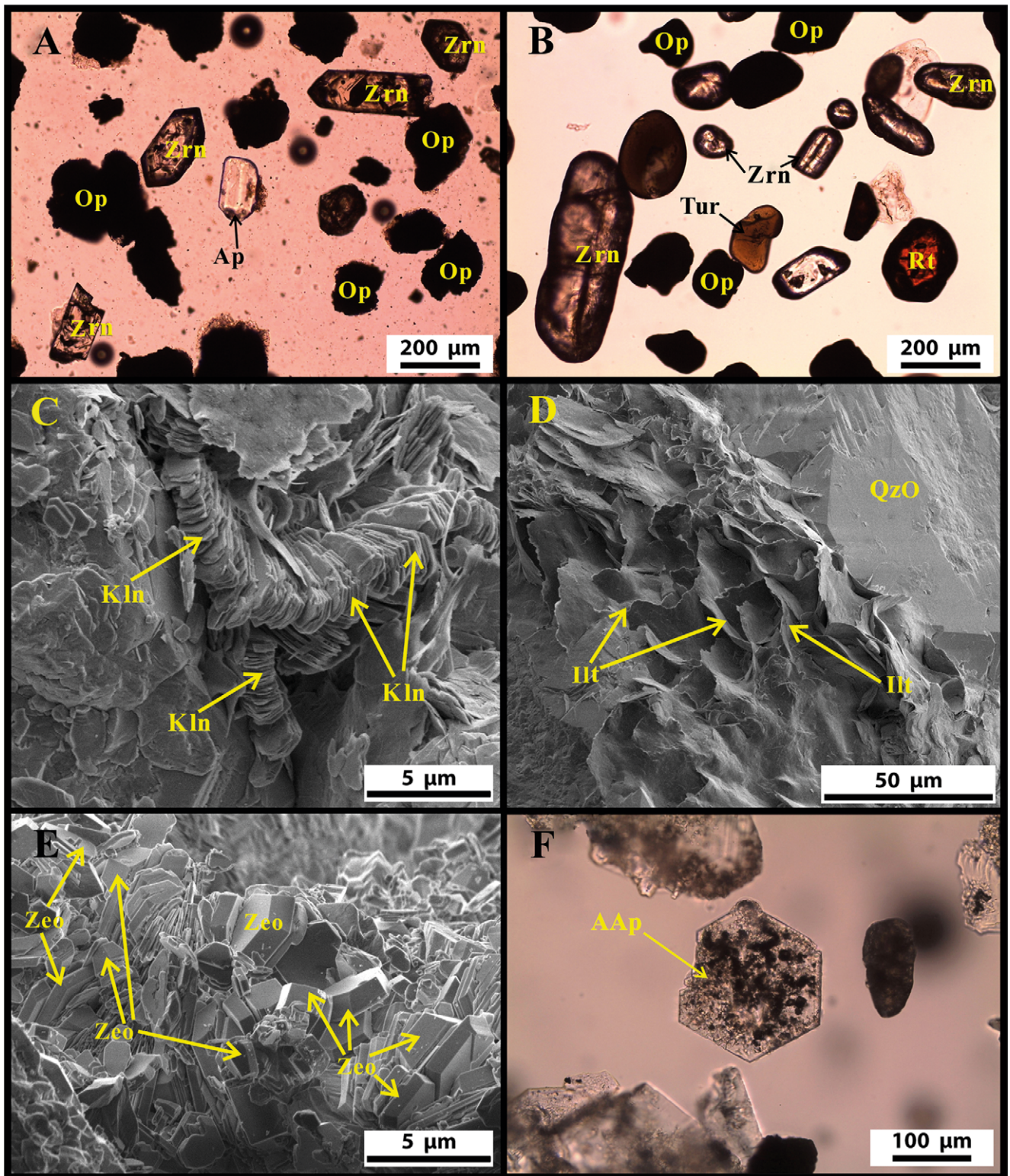


**Fig. 3.** Photomicrographs and SEM images illustrating: **A.** Photomicrograph, showing angular zircon grains (Zrn) and one subangular, detrital apatite (Ap), and opaque heavy minerals (Op) in the subarkosic arenite suite 1. Heavy mineral grain mount, sample SD7, PLL. **B.** Photomicrograph, showing rounded heavy minerals zircon (Zrn), rutile (Rt), tourmaline (Tur), opaques (Op). Heavy mineral grain mount, quartz arenite suite 4, sample R9, PLL. **C.** SEM image, showing kaolinite (Kln), characterized by book-like aggregates of crystals, quartz arenite suite 2, sample UI9B. **D.** SEM image, illustrating neoformed illite (Ill), filling a fracture adjacent to a quartz grain, characterized by a euhedral overgrowth (QzO), subarkosic arenite suite 1, sample SD7. **E.** SEM image, illustrating a swarm of neoformed zeolite crystals (Zeo), subarkosic arenite suite 1, sample SD3. **F.** Photomicrograph for “rare” authigenic apatite (AAp) without a seed, characterized by euhedral, hexagonal crystal faces. Heavy mineral grain mount, subarkosic arenite suite 1, sample AK6, PLL.

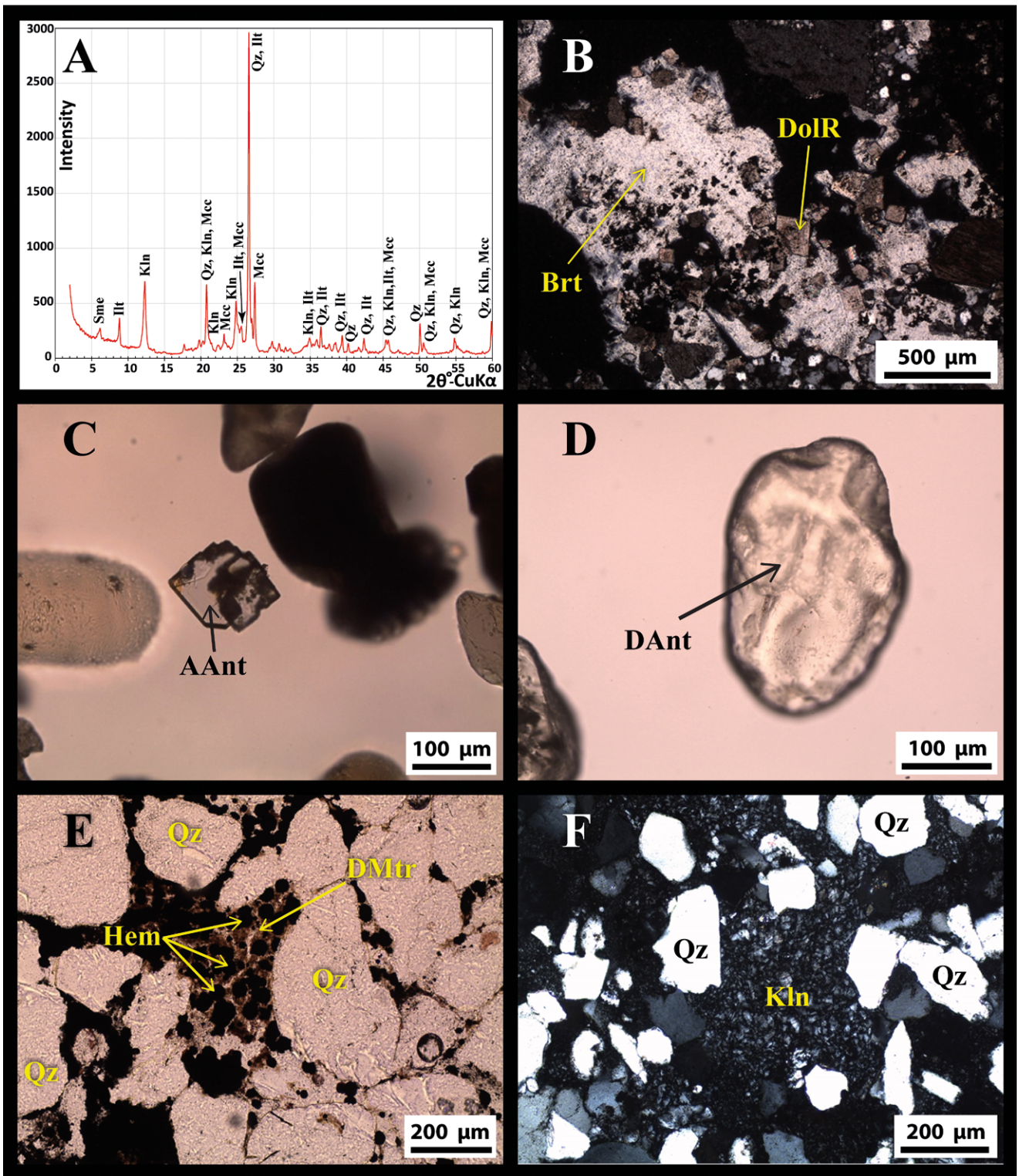


**Fig. 4.** XRD chart and photomicrographs illustrating: **A.** XRD chart for a random-oriented powder sample (H6), subarkosic arenite suite 3, revealing presence of smectite (Sme), illite (Ill), kaolinite (Kln), quartz (Qz) and microcline (Mcc). **B.** Photomicrograph, showing barite cement (Brt), which is partly replaced by dolomite rhombs (DoIR), subarkosic arenite suite 3, sample KH2, XPL. **C.** Authigenic anatase (AAnt), illustrating typical, euhedral crystal boundaries and tabular or platy form, subarkosic arenite suite 3, sample RS5. Heavy mineral grain mount, PPL. **D.** Detrital anatase (DAnt) characterized by well-rounded form and an abraded boundary, subarkosic arenite suite 1, sample SD3. Heavy mineral grain mount, PPL. **E.** Photomicrograph, showing authigenic hematite as hexagonal crystals (Hem), replacing detrital ferruginous clayey matrix (DMtr), and detrital quartz grains (Qz), subarkosic arenite suite 3, sample H9, PPL. **F.** Photomicrograph, showing authigenic kaolinite (Kln) with a “worm-like” texture, and detrital quartz grains (Qz), subarkosic arenite suite 1, sample AK6, XPL.

clay minerals of the matrix and part of the neoformed clay minerals were isolated by the gravitational settling technique, following Stoke's Law and identified by XRD, employing the special mounts of clay minerals, as mentioned in the methodology section. Occasional, dispersed, silt-sized quartz grains in the matrix were encountered in all sandstone samples. It is important to distinguish between the detrital clay minerals, constituting the matrix, and the neoformed clay minerals. The detrital clay minerals were seen in thin sections under plane-polarized light as inhomogeneous, very fine-grained particles, the type of which cannot be resolved by the polarized microscope. The neoformed clay minerals, on the one hand, appeared under plane-polarized light as a homogenous, clear, colourless substance, free of impurities, filling the interstitial pore spaces between framework components. Furthermore, under crossed-polarized light, they have mainly a first-order interference colour and there is a specific texture for each clay mineral. For example, kaolinite exhibits a texture of "worms" of various sizes (Fig. 4F). In SEM images, kaolinite appears as "books" composed of euhedral, hexagonal to pseudohexagonal plates (Fig. 3C).

The cements consist mainly of syntaxial quartz overgrowths (Fig. 2A, Supplementary Tab. 2), which is ubiquitous in all samples of the four sandstone suites. Quartz cement is followed in modal abundance by kaolinite (Fig. 3C; Supplementary Tab. 2) and dickite. The former is encountered in most samples of sandstone suites 1, 2 and 3, whereas the latter occurs only in the lower Cambrian sandstone samples of suites 1 and 2 (SR1, SR5, SD1-9, AK1-11, and U11-17), since it requires a great burial depth for its neoformation (Amireh, 1994; Amireh *et al.*, 1994b). Iron oxyhydroxides, particularly hematite (Fig. 4E) and calcite (Supplementary Tab. 2), are the cements second and third in abundance that occur in most of samples of the four sandstone suites. Less common cements include illite (Figs 2B, 3D), which exists only in the lower Cambrian sandstones of suites 1 and 2 (Fig. 2B, Supplementary Tab. 2), similar to dickite. Dolomite cement is restricted to samples of the shallow-marine sandstone suite 3 (Supplementary Tab. 2). Minor, authigenic phases include epitaxial feldspar overgrowths (Supplementary Tab. 2), and rare poikilotopic or patchy barite cement (Fig. 4B). Additionally, authigenic anatase (Fig. 4C), authigenic apatite (a rare occurrence without a "seed", Fig. 3F) and apatite overgrowths (Amireh, 2020, fig. 3D), and zeolite minerals (Fig. 3E) were encountered.

According to the framework and matrix modes of the sandstones, they are classified as subarkosic arenites and quartz arenites (Fig. 2F), following the classification of Amireh (2018).

The modal heavy minerals (Supplementary Tab. 3) include the ubiquitous, transparent, ultrastable zircon ( $ZrSiO_4$ , Fig. 3A, B), rutile (Fig. 3B) with its polymorphs detrital anatase ( $TiO_2$ ; Fig. 4D) and brookite, tourmaline (Fig. 3B), detrital apatite (Fig. 3A), garnet (Fig. 2G), barite, thorite ( $ThSiO_4$ ; Fig. 2E), titanite, monazite ((LREE, Th, U)  $PO_4$ ), and rare hornblende. The modal, opaque heavy minerals (Supplementary Tab. 3; Fig. 3A, B) are mainly hematite as a cement and as an alteration product of ilmenite (Amireh, 2020, fig. 5A, B), and less commonly ilmenite and thorite.

However, other opaque heavy minerals are inferred in this study from the chemical analysis, including ilmenorutile ((Ti, Nb,  $Fe^{3+}$ ) $O_2$ ), xenotime ((Y, HREE) $PO_4$ ), and euxenite ((Y, Ca, Ce, U, Th)(Nb, Ti, Ta) $_2O_6$ ), as will be shown in the section on trace elements below.

## GEOCHEMISTRY

### Major elements

Amireh (2020) recorded the concentration of the major elements in the siliciclastic succession under investigation. Since these data were necessary for illustrating the relationships between the major elements, the TEs and REEs, and the detrital and authigenic minerals, and in order not to repeat the same chemical analysis, his data have been employed here (Supplementary Tab. 1). Figure 8 portrays the abundance and variability of the major elements in the form of a box-whisker diagram. This type of data presentation was adopted because the sandstones studied were grouped into 4 suites with a small number of sample points (< 30). Such small numbers of samples do not allow determination of the type of distribution of the elements analyzed, belonging to a suite and accordingly expressing their chemical variability by means of the proper statistical moments. To overcome this problem, the box and whisker charts were constructed to view and visually display the chemical variability of the trace, rare-earth, and major elements studied. The charts constructed are displayed in Figures 6, 7, and 8. The lines extending parallel from the boxes refer to the variability outside the upper and lower quartiles (Q3 and Q1). Dots outside the boxes are outliers. The x inside the box refers to the median and the line to the mean. Major-element whiskers show that concentrations of  $SiO_2$ ,  $Al_2O_3$ , and CIA values exhibit a great deal of chemical variability and outliers in all the suites studied.

### Distribution and behavior of the trace elements

The abundance of TEs and the REEs were portrayed as spider diagrams, normalized to the upper continental crust (UCC; Fig. 5) of Taylor and McLennan (1985) and McLennan (2001), since the source rocks were mainly granitoids (Amireh, 2020), similar to the average composition of the UCC, as discussed below. Moreover, the TEs are portrayed as a box-whisker diagram (Fig. 6). The TE whiskers show clearly that Ba, Sr, Zn, and Zr exhibit greater variability in all suites, whereas the rest of the trace elements and especially some of them, exhibit a large variability in certain suites.

It appears from the spider diagrams (Fig. 5) that most elements in the quartz arenite suites 2 and 4 and subarkosic arenite suite 1 exhibit depleted (negative) anomalies relative to their UCC values, except barium, which is enriched in three samples, owing to their barite cementation. On the other hand, the subarkosic arenite suite 3 is enriched (positive anomalies) in some elements, particularly the REEs, Ba, Zr, Hf, Th, and Y, whereas the mudstone is enriched in most of the TEs and all of the REEs. Additionally, the abundance variation of some characteristic TEs and REEs with

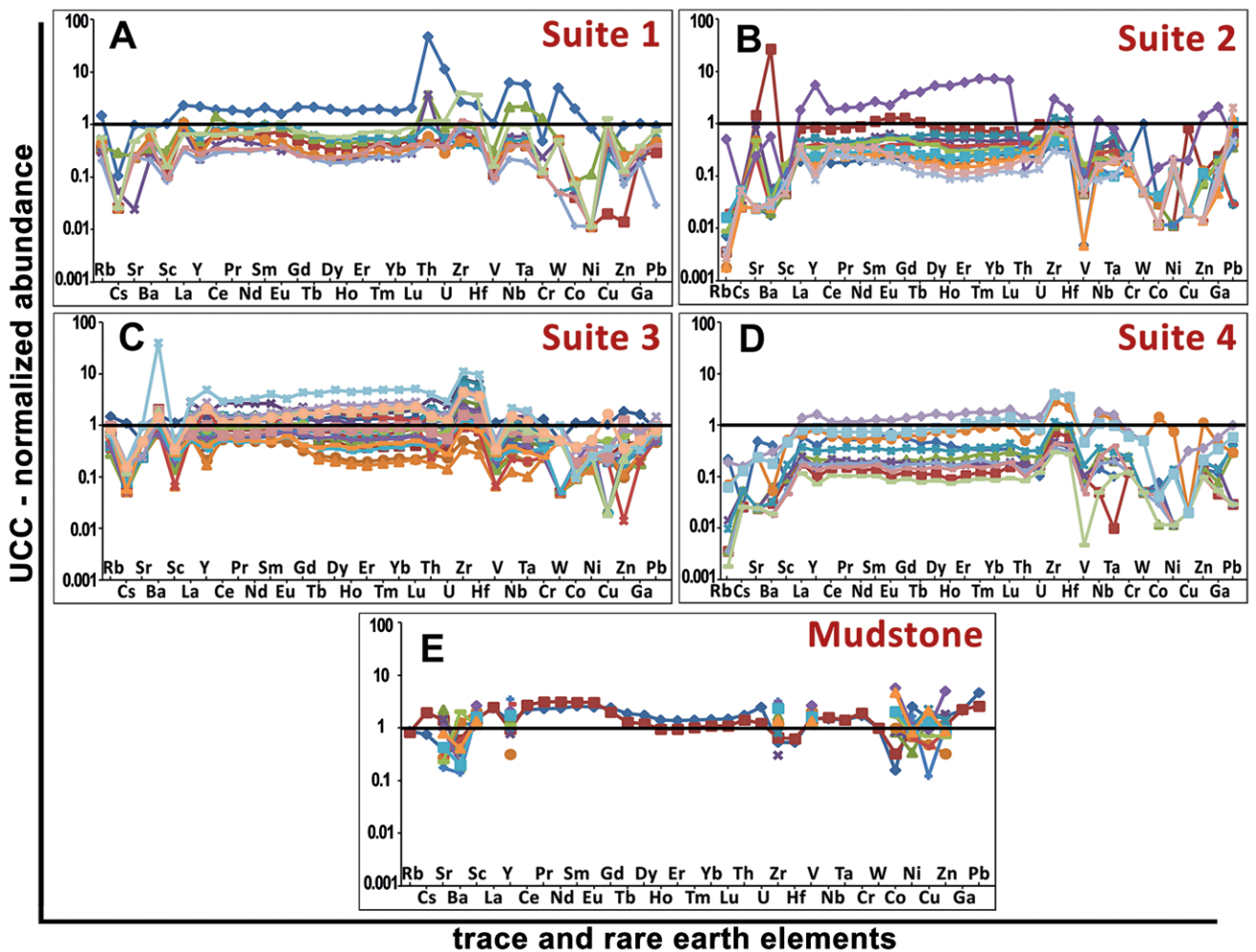


Fig. 5. UCC-normalized multi-element diagrams, illustrating the abundance of the trace and rare earth elements arranged from Rb to Pb, in the four sand size grades and the mudstone grade. CS – coarse sand, MS – medium sand, FS – fine sand, VFS – very fine sand.

decreasing grain size (increasing  $\Phi$  values), from coarse sand to mud size (clay-silt) is depicted in Figure 9.

It appears from Figures 5 and 9 and Table 2 that most of the TEs are depleted in the coarse, medium, and fine sand grades relative to the UCC, but are partially enriched in the very fine sand and the mud fractions.

Moreover, all the TEs, excluding Ba, exhibit a systematic increase in abundance with decreasing size, from coarse sand (represented by sample US1, not affected by hydrothermal metasomatism) to the mud fraction (Tab. 2). Accordingly, the mud fraction is enriched in all the TEs, associated with detrital clay minerals, excluding Zr, Hf, and Y that are concentrated in zircon in the very fine sand (Tab. 2; Fig. 9I, J), which can be attributed to hydraulic sorting. However, Ta and Nb are mainly in the detrital, silt-sized Ti-bearing minerals, e.g., rutile, anatase-brookite, titanite, and ilmenorutile, as well as in authigenic anatase (Fig. 4C), which captured a small portion of them during diagenesis, as will be discussed in the section of diagenesis. From another aspect, the subarkosic arenite suites 1 and 3 invariably exhibit a higher concentration of all the TEs, compared to the quartz arenite suites 2 and 4 (Tab. 2), which can be attributed to provenance effects. In other words, this could be attributed to derivation of the subarkosic arenites from

the granitoid source rocks of the Arabian Shield, rich in TEs, whereas the quartz arenites were derived from the Palaeozoic-Mesozoic siliciclastic strata, very poor in TEs. The TEs are classified into the following groups.

#### *Large-ion, lithophile elements (LILEs, Rb, Ba, Sr, Cs)*

Rubidium, Ba, and Sr are depleted in the sandstone suites and in the mudstone suite in comparison with UCC and PAAS (Tab. 2). This could indicate strong weathering conditions dominating the source rocks and affecting the sediments during the long fluvial pathway, or the recycling of older sedimentary rocks. However, barium has its maximum abundance in the very fine sand (Tab. 2, excluding the three samples cemented by barite), which is associated with minute K-feldspar grains that are concentrated in this size ( $K_2O = 2.8$  wt.%; Supplementary Tab. 1); they were removed preferentially from the coarser sand fractions by abrasion during transport, owing to their mechanical instability. This conclusion is corroborated by the excellent correlation between Ba and K ( $r = 0.95$  in all suites, and 0.85 in subarkosic arenite; Supplementary Tab. 4).

On the other hand, Cs is depleted in the sandstones, but is enriched in the mudstones, relative to the UCC and PAAS values (Tab. 2). This can be attributed to its occurrence

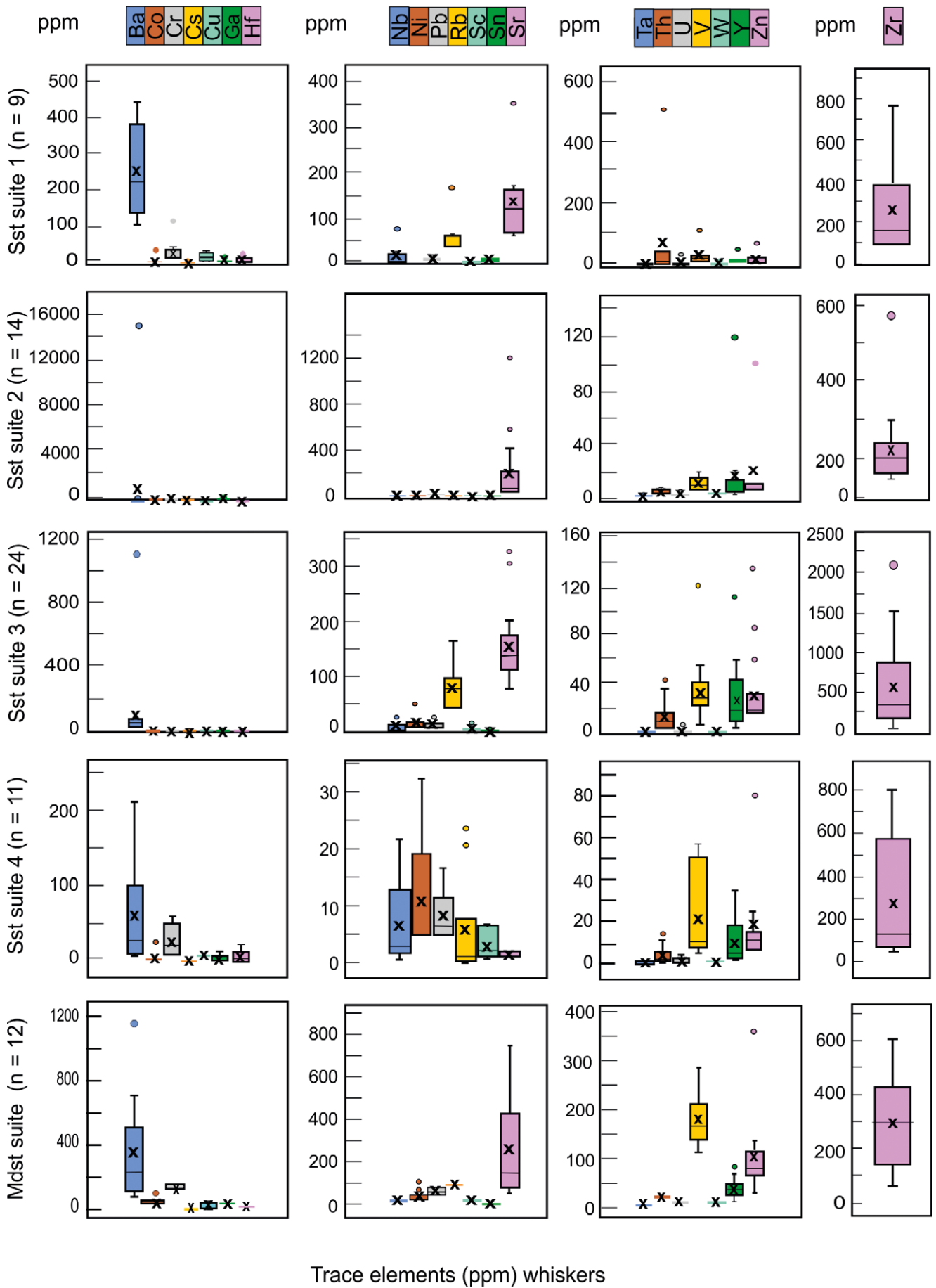
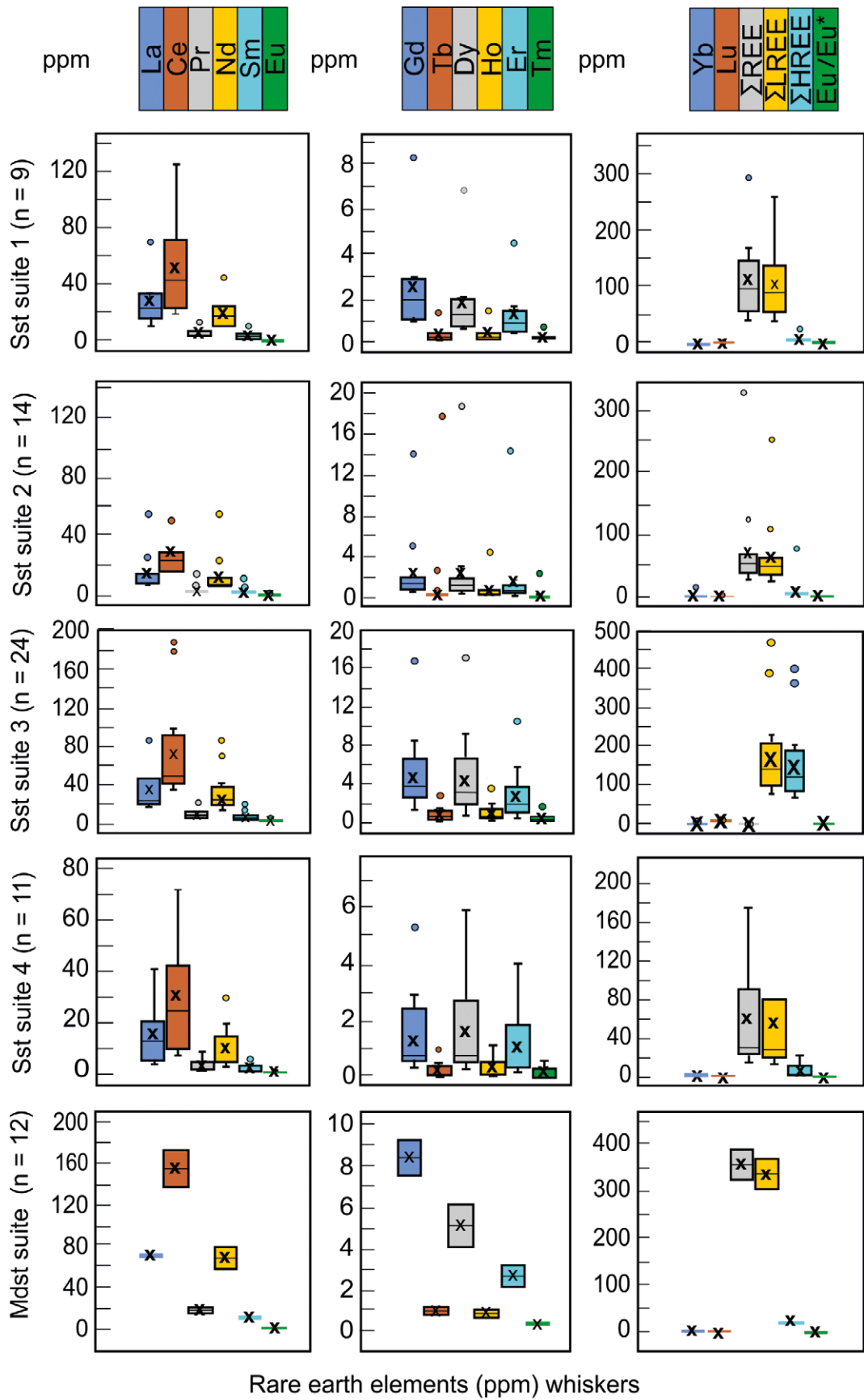
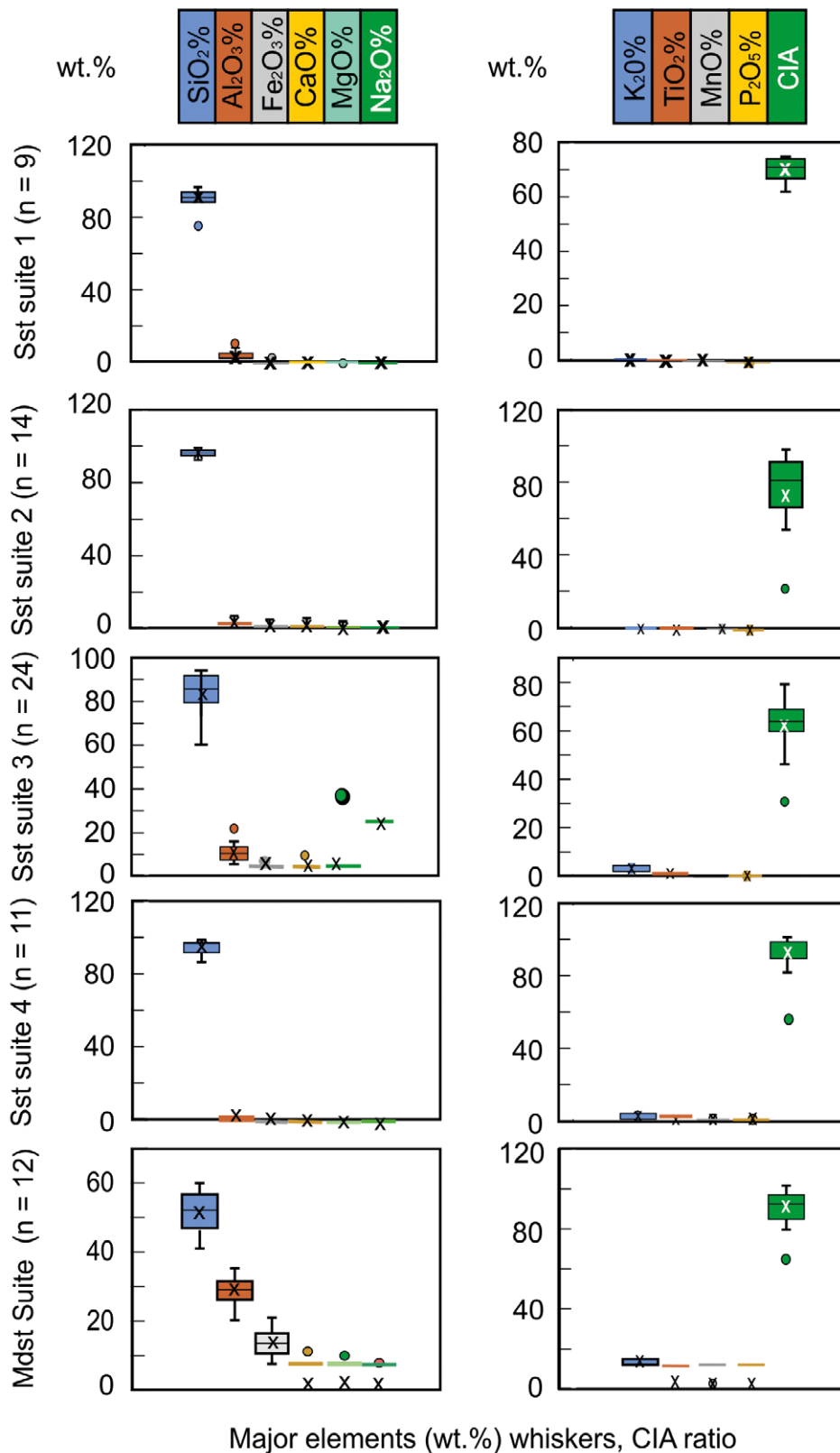


Fig. 6. Box-whisker diagram for the trace elements Ba, Co, Cr, Cs, Cu, Hf, Nb, Ni, Pb, Rb, Sc, Sr, Ta, Th, U, V, W, Y, Zn, and Zr.



**Fig. 7.** Box-whisker diagram for the rare earth elements La, Ce, Pr, Nd, Sm, Eu, Gd, Tb, Dy, Ho, Er, Tm, Yb, Lu, ΣREE, ΣLREE, ΣHREE, and Eu/Eu\* anomaly.



**Fig. 8.** Box-whisker diagram for the major elements  $\text{SiO}_2$ ,  $\text{Al}_2\text{O}_3$ ,  $\text{Fe}_2\text{O}_3$ ,  $\text{CaO}$ ,  $\text{MgO}$ ,  $\text{Na}_2\text{O}$ ,  $\text{K}_2\text{O}$ ,  $\text{TiO}_2$ ,  $\text{MnO}$ ,  $\text{P}_2\text{O}_5$ , and index of chemical alteration CIA.

entirely in the clay minerals, particularly montmorillonite. Rubidium substitutes for K in K-feldspar, illite and muscovite. Strontium is hosted by multiple mineral phases, since it does not correlate significantly with any major element or TE indicative of a specific mineral (Supplementary Tab. 4).

However, it is more concentrated in the mudstones, indicating its possible association with the detrital clay minerals, as revealed by its maximum abundance in the mudstone (257.2 ppm Sr, Tab. 2).

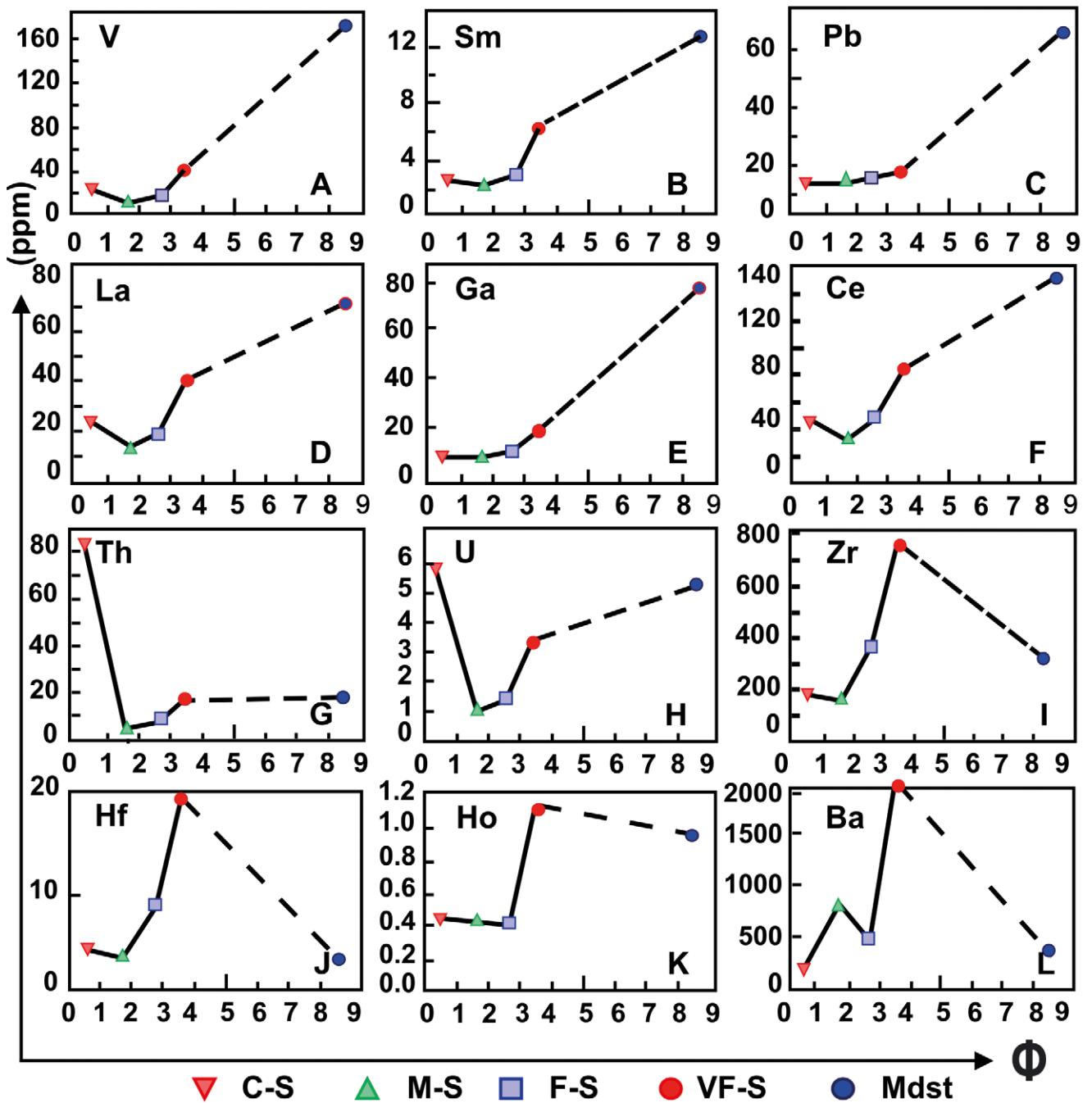


Fig. 9. Plots illustrating variation of mean abundances of some characteristic trace and rare earth elements with grain size. Note the vertical axis, representing the abundance in ppm, and the horizontal axis, representing the ( $\Phi$ ) grain size, and the dashed lines connecting the actually determined phi means of the very fine sand size and the proposed mean (8.5  $\Phi$ ) of the clay fraction, going through the various silt grades that are not determined.

**High-Field-Strength elements (HFSEs, Th, Zr, Hf, Y, U, Nb)**

Thorium is concentrated in the average sand and mud fraction 1.6 times, compared to its value in UCC lithologies (Tab. 2). In addition, it is more enriched in the very fine sand and the mud fractions, indicating its possible association with the detrital very fine sand-sized heavy minerals and the detrital clay minerals, respectively. Moreover, Th is highly enriched in the coarse sandstone, located above the Rum Unconformity, that was affected by hydrothermal metasomatism, which led to enrichment of it in the average sand.

It occurs mainly in the opaque mineral thorite, since Th shows excellent correlation with the modal opaque heavy minerals ( $r = 0.93$ ). The remarkable, excellent correlation between U and Th ( $r = 0.96$  in all sandstones, and 0.97 in subarkosic arenites, and 0.91 in quartz arenites) reflects the extensive isomorphism of  $U^{4+}$  and  $Th^{4+}$ , owing to similarities in charge and radius. Such a correlation may confirm the presence of thorite, as identified in thin sections (Fig. 2E) and in grain mounts of heavy minerals.

Zirconium and Hf show excellent correlation with each other ( $r = 0.997$  in all suites, 0.998 in subarkosic arenites,

0.99 in quartz arenites). They are concentrated in the average sand more than in the average UCC by ca. 2 and 1.7 times, respectively, and are highly enriched in the very fine sand (Tab. 2; Fig. 9I, J), hosted solely in zircon. Almost all the REEs correlate very well with Zr and Hf (Supplementary Tab. 4), indicating their principal occurrence in zircon, or even their substitution for Zr in the zircon crystalline structure. Moreover, Zr correlates very well with  $\text{TiO}_2$  ( $r = 0.85$  in all suites,  $0.82$  in subarkosic arenites, and  $0.85$  in quartz arenites) indicating the certain association of zircon with detrital rutile, anatase and brookite, and probably with titanite and ilmenite, all occurring in the silt-size fraction, as discussed below.

Yttrium shows fairly good to excellent correlation with Zr ( $r = 0.64$  in all suites,  $0.68$  in subarkosic arenite), Hf ( $r = 0.64$  in all suites,  $0.68$  in subarkosic arenites, and  $0.59$  in quartz arenites), and  $\text{TiO}_2$  ( $r = 0.63$  in all suites, and  $0.84$  in subarkosic arenites), indicating its association mainly with zircon and Ti-bearing heavy minerals. However, it has excellent correlation with  $\Sigma\text{HREEs}$  ( $r = 0.996$  in all suites,  $0.99$  in subarkosic arenites, and  $0.9996$  in quartz arenites), which is attributed to the similar charge and ionic size of Y and the HREEs. Therefore, Y and part of the REEs are associated with detrital heavy minerals, particularly xenotime. This result is indicated by the excellent correlation of Y with Yb ( $r = 0.98$  in all suites,  $0.98$  in subarkosic arenite,  $0.996$  in quartz arenite), the very good correlation with Nd ( $r = 0.83$ ) in all suites, excellent in quartz arenite ( $r = 0.95$ ), and very good in subarkosic arenite ( $r = 0.8$ ), good correlation with Ce ( $r = 0.76$ ) in all suites, excellent in quartz arenite ( $n = 0.93$ ), good correlation with La ( $r = 0.74$ ) in all suites, excellent in quartz arenite ( $n = 0.9$ ), weak correlation with V ( $r = 0.36$ ) in all suites, and the very weak correlation with  $\text{P}_2\text{O}_5$  ( $r = 0.13$ ) in all suites, but weak correlation in subarkosic arenite ( $r = 0.36$ ). The very weak to weak correlation of the latter is attributed to the occurrence of  $\text{P}_2\text{O}_5$  mainly in the major phase, apatite. Moreover, Y occurs in euxenite, as indicated by its good correlation with Ce ( $r = 0.76$ ) in all suites, excellent correlation in quartz arenite ( $r = 0.93$ ), fairly good correlation with Nb ( $r = 0.52$ ) in all suites, fairly good correlation with  $\text{TiO}_2$  ( $r = 0.63$ ) in all suites, but very good correlation in subarkosic arenite ( $r = 0.84$ ), weak correlation with Ta ( $r = 0.48$ ), weak correlation with U ( $r = 0.38$ ) in all suites, and very weak correlation with Ca ( $r = 0.29$ ), but weak correlation in quartz arenite ( $r = 0.4$ ), and very weak correlation with Th ( $r = 0.23$ ) in all suites. Again, the very weak to weak correlation of yttrium with Ca is attributed to the presence of calcite and dolomite cements that contain significant amounts of calcium.

Niobium and U abundances correlate excellently with each other ( $r = 0.94$ ) in all suites, and occur in the opaque heavy minerals, ilmenorutile and thorite, respectively. The presence of thorite was proved in the examination of thin sections and in the first paragraph of this section, whereas the presence of ilmenorutile is indicated by the excellent correlation of Nb with Ta ( $r = 0.99$ ) in all suites, as well as in each of the subarkosic arenites and quartz arenites ( $r = 0.996$ , and  $0.98$ , respectively), good correlation with  $\text{TiO}_2$  ( $r = 0.75$ ) in all suites, and very good correlation in quartz arenites ( $r = 0.86$ ), and weak correlation with  $\text{Fe}_2\text{O}_3$

( $r = 0.4$ ) in all suites. Moreover, its occurrence as an opaque heavy mineral is confirmed by the good correlation of Nb with the modal amounts of opaque heavy minerals ( $r = 0.79$ ) in all suites, but very good correlation in subarkosic arenites ( $r = 0.85$ ).

#### **Transition trace elements (TTEs, Ta, Cr, Co, Ni, Cu, Sc, V, Zn)**

Remarkably, all the TTEs are depleted in the average sand, and enriched in the mud fraction relative to the average UCC (Tab. 2), indicating their possible association with clay minerals, besides other heavy minerals. Tantalum occurs mainly in ilmenorutile. Cobalt correlates with an array of TEs, alumina, iron oxide and opaque heavy minerals (Supplementary Tab. 4), indicating its occurrence mainly in the opaque heavy minerals (ilmenite, hematite, thorite) and partly in illite. Chromium, Ni, V, and Zn correlate positively very well with each other, and well with  $\text{Al}_2\text{O}_3$ ,  $\text{Fe}_2\text{O}_3$ ,  $\text{MgO}$ ,  $\text{K}_2\text{O}$ , modal mica, opaque minerals, and  $\text{TiO}_2$ , and negatively with  $\text{SiO}_2$  (Supplementary Tab. 4). Therefore, they are mainly sorbed into illite and less commonly montmorillonite, and associated with rutile-anatase, biotite, ilmenite, and hematite. Probably, discrete minerals of each element, either detrital ones like chromite ( $\text{FeCr}_2\text{O}_4$ ), or authigenic ones such as sphalerite ( $\text{ZnS}$ ), are present within the opaque fraction.

Scandium increases in abundance with decreasing grain size from coarse sand to very fine sand, then markedly to mud size, and thus the mudstones are much more enriched in Sc than the average sand (Tab. 2). This result leads to the conclusion that Sc in the investigated siliciclastics is adsorbed onto the clay minerals (cf., Zhao and Zheng, 2015). Moreover, this conclusion is corroborated by the strong positive correlations of Sc with  $\text{Al}_2\text{O}_3$ ,  $\text{Fe}_2\text{O}_3$ ,  $\text{K}_2\text{O}$ , and  $\text{TiO}_2$ , and the negative correlation with  $\text{SiO}_2$  (Supplementary Tab. 4).

#### **Other elements (Pb, Ga, Sn, W)**

Lead correlates fairly positively with  $\text{Al}_2\text{O}_3$ ,  $\text{K}_2\text{O}$ , and  $\text{TiO}_2$ , and negatively with  $\text{SiO}_2$  (Supplementary Tab. 4), indicating its possible association with detrital K-feldspar and detrital rutile. Gallium correlates well with  $\text{Al}_2\text{O}_3$ ,  $\text{Fe}_2\text{O}_3$ , LOI,  $\text{K}_2\text{O}$ , Rb and modal mica (Supplementary Tab. 4), indicating its association mainly with illite and less commonly montmorillonite, biotite, and K-feldspar. Tin and W are present as cassiterite ( $\text{SnO}_2$ ), which is identified by SEM-EDS analysis, and possibly as scheelite ( $\text{CaWO}_4$ ), respectively, that are both present among the opaque heavy minerals.

#### **The abundance and distribution of the REEs**

The REEs could be subdivided into light (LREEs), La, Ce, Pr, Nd, Sm, and Eu, and heavy (HREEs), Gd, Tb, Dy, Ho, Er, Tm, Yb, and Lu. The REEs in the four sand size grades, the mudstone, the UCC, PAAS, NASC, and Phanerozoic shale were normalized relative to the CI carbonaceous chondrite (which is taken as a representative of the bulk Earth; Fig. 10). Figure 10A–E shows that the CI carbonaceous chondrite normalized REE patterns of the coarse, medium, fine, very fine sand, and the mud fraction and the Eu anomaly are

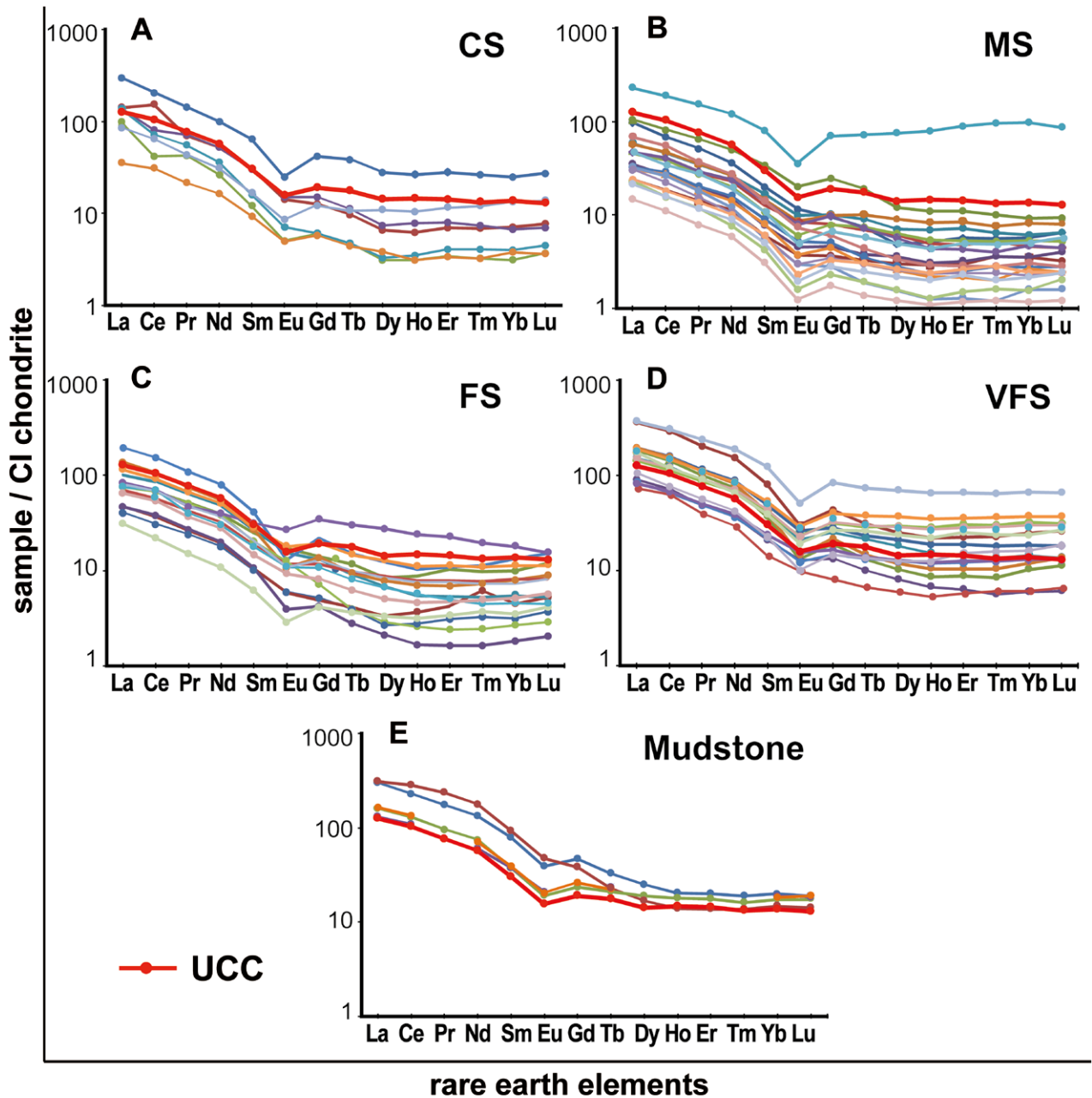


Fig. 10. CI chondrite-normalized REE patterns of: A–D coarse, medium, fine, and very fine sand grades, E two mudstone samples, UCC, PAAS, and NASC.

almost parallel to those of the UCC, i.e., LREE enrichment with a negative “Eu anomaly” (White, 2013). Moreover, an invariable pattern of LREE enrichment, but with a decline from La to Sm, and relatively flat HREE abundances is revealed. Additionally, a restricted variation of Eu depletion ( $\text{Eu}/\text{Eu}^*$  ranges from 0.64 to 0.75 in sands and attains 0.72 in muds) is apparent.

Furthermore, Table 3 illustrates that  $\Sigma\text{REEs}$ ,  $\Sigma\text{LREEs}$ , and  $\Sigma\text{HREEs}$  increase gradually from coarse sand (represented by US1 sample) to fine sand, then abruptly to very fine sand and abruptly increase to the mud fraction. Thus, the mud fraction is more enriched in REEs than the average sand and the UCC, PAAS and NASC (Tab. 3). In the mud fraction, most of the REEs are hosted in detrital, silt-sized,

$\text{TiO}_2$ -bearing minerals, as explained below. Minor amounts of the REEs are associated with the detrital clay minerals as indicated here by the weak positive correlation between  $\text{Al}_2\text{O}_3$  and  $\Sigma\text{REEs}$  ( $r = 0.42$ ) in all suites, weak correlation with  $\Sigma\text{LREEs}$  ( $r = 0.43$ ) in all suites, and weak correlation with  $\Sigma\text{HREEs}$  ( $r = 0.31$ ) in all suites and agree with the result reported by Condie (1991). Probably, the REEs are adsorbed on the crystal structure, or reside in the interlayers of clay minerals. However, the heavy minerals are the primary minerals hosting the REEs as shown next.

The values of  $\Sigma\text{REEs}$ ,  $\Sigma\text{LREEs}$ , and  $\Sigma\text{HREEs}$  in the average sand size are less than those of the UCC and the average Aqaba Complex, the possible source rocks (Tab. 3; Jarrar *et al.*, 2003). Thus, the average sand apparently is depleted in

$\Sigma$ REEs,  $\Sigma$ LREEs and  $\Sigma$ HREEs relative to the average UCC and the source rocks. However, this conclusion could be misleading, since the very fine sand is more enriched with  $\Sigma$ REEs,  $\Sigma$ LREEs and  $\Sigma$ HREEs than both the UCC and the source rocks (Tab. 3), which is attributed to hydraulic sorting of the heavy minerals, particularly zircon in the very fine sand grade. The much lower  $\Sigma$ REEs,  $\Sigma$ LREEs, and  $\Sigma$ HREEs in the coarse, medium and fine sand fractions, compared to both the UCC and the source rocks (Tab. 3), could be attributed to quartz dilution, resulting from hydraulic sorting and recycling, or due to extensive chemical weathering of the source rocks (cf., Nesbitt and Markovics, 1997), as discussed below.

Zircon and the Ti-bearing minerals (rutile, anatase, brookite, titanite, ilmenite, and ilmenorutile) are the primary heavy minerals hosting REEs, particularly in the very fine sand and silt sizes, respectively (Tab. 3). This conclusion is reached through the very good correlation of Zr with  $\Sigma$ REEs ( $r = 0.82$ ),  $\Sigma$ LREEs ( $r = 0.83$ ), and the fairly good correlation with  $\Sigma$ HREEs ( $r = 0.66$ ), and the very good correlation of Ti with  $\Sigma$ REEs ( $r = 0.83$ ),  $\Sigma$ LREEs ( $r = 0.84$ ), and the fairly good correlation with  $\Sigma$ HREEs ( $r = 0.63$ ). Furthermore, this result is corroborated by the maximum abundance of Zr in the very fine sand fraction (Tab. 2; Fig. 9I), due to the hydraulic sorting of ultrastable zircon in this size fraction. The maximum abundance of  $\text{TiO}_2$  occurs in the mud fraction (Tab. 2; Fig. 9H) and is attributed to hydraulic sorting of detrital, silt-sized, less mechanically stable rutile (Amireh, 1991) in this mud fraction. However, a very small portion of  $\text{TiO}_2$  is certainly present in authigenic anatase (Fig. 4C, Supplementary Tab. 3). Since the maximum abundance of  $\Sigma$ REEs is found in the mud fraction (356.73 ppm, Tab. 3), REEs are more significantly associated with the Ti-bearing heavy minerals (rutile, anatase, brookite, ilmenite, titanite, and ilmenorutile,) than with zircon, euxenite and xenotime. It is already well known that the REEs substitute for Zr in the crystal structure of zircon (Romans *et al.*, 1975; Speer, 1980). On the other hand, although it is rarely reported that  $\text{TiO}_2$  correlates with REEs, the results confirm this correlation. For example, in recent stream sediments and floodplain sediments,  $\text{TiO}_2$  correlates fairly well with Eu ( $r > 0.6$ ), and weakly with most of the REEs ( $r > 0.4$ ; Anonymous, 2005).

From another aspect, the subarkosic arenite suites 1 and 3, derived directly from the Aqaba Complex granitoid source rocks, are characterized by higher  $\Sigma$ REEs,  $\Sigma$ LREEs, and  $\Sigma$ HREEs than the quartz arenites suite 4 that are recycled from older siliciclastic strata, and higher than the first-cycle quartz arenite suite 2 (Tab. 3) that was produced by intense, chemical weathering of the source rocks (to be discussed below). However, this REE enrichment is much more pronounced in the subarkosic arenite suite 3 than in the subarkosic arenite suite 1 (Tab. 3). The high HREEs can only be attributed to the presence of garnet in the former suite (Fig. 2G, Supplementary Tab. 3; Amireh, 1991, 2018, 2020), since the HREEs have radii small enough to substitute for  $\text{Al}^{3+}$  in the garnet crystal. The reason for garnet, which is unstable against chemical weathering, being only in this sandstone suite, is the absence of chemical weathering affecting the source rocks. This is attributed to the cold, arid climate,

prevailing in the study area during the Late Ordovician regional, glacial event (Abed *et al.*, 1993). On the other hand, the source rocks of subarkosic arenite suite 1 were subjected to intensive chemical weathering because of the prevailing hot, humid climate at the time of its derivation, as will be discussed below. Moreover, the higher  $\Sigma$ REEs and  $\Sigma$ LREEs in subarkosic arenite suite 3 could be attributed, additionally, to its higher content of detrital micas (particularly biotite, Fig. 2D), chlorite and rutile/anatase, and having a matrix rich with S/I-mixed layers.

### Eu anomaly

The negative correlation of the Eu negative anomaly ( $\text{Eu}/\text{Eu}^*$ ) with Zr ( $r = -0.5$  in all suites) and the absence of a correlation with  $\text{Al}_2\text{O}_3$  ( $r = 0.16$  in all suites) indicate that neither zircon nor the clay minerals are responsible for the Eu anomaly in the sandstone and mudstones investigated. Instead, it was inherited from their source rocks, the Aqaba Complex granitoids that exhibit similar  $\text{Eu}/\text{Eu}^*$  values (Jarrar *et al.*, 2003; Ben sera, 2018), closely resembling the UCC (White, 2013).

In the coarse, medium, fine, and very fine sand fractions, the Eu anomaly reaches values of 0.6, 0.67, 0.75, 0.64 (Tab. 3), respectively. Thus, there is no obvious correlation of the Eu anomaly with the sand grain size; in other words, hydraulic sorting had no effect on its value. Moreover, the value of the Eu negative anomaly of the average sand (0.68) is comparable with that of the UCC (0.65). Additionally, its value (Tab. 3) in the average mud (0.72) is also close to that of the PAAS (0.65), NASC (0.68) and Phanerozoic Shale (0.63).

However, subarkosic arenite suite 1, produced by intensive weathering of the source rocks, has a lower negative Eu anomaly value (0.73) than the subarkosic suite 3 (0.69), which must be due to weak degrees of weathering of the source rocks, apparently indicating that the anomaly decreases with chemical weathering. What is more remarkable is that the first-cycle quartz arenite suite 2 has a significant lower negative anomaly (0.7) than the recycled quartz arenite suite 4 (0.58), indicating that recycling significantly increases the value of the Eu negative anomaly.

Additionally, the subarkosic arenites have an  $\text{Eu}/\text{Eu}^*$  mean of 0.7, whereas that of the quartz arenites is 0.65, meaning that the latter has a larger Eu negative anomaly value than the former. This could be attributed to the presence of garnet in the subarkosic arenite suite 3 (Fig. 2G; Supplementary Tab. 3) that lowers the Eu negative anomaly. This is because  $\text{Eu}^{2+}$  can substitute for  $\text{Ca}^{2+}$  in Fe-rich garnet, thus  $\text{Eu}^{2+}$  is strongly partitioned into the garnet (Smith *et al.*, 2004). This conclusion is corroborated by the fairly good to weak correlation between the  $\text{Eu}/\text{Eu}^*$  and the modal amounts of garnet ( $r = 0.4$ , in all suites, and 0.41 in subarkosic arenite).

## DISCUSSION

It is obvious from the preceding text that the distribution of the TEs and REEs in the four sandstone suites and the mudstone suite was controlled by eight factors: the

provenance source rocks and tectonic setting, chemical weathering, recycling, hydraulic sorting, depositional environment, redox conditions, very low-grade metamorphism/low-temperature, hydrothermal metasomatism, and diagenesis, as discussed below.

## Provenance

### Source rocks

As mentioned in the introduction, the relatively immobile elements Al, Ti, Zr, Y, Hf, Ga, Th, Nb, and Sc, and the REEs, generally were transported from the source rocks within their containing minerals as a suspended load to the depositional sites with little chemical alteration. Under the assumption that they were quantitatively transported from the source rocks to the depositional site without any loss along the way (Ali *et al.*, 2014), these elements and their ratios can be used to trace the sediment provenance (Taylor and McLennan, 1985; Blake *et al.*, 2017). Table 4 lists the elements and elemental ratios, characteristic for standard felsic, mafic and recycled source rocks, the average UCC, and their values in the siliciclastics investigated.

The standard, felsic source rocks, employed in Table 4, are Proterozoic granite (Condie, 1993), the Rahma Suite and the Hummrat Feinan Suite of the Aqaba Complex (Jarrar *et al.*, 2003), and the Danburg granite (Cullers, 1988). The standard, mafic source rocks employed are average mid-oceanic ridge basalt (AMORB, White and Klein, 2013), late Proterozoic basalt (Condie, 1993), the Duheila hornblende Suite (Jarrar *et al.*, 2003), the Qunai monzogabbro (Ghanem and Jarrar, 2013), the Araba mafic to intermediate Suite of the Aqaba Complex (Jarrar *et al.*, 2003), and the ultramafic Wet Mts. amphibolite (Cullers, 1994).

A major, felsic source for the siliciclastics investigated is indicated by the following element abundance values and element ratios (Tab. 4): a high abundance of Ba, Rb, Zr, Hf, and Th, a low abundance of Ti, Sc, Cr, Ni, Zn, and Cu, high Th/Sc, Y/Ni, and Ba/Sr, and low Cr/Th, Ti/Zr, Ti/La $\times$ 20, and Ce/Th. On the other hand, only the high Cr/Ni indicates a rare, mafic provenance. Additionally, a minor, recycled siliciclastic provenance is indicated by the SiO<sub>2</sub> mean (89.19 wt.%) that mainly represents detrital quartz grains, being much higher than that of the felsic and mafic provenances (Tab. 4). It can be added here, that since quartz overgrowths have the same chemical composition as the detrital grains, entirely SiO<sub>2</sub>, as indicated by the optical continuity of the detrital quartz cores and the syntaxial quartz overgrowths (Fig. 2A), there could be no difference in TE and REE content of the quartz detrital grains and the quartz overgrowths. Moreover, insignificant amounts of TE and REE are hosted in the overgrowths, which do not exceed 14% modal composition, in comparison with the detrital quartz cores that attain modes of up to 92% (Supplementary Tab. 2). Accordingly, the claim that there could be a difference in the TE and REE content of detrital quartz grains and quartz overgrowths should not prevent the use of SiO<sub>2</sub> as a proxy for recycled siliciclastic provenance.

Therefore, the provenance of the lower Cambrian–Lower Cretaceous siliciclastic succession under study is a mixed

one, consisting of major, felsic; minor, siliciclastic; and rare, mafic source rocks.

The theoretical explanation for the abundances of these provenance-indicative elements and element ratios is as follows. Barium, Rb, Zr, Hf, and Th have higher abundances in felsic, compared to mafic rocks. Ba and Rb are attributed to high K-feldspar, Zr and Hf to high zircon, and Th to the higher monazite and apatite contents of the granitic, felsic provenance. On the other hand, Cr, Ni, Sc, Cu, Zn and Ti have higher abundances in mafic, compared to felsic source rocks. Cr and Sc are related to pyroxene, Ni to olivine, Zn to magnetite, Cu to pyroxene, hornblende and biotite, and Ti to high-Ti augite, amphibole, and biotite in mafic source rocks. Consequently, the felsic source rocks are characterized by high Ba/Sr, Th/Sc, and Y/Ni because Y substitutes for Zr in zircon, as indicated in the present study by the fairly good correlation between Y and Zr ( $r = 0.64$  in all suites and  $0.68$  in subarkosic arenite) and low Cr/Th, Ti/Zr, Ce/Th, and Ti/La $\times$ 20. The latter two lower ratios are interpreted as follows. Although the higher Ce content of felsic source rocks, relative to mafic ones, is attributed to the larger amounts of monazite, xenotime, apatite, and zircon, it seems that the much higher Th content of felsic, relative to mafic rocks, results in lower Ce/Th in the felsic rocks. The lower Ti/La $\times$ 20 in felsic source rocks is attributed to smaller amounts of Ti-bearing minerals and concomitantly higher La-bearing minerals, such as monazite, apatite, and K-feldspar in the felsic rocks. Only high Cr/Ni could indicate a mafic provenance, as this contains large amounts of Cr-bearing pyroxene and smaller amounts of Ni-bearing olivine.

From another perspective, the proposed, mixed provenance of the clastic sediments is substantiated by provenance discriminant plots Sc vs. Th (Fig. 11A), Cr/Th vs. Th/Sc (Fig. 11B), Zr/Sc vs. Th/Sc (Fig. 11C), and Th vs. La (Fig. 11D). All these diagrams show that most of the samples of the four sandstone suites plot within the field of felsic rocks, or close to it.

The data point to a major, felsic provenance that must have consisted of granitoids, mainly granites, and less commonly granodiorites, gneisses, and schists, of the Aqaba Complex of the late Neoproterozoic Arabian-Nubian Shield. On the other hand, the minor degree of recycled, siliciclastic provenance was due to the contributions from the lower Palaeozoic strata that supplied detritus to the middle and upper Palaeozoic deposits, and furthermore to contributions from the lower Mesozoic siliciclastic strata that all delivered detritus to the Lower Cretaceous Kurnub Group. Finally, the rare, mafic provenance can be attributed to the smaller volume of mafic rocks, available in the Arabian-Nubian Shield, such as the Duheila Hornblendite Suite (Jarrar *et al.*, 2003) and the Qunai monzogabbro (Ghanem and Jarrar, 2013) that contributed hornblende, ilmenite, ilmenorutile, rutile, and the opaque heavy minerals.

On the basis of a large, geochemical dataset, this study constrains the provenance of the clastic sediments to large, felsic; minor, clastic; and rare, mafic source rocks. The data strongly point to the Arabian Shield as the source of the siliciclastic sediments, as recorded by many studies, based on other lines of evidence, including sedimentological and petrographic criteria (Amireh 1991, 1997, 2018, 2000, 2020;

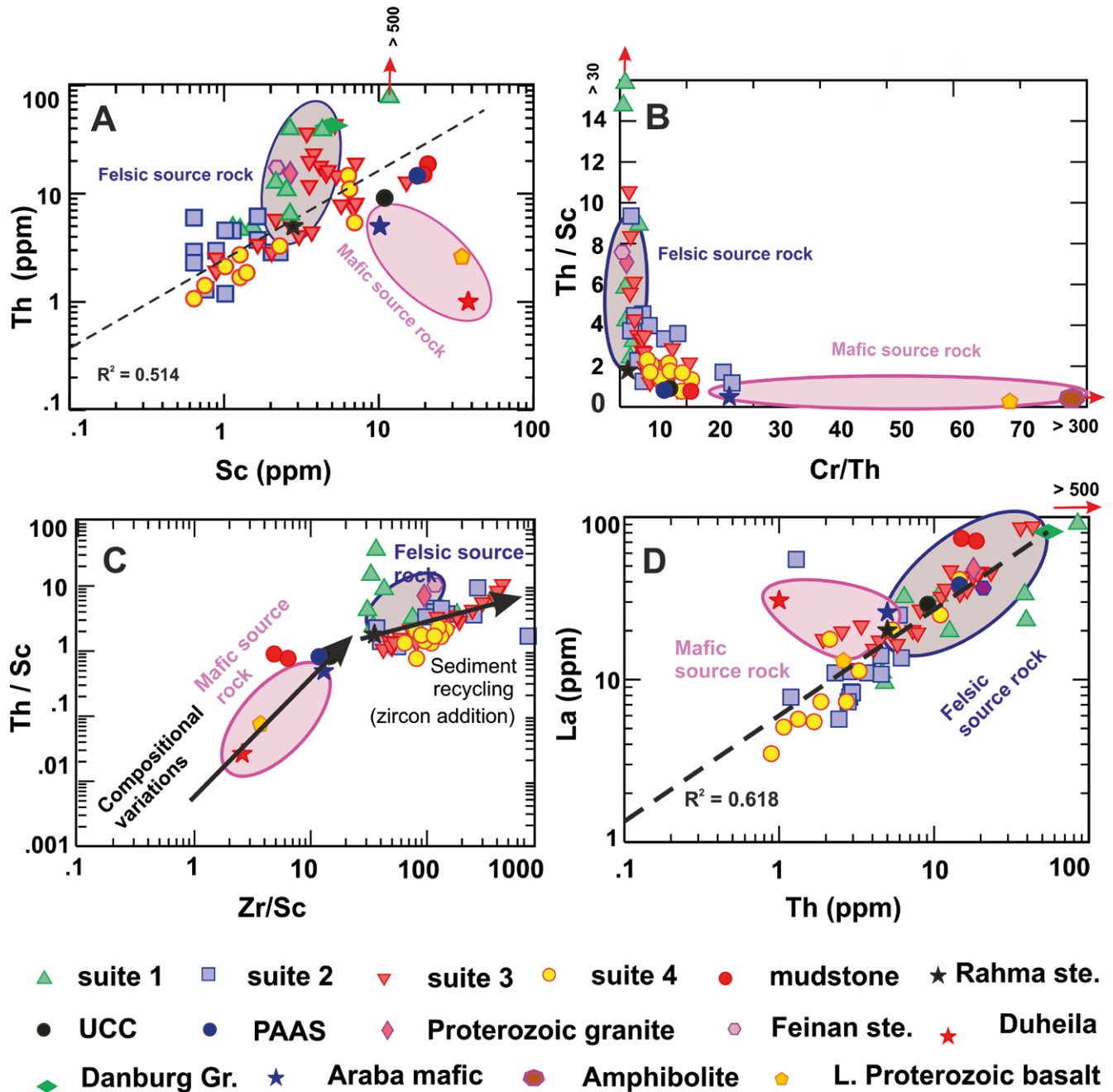


Fig. 11. Provenance discriminant bivariate plots.

Amireh *et al.*, 1994b, 2001, 2008, 2019; Schneider *et al.*, 2007).

Moreover, an Arabian-Nubian Shield provenance similarly was documented in nearby countries. West of the study area (Fig. 1), Weissbrod and Nachmias (1986), Kröner *et al.* (1990), Avigad *et al.* (2003, 2015, 2017), Kolodner *et al.* (2006), and Morag *et al.* (2012) similarly recorded this Neoproterozoic Arabian-Nubian Shield provenance for the Cambrian and Ordovician siliciclastic sequence. On the basis of a study of heavy minerals in the Early Cretaceous Kurnub Group, Weissbrod and Nachmias (1986) concluded that granitic and metamorphic rocks of the Arabian-Nubian Shield acted as their sources. Kröner *et al.* (1990) dated detrital zircon grains from several rock types of the Eilat basement (Fig. 1) and the adjacent Sinai, applying the  $^{207}\text{Pb}/^{206}\text{Pb}$

single-grain evaporation method, and obtained an age range of 820 to 800 Ma. Avigad *et al.* (2003) recorded 550–650 Ma ages of detrital zircons from the Cambrian unit in the Eilat area, using the SHRIMP U-Pb method (Fig. 1). They also indicate the calc-alkaline and alkaline, igneous rocks of the Neoproterozoic Arabian-Nubian Shield as the provenance. Avigad *et al.* (2015), on the basis of U-Pb-Hf detrital zircon geochronology of the Zenifim Formation, subcropping west of the study area (Fig. 1), identified the granites of the adjacent Arabian-Nubian Shield, formed at the cessation of the Neoproterozoic orogeny, as a major provenance for these late Ediacaran arkoses.

Recently, Avigad *et al.* (2017) used detrital rutile U-Pb geochronology to deduce a broad North African source for the Cambro-Ordovician sandstones, cropping out in the Eilat

area (Fig. 1), southern Jordan, and Ethiopia. Kolodner *et al.* (2006) obtained 900–530 Ma U-Pb ages, indicating derivation of the Cambrian and Ordovician siliciclastics from the proximal, northern part of the Arabian-Nubian Shield. Kolodner *et al.* (2009) also obtained U-Pb ages for detrital zircons from Lower Cretaceous sandstones, cropping out west of the study area, and concluded that they are mostly derived from reworking of the Palaeozoic section. Morag *et al.* (2012) documented the northern Arabian-Nubian Shield as a provenance for the Eilat conglomerate (Fig. 1) unit, based on detrital zircon grains, ranging in age from 1.0 Ga to around 580 Ma. More westward, Samuel *et al.* (2011) constrained the age of the Rutig conglomerate between 850 and 600 Ma, concluded the provenance to be the Arabian-Nubian Shield material in Sinai, and confined deposition of different levels of the conglomerates to ca 620–610 Ma and 600–590 Ma.

It should be emphasized that, since the signature of this mixed provenance is still recognizable in the major, TE and REE compositions of the sandstones and mudstones, even after being variably influenced by other factors, it can be concluded that provenance was the principal factor, controlling the chemical composition of the sandstones and mudstones under investigation.

### **Tectonic setting**

Using the La-Th-Sc diagram, the tectonic setting of the sandstone provenance may be inferred (Fig. 12A). Most samples of sandstone suites 1, 2, 3, and 4 fall in the passive (D) and active, continental margin (C) and a few samples fall in the oceanic island-arc field (B). This generally agrees with the transitional (TC) and craton interior (CI) continental block provenances for the same subarkosic arenite suites 1 and 3 (Fig. 12D), whereas quartz arenite suites 2 and 4 fall entirely in the craton interior (CI) continental block provenance field (Fig. 12D). The same result is obtained, using the Th-Sc-Zr/10 ternary diagram (Fig. 12B), where most samples of the sandstone suites 2, 3, and 4 fall in the passive continental margin field. Furthermore, the V-Ni-Th $\times$ 10 diagram (Fig. 12C) likewise shows that the four sandstone suites either fall within, or cluster around the felsic source rocks field. On the other hand, the majority of the subarkosic arenite suite 1 samples plot outside this and all the other fields, owing to the rather high content of Th in the samples, located directly above the Rum Unconformity that were affected by a hydrothermal metasomatism event.

Additionally, it is implicitly assumed in this study that the plots of Pearce *et al.* (1984) for igneous rocks can be applied to siliciclastic, sedimentary rocks, since the provenance was mainly of granitic composition as shown above; the consistency of the results justify this assumption. Accordingly, the tectonic setting of the provenance areas could be constrained by constructing various bivariate trace-element plots, including Y vs. Nb (Fig. 13A), Yb vs. Ta, (Fig. 13B), (Y + Nb) vs. Rb (Fig. 13C), and (Yb + Ta) vs. Rb (Fig. 13D).

The Yb vs. Ta plot (Fig. 13B) indicates that most samples of the four sandstone suites and the mudstone samples are constrained in the volcanic arc granite field (VAG), with a few sandstone samples plotting in the within plate granite (WPG), syn-collision granite (syn-COLG) or orogenic

granite (ORG) fields. The same result is obtained by the Y vs. Nb (Fig. 13A), (Y + Nb) vs. Rb (Fig. 13C), and the (Yb + Ta) vs. Rb plots (Fig. 13D). This inferred volcanic-arc tectonic setting of the granitic source rocks provenance of the sandstones and mudstones agrees with the collisional and accretionary, tectonic processes that led to the formation of the Arabian-Nubian Shield (Abdelsalam and Stern, 1996; Hussein, 2000; Al Shanti, 2009). This shield formed during the late Neoproterozoic amalgamation of northern Gondwana, the so-called Pan African thermo-tectonic event (Kröner, 1984). Moreover, this inferred provenance volcanic-arc tectonic setting was documented recently by Ben sera (2018) for most of the granitic suites of the Aqaba Complex granitoids in Jordan.

The volcanic arcs granites were involved during the cratonization phase of accretionary and collisional (compressional) tectonic processes and the complete assembly of the Arabian Shield (Al Shanti, 2009). Subsequently, at the end of the late Neoproterozoic, an extensional collapse phase of the Pan African thermo-tectonic event occurred in the Arabian Shield and replaced the compressional phase. In this last extensional phase, rifting led to the development of the regionally extensive Najd Fault System and its complementary syn-rift, down block-faulted, extensional basins and up block-faulted heights (Amireh, 2018) that could be considered as a passive continental margin tectonic setting. This passive continental margin terrane consisting of Aqaba Complex granitoids, of volcanic arc origin, represents the major source rocks provenance of the sandstones and mudstones that persisted during deposition of the entire lower Cambrian-Lower Cretaceous succession.

### **Chemical weathering and recycling**

The chemical weathering of source rocks is controlled by the prevailing climate and the properties of the source rocks. Chemical weathering can be estimated by the index of chemical alteration (CIA; Nesbitt and Young, 1982, 1984), where high values indicate a high intensity of chemical weathering. According to the CIA of the sandstone suites and the mudstone suite investigated (Supplementary Tab. 1), the order of increasing weathering intensity of their source rocks is subarkosic arenite suite 3 (CIA = 63), subarkosic arenite suite 1 (CIA = 70), quartz arenite suite 2 (CIA = 75), and finally quartz arenite suite 4 (CIA = 90).

The lowest CIA for the subarkosic arenite suite 3 (CIA = 63) is attributed to the high, modal amounts of K-feldspar in the samples (Supplementary Tab. 1) that were not leached or hydrolyzed, owing to the absence of chemical weathering during the Late Ordovician glacial event at the time of deposition of this suite (Abed *et al.*, 1993). On the other hand, the higher CIA of both subarkosic arenite suite 1 and quartz arenite suite 2, and quartz arenite suite 4, are due to the hot, humid climate, prevailing in the early Cambrian to Middle Ordovician (Amireh, 1991, 2018; Sandler *et al.*, 2012; Amireh *et al.*, 2019) and the Early Cretaceous (Amireh, 2018), respectively. These inferences of the intensity of chemical weathering of the source rocks of the various sandstone suites, based on the CIA weathering index, is substantiated by further geochemical attributes, particularly, REE and TE depletion, as discussed below.

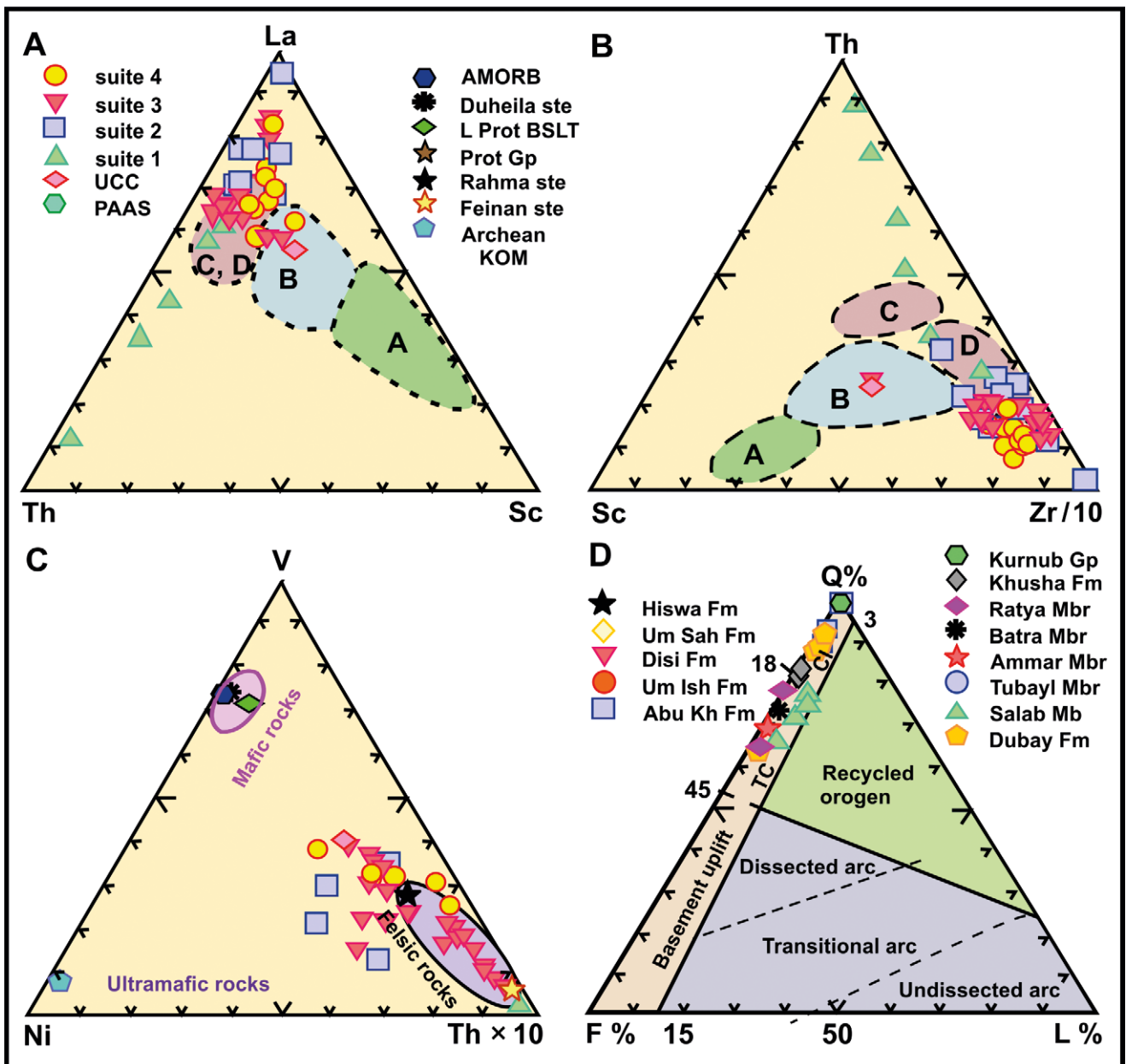


**Fig. 12.** Triangular diagrams illustrating: **A.** Provenance tectonic setting discriminate La-Th-Sc ternary plot with fields of passive continental margin (D), active continental margin (C), continental island arc (B), and oceanic island arc (A) after Bhatia and Crook (1986). **B.** Provenance tectonic setting discriminate Th-Sc-Zr/10 ternary plot, fields as those in A. **C.** Felsic-mafic-ultramafic discriminate V-Ni-Th $\times$ 10 ternary plot; fields of felsic and mafic rocks are established in this study. **D.** Tectonic setting discriminate Q-F-L (quartz-feldspar-lithic fragments) ternary diagram after Dickinson *et al.* (1983). Note that the formations of suites 2 and 4 fall entirely in the continental interior discriminate field (CI), whereas the formations of suites 1 and 3 fall between the CI and the transitional continental block discriminate field (TC).

It can be added here that among the weathering products of the granitoid source rocks is kaolinite. It was detached from the weathering profile, accumulating on the source rocks, as detrital kaolinite. Afterwards, it was transported by braided rivers, and finally deposited mainly on braid plains or bar tops as a detrital matrix, interspersed between detrital framework grains. During diagenesis, part of this detrital kaolinite was recrystallized into crystalline kaolinite, in addition to the directly precipitated kaolinite in the interstitial pore spaces between the framework grains (authigenic kaolinite).

Quartz arenite suite 4 was subjected to pronounced recycling more than the other sandstone suites. This conclusion was previously proposed, on the basis of several petrographic criteria (Amireh, 1991, 2018) and here is confirmed by geochemical attributes, particularly, its REE and TE depletion.

#### TEs and REEs depletion

Subarkosic arenite suite 1, produced by intensive weathering of the source rocks, has lower concentrations of all the REEs,  $\Sigma$ REEs,  $\Sigma$ LREEs,  $\Sigma$ HREEs, and TEs, Zr, Hf, Ba, Cr,

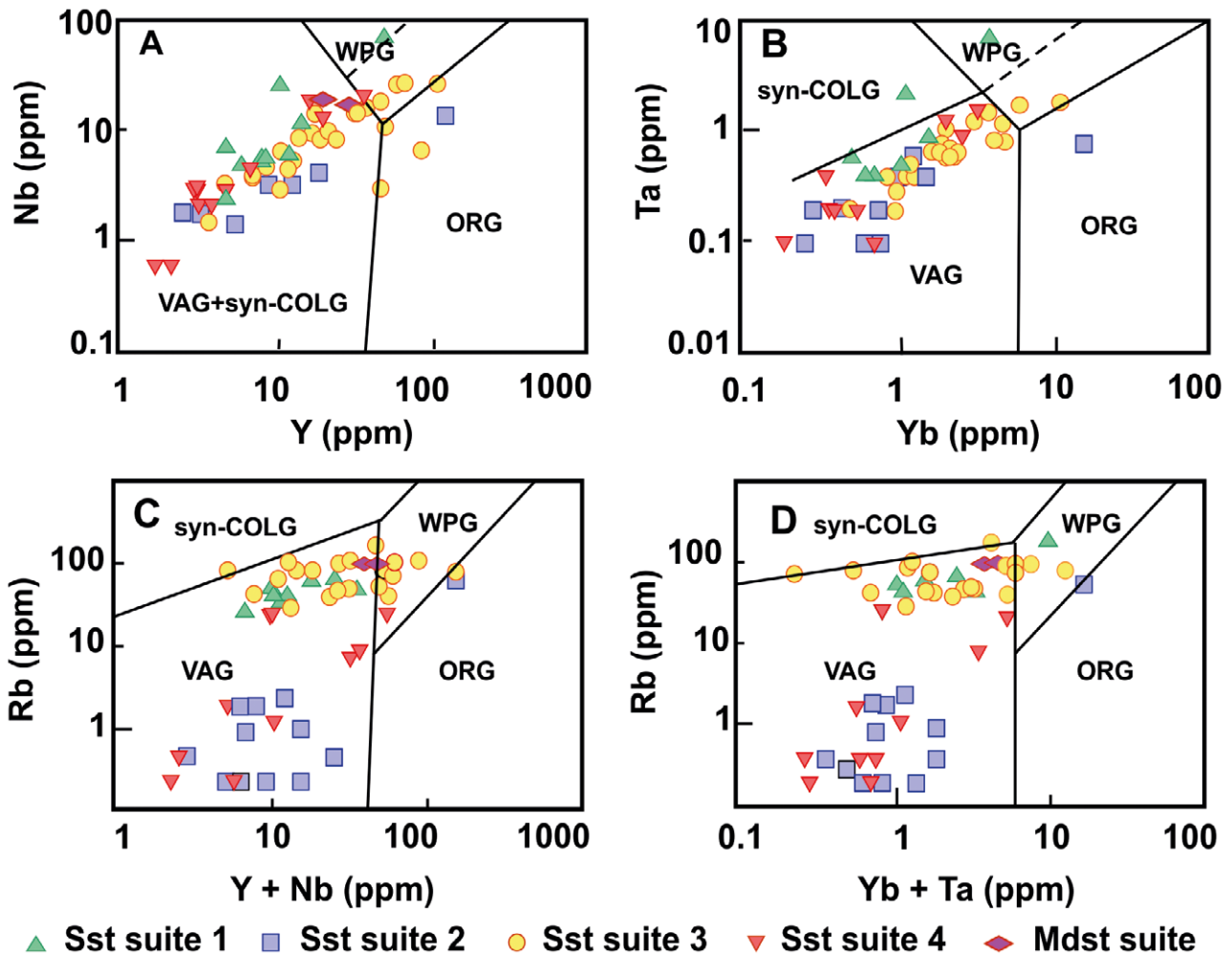


**Fig. 13.** Granitic source rocks tectonic setting bivariate discriminate plots. **A.** Y vs. Nb. **B.** Yb vs. Ta. **C.** (Y + Nb) vs. Rb. **D.** (Yb + Ta) vs. Rb after Pearce *et al.* (1984). VAG – volcanic arc granite, syn-COLG – syn-collisional granite, WPG – within plate granite, PRG – orogenic granite.

Cs, Ga, Rb, Sc, Sr, V, Y, and Zn, compared to subarkosic arenite suite 3, that resulted from a much lower degrees of source rock weathering (Tabs 2, 3). This indicates that depletions of these elements were due to an intensive, chemical weathering event. The authors therefore conclude that chemical weathering of the sandstone provenance caused depletion of all the REEs, and the TEs, Zr, Hf, Ba, Cr, Cs, Ga, Rb, Sc, Sr, V, Y, and Zn. However, the effects of subsequent recycling and hydraulic sorting partly may have counteracted this result, as will be shown next.

The highly recycled quartz arenite suite 4 has lower concentrations of REEs,  $\Sigma$ REEs,  $\Sigma$ LREEs,  $\Sigma$ HREEs, and Cu, Ga, Pb, Sn, Sr, W, Y and Zn than the first-cycle quartz arenite suite 2 and the other subarkosic arenite suites. The depletion of the TEs and the REEs, due to recycling, could be attributed to the initial reworking and winnowing of the low-density clay minerals containing these TEs and part of the REEs. However, assuming that the clay minerals stayed in a closed system, they were subsequently once more concentrated by the counteracting process of hydraulic sorting. On the other hand, the highly recycled quartz arenite suite 4

was enriched in Zr, Hf, Ba, Co, Cr, Cs, Nb, Ni, Rb, Ta, Sc, Th, U, and V to higher degrees than the first-cycle quartz arenite suite 2. The concentration of zircon during recycling is confirmed by the Zr/Sc vs. Th/Sc plot (Fig. 7C), which shows that the Zr/Sc in the four sandstone suites deviates from its compositional variation from mafic to felsic rocks, which may be attributed to zircon addition and concentration during recycling (McLennan *et al.*, 1993).

Therefore, it can be concluded that recycling caused depletion of REEs and Cu, Ga, Pb, Sn, Sr, W, Y and Zn, but enrichment in Zr, Hf, Ba, Co, Cr, Cs, Nb, Ni, Rb, Ta, Sc, Th, U, and V. This apparent contradiction between the depletion of REEs and some TEs and enrichment of Zr, Hf and other TEs during recycling may be attributed to the accommodation of LREEs, HREEs and some TEs in other heavy minerals, which have lower, mechanical durability than zircon and thus lower resistance against recycling. Such heavy minerals include rutile/anatase, monazite, apatite, thorite, titanite, and xenotime that were abraded, or even removed during recycling (Amireh, 1991). However, these heavy minerals may be concentrated in specific grain

size fractions by subsequent hydraulic sorting, as is shown in the next section.

From another point of view, the REEs,  $\Sigma$ REEs,  $\Sigma$ LREEs, and  $\Sigma$ HREEs of each average sand size fraction are below that of UCC (Tab. 3). This may indicate REE fractionation, becoming depleted in the average sand fraction relative to the average UCC, owing to intensive chemical weathering or recycling. However, this conclusion would be misleading, since the very fine sand size fraction is actually more enriched in REEs than UCC, owing to zircon hydraulic sorting, whereas the coarser sand size fractions (fine, medium, and coarse sand) are virtually depleted in REEs, relative to UCC (Tab. 3). This REE depletion may be attributed to their derivation from the upper part of weathering profiles, depleted in REEs, not from the deeper REE-richer part (Nesbitt and Markovics, 1997). This reflects intensive, chemical weathering of the source rocks with high REE contents (average of Feinan and Rahma Suites of the Aqaba Complex, Tab. 3), characterized by low relief, and exposed in the transitional and stable interior of the Arabian Craton (Fig. 2F; Amireh, 2018). Additionally, this REE depletion in the coarse to fine sand-sized quartz arenite suites may reflect their being recycled from older, siliciclastic Palaeozoic and/or Mesozoic strata, originally depleted in REEs.

It should be added that the various degrees of recycling of the four sandstone suites have been substantiated by numerous, petrographic observations. One criterion is the high degree of roundness and abrasion of the ultrastable heavy minerals zircon, rutile, and tourmaline (Fig. 3B), i.e., very stable minerals, resisting mechanical abrasion. A second criterion is the presence of two-quartz overgrowth envelopes, surrounding detrital quartz cores (Amireh, 1991, 2018), indicating two cycles of sedimentation. A third criterion is the well-rounded and well-sorted character of the detrital quartz grains (Fig. 2A; Amireh, 2015; Saffarini and Amireh, 2016). On the other hand, first-cycle quartz arenite suite 2 lacks such well-rounded, ultrastable, heavy minerals and quartz grains, but on the contrary, consists mainly of angular to sub-rounded heavy minerals (Fig. 3A) and quartz grains (Fig. 2C). Moreover, the overgrown quartz grains exhibit only one envelope around a detrital quartz core (Fig. 2A).

According to these unequivocal, petrographic criteria, the claim that the quartz arenite suite 4 may have originated by diagenetic removal of non-quartz minerals, as in the case recorded by McBride (1987), is refuted.

### **Hydraulic sorting**

Hydraulic sorting of detrital minerals, according to their size and density, during transport and deposition may lead to their fractionation into different grain sizes. Therefore, selective enrichment of some elements is associated with the clay minerals (Riboulleau *et al.*, 2014), and other elements are associated with heavy minerals in the fine sand, very fine sand, or the silt size fractions. On the other hand, Si is fractionated in the medium to coarse sand fractions, owing to the hydraulic sorting of detrital quartz in these grain sizes.

Upon decreasing grain size from coarse sand (represented by sample US1 not affected by hydrothermal metasomatism) to mud fraction, only SiO<sub>2</sub> decreases, whereas Al, Fe, Mg, and Ti oxides and LOIs increase in abundance

(Supplementary Tab. 1). This trend is straight-forwardly attributed to decreasing detrital quartz content and the concomitant increase in detrital clay minerals, due to hydraulic sorting. Similarly, there is a systematic increase in the abundance of most of the TEs and REEs (Tabs 2, 3). Accordingly, the mudstones are enriched in Co, Cr, Cs, Cu, Ga, Ni, Pb, Rb, Sc, Sn, Sr, Th, U, V, W and Zn, and selected REEs (La, Ce, Pr, Nd, Sm, Eu, Gd and Tb), all associated with detrital and authigenic clay minerals. Additionally, the silt-size fraction of the mud is enriched significantly in Ti, Nb, Ta, and the REEs, which are associated with rutile, anatase, brookite, ilmenite, titanite, and ilmenorutile, as shown in the section on the abundance and distribution of the REEs. Moreover, the very fine sand fraction is enriched in Zr, Hf, Y, Ba, Dy, Ho, Er, Tm, Yb, and Lu; whereby Zr and Hf are contained solely in zircon, whereas Y, Dy, Ho, Er, Tm, Yb, and Lu are hosted largely in zircon, and partly in the other heavy minerals.

### **Very low-grade metamorphism and low-temperature, hydrothermal metasomatism**

Amireh (2020) recorded a very low-grade metamorphism and associated low-temperature, hydrothermal metasomatism in the lower part of the siliciclastic succession, using several petrographic criteria. This result is confirmed here for the coarse sandstones, directly overlying the Rum Unconformity (particularly sample SR1, Tabs 2, 3) by their anomalous, high concentrations of TEs and REEs, compared to UCC and the average composition of the Aqaba Complex granitoid source rocks (Tabs 2, 3). The enriched TEs include Ag, Co, Ga, Hf, Nb, Rb, Sc, Sn, Ta, Tl, Th, U, V, W, Y, and Zr. The enrichment of these TEs and REEs is attributed to the neof ormation of the following, opaque heavy minerals: thorite, ilmenorutile, xenotime, euxenite, cassiterite, and scheelite, as discussed in the sections on distribution of TEs and other elements. This interpretation is substantiated by the strong, positive correlations of these elements with the modal amounts of opaque, heavy minerals (Supplementary Tabs 4, 5). Moreover, Ti is enriched and resides partly in neof ormed anatase, encountered in the sandstones, overlying the Rum unconformity. Silver and Tl are incorporated in other unidentified minerals. On the other hand, the enrichment of the other TEs and REEs is attributed to illite neof ormation (Figs 2B, 3D), particularly Rb, Cr, Ni, V, Zr, Sc, and Ga, as discussed in the sections on distribution of lithophiles and TEs. Similarly, this interpretation is substantiated by the strong, positive correlation of these elements with the proxy for neof ormed illite, Al and K (Supplementary Tabs 4, 5). The REEs, besides being associated partly with neof ormed xenotime and euxenite, are also accommodated partly in neof ormed anatase. Amireh (2020) recorded that the TEs and REEs, required for neof ormation of the various minerals, mentioned above, were supplied by the hydrothermal fluids, flowing through the impermeable Cambrian-Silurian sandstones and leaching elements from the clayey, iron-oxide-rich matrix, and possibly dissolving portions of the unstable feldspars, and some of the heavy minerals, particularly tourmaline (Amireh, 2020, fig. 5F). Moreover, Amireh (2020) proposed that this low-temperature, hydrothermal event

took place during the Middle/Late Devonian, or middle Carboniferous, or during three other geologic times.

Additionally, the Eu/Eu\* anomaly attains a value of 0.48 in sample SR1, indicating a much larger Eu negative anomaly than for the average UCC (0.65) and average sandstone (0.68). This might lead to the conclusion that hydrothermal metasomatism caused the increase of the negative value of the Eu anomaly.

Moreover, low-temperature, hydrothermal metasomatism is further confirmed by unraveling the geochemical attributes of monazite alteration to thorite. Alteration of detrital monazite to thorite was observed in sample SR1 (Fig. 2E); besides an anomalously high abundance of REEs (Tab. 3), it is characterized by an unusually high concentration of Th and U (504 ppm, 32 ppm, respectively, Tab. 2).

It is to be emphasized that low-temperature, hydrothermal metasomatism overprinted the effects of the provenance source rocks, chemical weathering and recycling, and hydraulic sorting, as discussed next. A metasomatic overprint of the provenance signature is indicated by the fact that the concentrations of some of the major elements, Al, K, Ti and Mn (Supplementary Tab. 1), and most of the TEs and REEs in the coarse sandstone, directly overlying the Rum Unconformity, are higher than those of the possible granitoid source rocks of the Aqaba Complex (Tabs 2, 3). Additionally, this coarse sandstone exhibits a remarkable enrichment of all the TEs and REEs, compared to the subarkosic arenite suite 1 that was produced by the intensive weathering of its source rocks (Tabs 2, 3). Moreover, it is enriched in all REEs and most TEs, compared to the quartz arenite suite 4 that was subjected to maximum recycling (Tabs 2, 3). Consequently, one may conclude that the low-temperature, hydrothermal metasomatism totally overwhelmed the chemical weathering effects and generally the recycling effects, as well. Additionally, this coarse sandstone deviates from the variation trends between the TEs, REEs and decreasing grain size of other samples (Tabs 2, 3). Therefore, it is appropriate to conclude, that the low-temperature, hydrothermal metasomatism strongly overprinted and erased the effect of hydraulic sorting.

### Depositional environment and redox conditions

Depositional environments of the four sandstone suites and the mudstone suite were predominantly fluvial and shallow-marine and are summarized in Table 1. The depositional environment of sandstone suite 1 is mainly a braided river (Amireh *et al.*, 1994a). Only three samples (AK2, AK6, and AK11) were deposited in a shallow-marine environment. Sandstone suite 2 was deposited dominantly in a braided-river environment. The depositional environment of sandstone suite 3 was entirely shallow-marine. Excluding three samples of sandstone suite 4 (J25, BF1, and BF10S), it was deposited by a meandering river of low sinuosity (Amireh, 1997). The mudstones generally were deposited on floodplains, or on bar tops within the braided river. Only samples H1 and BT6 were deposited in a shallow-marine environment.

The redox conditions predominant in the depositional environments of sandstone suites 1, 2, and 4 were straightforwardly oxic, since atmospheric oxygen was in direct contact

with the flowing water of the stream. Thus, sediments accumulating on the channel bottom, above bars, and on banks or floodplains, received oxygen during sedimentation and early diagenesis. On the other hand, the marine, depositional environment of sandstone suite 3 and a few samples from sandstone suites 1 and 4, could have been either oxic or anoxic.

To determine the redox conditions, predominant in the marine depositional environment, the following redox proxies are used: Ce/Ce\*, Pr/Pr\*, Ni/Co, V/(V + Ni), V/Cr, Mn\*, and U/Th (Supplementary Tab. 6). The former two ratios were calculated as the following:

$$\text{Ce/Ce}^* = \text{Ce}_{\text{SN}} / (0.5\text{La}_{\text{SN}} + 0.5\text{Pr}_{\text{SN}}),$$

$$\text{Pr/Pr}^* = \text{Pr}_{\text{SN}} / (0.5\text{Ce}_{\text{SN}} + 0.5)$$

following Bau and Dulski, (1996).

The Ce anomaly can be used to distinguish oxic vs. anoxic conditions of sedimentation. According to this formula, the smaller the resultant number, the more negative is the Ce anomaly. In oxidized seawater, cerium is oxidized from the soluble Ce<sup>3+</sup> to the highly insoluble Ce<sup>4+</sup>, which is removed from seawater and consequently creates a negative Ce abundance in seawater and the sediments derived from it, such as carbonate fluorapatite (CFA), glauconite, opal (Dumoulin *et al.*, 2011), and probably in fine siliciclastics, deposited at the bottom/water interface, such as sandstone suite 3, as discussed below. The removed Ce<sup>4+</sup> is, most probably, adsorbed on oxyhydroxides of Mn and Fe of the oceans, which may explain the positive Ce anomaly in, for example, Mn nodules on the ocean floor (e.g., Elderfield and Greaves, 1982; Wright *et al.*, 1987).

The Ce anomaly is around 1 (Supplementary Tab. 6), which is neither positive nor negative for the four sandstone suites, irrespective of their mineral composition, whether subarkosic or quartz arenites, or their depositional environment, whether fluvial or shallow-marine. Thus, the Ce anomaly has no significance in indicating the oxic vs. anoxic conditions of sedimentation of the four sandstone suites and the mudstone suite.

Moreover, this result is corroborated by plotting Ce/Ce\* vs. Pr/Pr\* using the diagram of Bau and Dulski (1996; Fig. 14). It can be seen from this figure that most samples of the four sandstone suites fall in field I, indicating neither a positive nor a negative Ce<sub>SN</sub> anomaly. Only a few samples fall in field IIa, and 10 samples in IIIb, indicating no negative, and a real negative Ce<sub>SN</sub> anomaly, respectively. The ten samples, indicating oxic conditions of the depositional environment, are mainly fluvial sandstone suites 1 and 4. This is a normal result for fluvial sediments, as discussed above.

Additionally, other element ratios are proposed as proxies for the palaeoredox of the siliciclastic, depositional environment. These are N/Co, V/(V+Ni), V/Cr, and U/Th.

The Ni/Co varies from 0 to 10 in all suites. However, in most samples of fluvial suites 1, 2, and 4 it has a zero value, whereas in samples of the marine sandstone suite 3, it ranges from 2.62 to 6.88, with an average of 3.86 and a standard deviation of 2.49. According to the results recorded by Jones and Manning (1994), if Ni/Co is less than 5, it indicates oxic, from 5 to 7 dysoxic, and greater than 7 dysoxic to suboxic-anoxic, depositional conditions. Therefore, the values of Ni/Co greater than 7 should be discarded for the samples

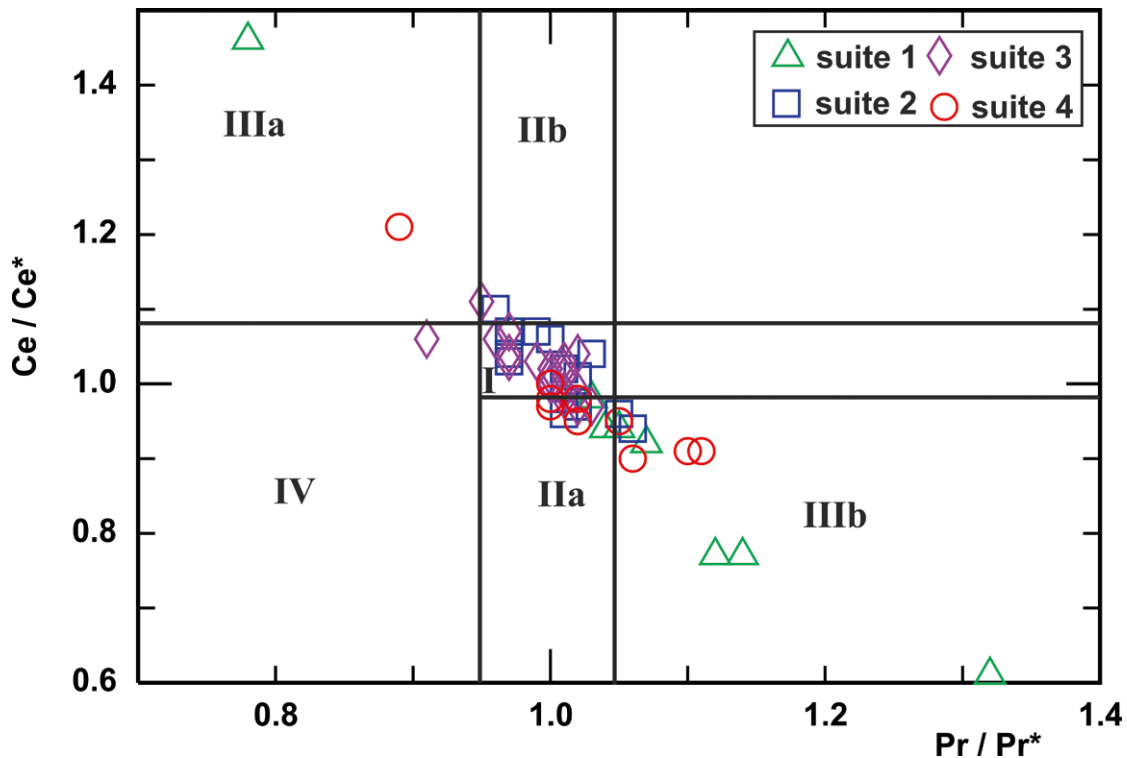


**Fig. 14.** Plot of  $Ce/Ce^*$  vs.  $Pr/Pr^*$  (Bau and Dulski, 1996), tests the effect of the concentration of  $La_{SN}$  on  $Ce_{SN}$  anomaly. Field I neither  $Ce_{SN}$  nor  $La_{SN}$  anomaly, field IIa positive  $La_{SN}$  anomaly that causes an apparent negative  $Ce_{SN}$  anomaly, field IIb negative  $La_{SN}$  anomaly that causes an apparent positive  $Ce_{SN}$  anomaly, field IIIa real positive  $Ce_{SN}$  anomaly, field IIIb real negative  $Ce_{SN}$  anomaly, and field IV positive  $La_{SN}$  anomaly that disguises positive  $Ce_{SN}$  anomaly.

(SR10, UI17, US1, and K1) that were deposited by a braided river, where oxic conditions predominated. However, the Ni/Co range and mean in the marine sandstones of suite 3 may indicate an anoxic, depositional environment.

The  $V/(V+Ni)$  proxy ranges from zero to 1 in the fluvial sandstone samples, from 0.37 to 0.79 in the marine sandstones, and from 0.59 to 0.94 in the mudstones. Following Pi *et al.* (2014), this indicates a strong reducing depositional environment for most fluvial sandstone samples, which is not the case. Regarding the marine sandstones, most of them were deposited under oxic conditions, excluding two samples, BF1, and BF10S. The mudstones, on the other hand, were mainly deposited in a reducing, depositional environment. This is again questionable, since their colour is neither black nor dark gray, indicating no organic carbon content, and pyrite is neither seen in thin sections, nor proved by XRD. Therefore, anoxic, depositional conditions can be refuted (Tucker, 2001). On the other hand, their colour is reddish or yellowish, owing to the presence of hematite, indicating oxic conditions, similar to many continental red beds, such as the Jurassic Navajo Sandstone, in Utah, USA.

The  $V/Cr$  ranges from 0.25 to 2 in the fluvial sandstones (excluding sample SR1 that was affected by the hydrothermal metasomatism), from 0.35 to 1.45 in the marine sandstones, and from 0.69 to 1.17 in the mudstones. According to Jones and Manning (1994), the values of  $V/Cr$  above 2 indicate anoxic, depositional conditions with  $H_2S$  present in water above the sediment, and below 2 indicate more oxidizing conditions. Values around 1 indicate that the  $O_2/H_2S$  interface was within the sediment. Accordingly, all

the fluvial and marine sandstone suites, and the mudstones were deposited in an oxic, depositional environment.

The U/Th proxy ranges from 0.02 to 0.59 in fluvial sandstones, from 0.19 to 0.53 in marine sandstones, and from 0.23 to 0.37 in mudstones. According to Jones and Manning (1994), U/Th values  $<0.75$  show oxic conditions, from 0.75 to 1.25 dysoxic, and  $>1.25$  suboxic. Therefore, the fluvial and the marine sandstones as well as the mudstones were deposited in an oxic environment.

Accordingly, it can be indicated by the previous four elemental ratio proxies and partly by the Ce anomaly that the depositional environment of the marine sandstone suite 3, as well as the fluvial sandstone suites 1, 2, and 4, and the mudstone suite was an oxic one. This oxidized, depositional environment, as well as oxic conditions of the early diagenetic environment, can explain the high, modal amounts of hematite cement in most samples of the four sandstone suites (Supplementary Tab. 2), as will be seen next.

### Diagenesis

The diagenetic processes encountered have the following paragenetic order: mechanical compaction and associated/consequent quartz pressure solution, syntaxial quartz overgrowth (Fig. 2A), epitaxial feldspar overgrowth, detrital feldspar dissolution, alteration and replacement, illitization and illite neoformation (Figs 2B, 3D), smectite and smectite/illite neoformation, kaolinite-dickite neoformation (Fig. 3C), calcite and dolomite cementation, titaniferous minerals authigenesis, particularly anatase (Fig. 4C), biotite

alteration and oxidation, iron oxides cementation (Fig. 4F), apatite overgrowth and neof ormation (Fig. 3F), poikilotopic or patchy barite cementation (Fig. 4B), and zeolite neof ormation (Fig. 3E). All these major diagenetic processes were recorded by the main author (Amireh, 1987, 1991, 1992, 2020; Amireh *et al.*, 1994b) and they will not be discussed further here.

Of particular interest are apatite overgrowth and neof ormation, anatase neof ormation, and iron oxide cementation, since these diagenetic processes are considered as sinks for TEs and REEs. It is to be emphasized that the present whole-rock geochemistry cannot enable us to determine the TEs and the REEs that were captured by these minor, authigenic minerals during diagenesis, since no single grain/crystal chemistry, excluding the semi-quantitative EDAX analysis, was carried out. To determine the elemental composition of the authigenic, single mineral grains or crystals a new study, employing other techniques and equipment, should be carried out. However, the following section represents an attempt to determine the TEs and REEs that were captured by these authigenic minerals during diagenesis, employing the present whole-rock chemistry and the data, available in the literature from other similar cases.

The authigenic apatite has the forms of euhedral overgrowth on abraded, detrital apatite grains (Amireh, 1991, 2018, 2020, fig. 3D) and discrete, euhedral, hexagonal apatite crystals (Fig. 3F). It is encountered only in some samples of sandstone suite 2 of Cambrian age (Supplementary Tab. 3). The overgrowth is probably francolite (carbonate-fluor-apatite), as documented by Bouch *et al.* (1995, 2002) and Rasmussen (1996). Moreover, it could be richer in the REEs (up to 1 wt.% Ce<sub>2</sub>O<sub>3</sub>), Sr and F than the detrital cores (O'Sullivan *et al.*, 2020), and possibly U, like that recorded in the equivalent rocks, west of the study area (Vermeesch *et al.*, 2009). Phosphorus shows no significant correlation with any TE or REE, or even any major element, thus, it was not possible to judge which of these elements were captured by the authigenic apatite overgrowths or the discrete hexagonal crystals. However, P was liberated probably from dissolved REE- and actinide-bearing phases in detritus (Bouch *et al.*, 2002), such as garnet (Fig. 2G), titanite (Amireh, 2020, fig. 2G), allanite and epidote, which were unstable during the low-temperature, thermal event, or even during burial diagenesis (Morton and Hallsworth, 1999 and references therein), and from the P, adsorbed onto clay-mineral surfaces (O'Sullivan *et al.*, 2020). The same can be applied on the other TEs and REEs that might be captured by the apatite overgrowths and the discrete, hexagonal apatite crystals.

Authigenic anatase occurs as discrete, euhedral crystals (Fig. 4C), with a characteristic anomalous, blue, first-order interference colour, thus it can be easily distinguished from detrital anatase (Fig. 4D), and detrital rutile (Fig. 3B) and detrital brookite. It is encountered in many samples of the four sandstone suites, particularly in marine, subarkosic arenite suite 3 (Supplementary Tab. 3).

Titanium correlates positively with Cr, Hf, Nb, Ni, Sc, Ta, U, V, Y, Zr, and REEs. Upon taking the samples D5A, RS3 and KH4 that contain much more modal anatase than detrital rutile and anatase (Supplementary Tab. 3), the following TEs are enriched therein: Cr, Hf, Nb, Sc, Ta, U, V, Y, and

Zr. On the other hand, REEs are enriched in these samples (Supplementary Tab. 3). How to distinguish between the TEs and REEs that are hosted in detrital rutile, anatase, titanite, ilmenite, and ilmenorutile and those captured by the authigenic anatase remains an unanswered question in this study.

The authigenic iron oxide hematite is seen in thin sections as a cement, occluding pore space (Amireh, 2020, fig. 3B), or forming rims surrounding detrital framework grains, or as patches and/or discrete, hexagonal crystals, replacing the detrital, ferruginous, clayey matrix (Fig. 4E). All these forms of authigenic hematite are seen in thin sections of most samples of the four sandstone suites and further identified by the XRD technique. Moreover, another minor type of authigenic hematite is encountered in the sandstone, overlying the Rum Unconformity surface, as hematite/leucoxene that represents an alteration product of detrital ilmenite (Amireh, 2020, fig. 5A, C). The hematite cement postdates all the diagenetic minerals mentioned above, except secondary, sparry calcite cement.

The hematite cement originated mainly by direct precipitation in pore spaces during early to late diagenesis, or even after uplift (Amireh, 1987, 2018, 2020) under oxic conditions, as is well known (Tucker, 2001). It is often recorded that iron oxides, including hematite, are sinks to numerous TEs, such as Zn, Co, Cr, Ni, and V, and REEs (Cave and Harmon, 1997; Ni *et al.*, 2009, and the references therein). Similarly, these elements probably were captured by the authigenic hematite, present in one or more of the sandstone suites, since there is a good to very good correlation of Fe with Co, Ga, Ni, Rb, Sc, V and Zn (Supplementary Tab. 4).

## CONCLUSIONS

1. Provenance of the lower Cambrian–Lower Cretaceous sandstones and mudstones of Jordan was a mixed one, mainly felsic, and rarely mafic, crystalline rocks of the late Neoproterozoic Arabian Shield, and to a lesser extent Palaeozoic and lower–middle Mesozoic siliciclastic strata.
2. The major, felsic provenance is constrained by the high abundance of Ba, Rb, Zr, Hf, and Th, the low abundance of Ti, Sc, Cr, Ni, Zn, and Cu, high Th/Sc, Y/Ni, and Ba/S, and low Cr/Th, Ti/Zr, Ti/La $\times$ 20, and Ce/Th.
3. High Cr/Ni indicates a minor, mafic provenance, whereas a recycled, siliciclastic provenance is inferred from the high amounts of SiO<sub>2</sub>.
4. The REEs patterns, the distribution of large-ion lithophile, high field strength, the transitional trace elements in both detrital and authigenic, light and heavy minerals of the sandstones are controlled principally by the source rocks provenance, followed by an interplay of chemical weathering, recycling, hydraulic sorting, locally low-temperature, hydrothermal metasomatism, depositional environment and redox conditions, and diagenesis.
5. Chemical weathering, recycling, hydraulic sorting, and low temperature, hydrothermal metasomatism caused fractionation of the REEs and the TEs in the sandstones and mudstones, which might also apply to other siliciclastics at different locations and in similar or unlike, stratigraphic positions.

## REFERENCES

6. Intensive, chemical weathering of the provenance source rocks led to depletion of all the REEs and depletion of Zr, Hf, Ba, Cr, Cs, Ga, Rb, Sc, Sr, V, Y, and Zn, compared to UCC.
  7. Subsequent recycling of the sandstone was responsible for depletion of all the REEs, and depletion of Cu, Ga, Pb, Sn, Sr, W, Y and Zn, but on the other hand, it caused enrichment of Zr, Hf, Th, U, Ba, Co, Cr, Cs, Nb, Ni, Rb, Ta, Sc, and V.
  8. Later hydraulic sorting led to enrichment of Al, K, most REEs and most TEs in the detrital clay minerals and enrichment of Ti, Nb, Ta and REEs in the silt-sized rutile/anatase, enrichment of Zr and Hf, hosted solely by very fine sand-sized zircon, and enrichment of Si in the sand-sized fraction.
  9. Scandium abundance increased with decreasing grain size from coarse sand to very fine sand, then markedly to the mud fraction. Thus, the mudstones are more enriched in Sc than the average sandstone.
  10. The REE are hosted mainly in zircon of very fine sand size and in the silt-sized Ti-bearing minerals (rutile and anatase, among others) and subordinately in clay minerals.
  11. The value of the Eu negative anomaly was increased significantly by recycling and low-temperature, hydrothermal metasomatism, whereas it very likely decreased during chemical weathering.
  12. The subarkosic arenites invariably exhibit higher concentrations of all REEs and all TEs, compared to the quartz arenites, reflecting the provenance signature.
  13. The bivariate trace elements plots, Y vs. Nb, Yb vs. Ta, (Y + Nb) vs. Rb, and (Yb + Ta) vs. Rb, although originally established for igneous rocks, can be applied successfully to siliciclastic successions.
  14. The inferred volcanic arc tectonic setting of the granitic source rocks provenance of the sandstone and mudstone agrees with the collisional and accretionary tectonic processes that led to the formation of the Arabian-Nubian Shield during the Pan African, thermo-tectonic event of the late Neoproterozoic amalgamation phase of NE Gondwana.
  15. On the basis of the ternary plots La-Th-Sc and Th-Sc-Zr/10, a passive continental margin is constrained as the final tectonic setting of the provenance subsequent to the late Neoproterozoic volcanic arc tectonism.
  16. Ce/Ce\* vs. Pr/Pr\* plot, and Ni/Co, V/(V + Ni), V/Cr, and U/Th redox proxies point to an oxic condition of deposition of the marine, subarkosic arenites as well as the fluvial, subarkosic arenites and quartz arenites.
- Acknowledgements**
- The Deanship of Scientific Research, the University of Jordan, is acknowledged for financial support of the research. Thanks go to Waddah Mahmoud for carrying out the SEM analysis, and to Miss Saja Abu Taha for drawing the line diagrams. The editor Bartosz Budzyń, the Editor-in-Chief Alfred Uchman, the reviewer Martin J. Timmerman and an anonymous reviewer are acknowledged for their valuable comments that significantly improved the paper. The manuscript has been English proofread by Frank Simpson and edited by Ewa Malata, who are both greatly acknowledged.
- REFERENCES**
- Abed, A. M., Makhlof, I. M., Amireh, B. S. & Khalil, B., 1993. Upper Ordovician glacial deposits in southern Jordan. *Episodes*, 16: 316–328.
- Abdelsalam, M. G. & Stern, J., 1996. Sutures and shear zones in the Arabian-Nubian Shield. *Journal of African Earth Sciences*, 23: 289–310.
- Al Shanti, A. M., 2009. *Geology of the Arabian Shield*. Scientific Publishing Center, King Abdulaziz University, Jeddah, 190 pp.
- Ali, S., Stattegger, K., Garbe-Schönberg, D., Frank, M., Kraft, S. & Kuhnt, W., 2014. The provenance of Cretaceous to Quaternary sediments in the Tarfaya Basin, SW Morocco: evidence from trace element geochemistry and radiogenic Nd-Sr isotopes. *Journal of African Earth Sciences*, 90: 64–76.
- Amireh, B. S., 1987. *Sedimentological and Petrological Interplays of the Nubian Series in Jordan with Regard to Paleogeography and Diagenesis*. Unpublished Ph.D. Thesis. TU Braunschweig, 232 pp.
- Amireh, B. S., 1991. Mineral composition of the Cambrian-Cretaceous Nubian Series of Jordan: provenance, tectonic setting and climatological implications. *Sedimentary Geology*, 71: 99–119.
- Amireh, B. S., 1992. Sedimentology and mineral composition of the Kurnub Sandstone in Wadi Qsieb, SW Jordan. *Sedimentary Geology*, 78: 267–283.
- Amireh, B. S., 1993. Three paleosols of the Nubian Series of Jordan: Climatologic, tectonic and paleogeographic implications. *Dirasat*, 20B: 33–62.
- Amireh, B. S., 1994. Heavy and clay minerals as tools in solving stratigraphic problems: a case study from the Disi Sandstone (Early Ordovician) and the Kurnub Sandstone (Early Cretaceous) of Jordan. *Neues Jahrbuch für Geologie und Paläontologie, Monatshefte*, 4: 205–222.
- Amireh, B. S., 1997. Sedimentology and paleogeography of the regressive-transgressive Kurnub Group (Early Cretaceous) of Jordan. *Sedimentary Geology*, 112: 69–88.
- Amireh, B. S., 2000. The Early Cretaceous Kurnub Group of Jordan: Subdivision, characterization and depositional environment development. *Neues Jahrbuch für Geologie und Paläontologie, Monatshefte*, 1: 29–57.
- Amireh, B. S., 2015. Grain size analysis of the lower Cambrian-lower cretaceous clastic sequence of Jordan: sedimentological and paleo-hydrodynamic implications. *Journal of Asian Earth Sciences*, 97: 67–88.
- Amireh, B. S., 2018. Petrogenesis of the NE Gondwanan uppermost Ediacaran–Lower Cretaceous siliciclastic sequence of Jordan: Provenance, tectonic, and climatic implications. *Journal of Asian Earth Sciences*, 154: 316–341
- Amireh, B. S., 2020. Weathering, recycling, hydraulic sorting and metamorphism/metasomatism implications of the NE Gondwana lower Cambrian–Lower Cretaceous siliciclastic succession of Jordan. *Journal of Asian Earth Sciences*, 191: 104228. <https://doi.org/10.1016/j.jseae.2020.104228>
- Amireh, B. S. & Abed, A. M., 1999. Depositional environments of the Kurnub Group (Early Cretaceous) in northern Jordan. *Journal of African Earth Sciences*, 29: 449–468.
- Amireh, B. S., Amaireh, M. N. & Abed, A. M., 2008. Tectono-sedimentary evolution of the Umm Ghaddah Formation (late

- Ediacaran–early Cambrian) in Jordan. *Journal of Asian Earth Sciences*, 33: 194–218.
- Amireh, B. S., Amaireh, M. N., Abu Taha, S. & Abed, A. M., 2019. Petrogenesis, provenance, and rare earth element geochemistry, southeast desert phosphorite, Jordan. *Journal of African Earth Sciences*, 150: 701–721.
- Amireh, B. S., Henius-Kunst, F., Jarrar, G. H. & Schneider, W., 1998. K-Ar dating, X-ray diffractometry, optical and scanning electron microscopy of glauconies from the Early Cretaceous Kurnub Group of Jordan. *Geological Journal*, 33: 49–65.
- Amireh, B. S., Schneider, W. & Abed, A. M., 1994a. Evolving fluvial-transitional-marine deposition through the Cambrian sequence of Jordan. *Sedimentary Geology*, 89: 65–90.
- Amireh, B. S., Schneider, W. & Abed, A., 1994b. Diagenesis and burial history of the Cambrian–Cretaceous sandstone series in Jordan. *Neues Jahrbuch für Geologie und Paläontologie, Abhandlungen*, 192: 151–181.
- Amireh, B. S., Schneider, W. & Abed, A., 2001. Fluvial-shallow marine-glaciofluvial depositional environments of the Ordovician System in Jordan. *Journal of Asian Earth Sciences*, 19: 45–60.
- Anonymous, 2005. *Geochemical Atlas of Europe*. The Association of the Geological Surveys of the European Union (EuroGeoSurveys)/the Geological Survey of Finland, 9 pp.
- Avigad, D., Kolodner, K., McWilliams, M., Persing, H. & Weissbrod, T., 2003. Origin of northern Gondwana Cambrian sandstone revealed by detrital zircon SHRIMP dating. *Geology*, 31: 227–230.
- Avigad, D., Morag, N., Abbo, A. & Gerdes, A., 2017. Detrital rutile U-Pb perspective on the origin of the great Cambro-Ordovician sandstone of North Gondwana and its linkage to orogeny. *Gondwana Research*, 51: 17–29.
- Avigad, D., Weissbrod, T., Gerdes, A., Zlatkin, O., Ireland, T. R. & Morag, N., 2015. The detrital zircon U-Pb-Hf fingerprint of the northern Arabian-Nubian Shield as reflected by a late Ediacaran arkosic wedge (Zenifim formation; subsurface Israel). *Precambrian Research*, 266: 1–11.
- Basu, A., Bickford, M. & Deasy, R., 2016. Inferring tectonic provenance of siliciclastic rocks from their chemical compositions: A dissent. *Sedimentary Geology*, 336: 26–35.
- Bau, M. & Dulski, P., 1996. Distribution of yttrium and rare-earth elements in the Penge and Kuruman iron-formations, Transvaal Supergroup, South Africa. *Precambrian Research*, 59: 37–55.
- Bender, F., 1968. *Geologie von Jordanien*. 7. Beiträge zur regionalen Geologie der Erde. Gebrüder Borntraeger Bornträger, Berlin, 230 pp.
- Ben sera, A. S., 2018. *Petrogenesis, geochemistry and Geochronology of Granitic and Granodioritic Suites in Aqaba Complex, Southern Jordan; Constraints from U-Pb Zircon Ages*. Unpublished Doctoral Dissertation, University of Jordan, 141 pp.
- Bhatia, M. R. & Crook, A. W., 1986. Trace element characteristics of graywackes and tectonic setting discrimination of sedimentary basins. *Contribution to Mineralogy and Petrology*, 92: 181–193.
- Biscaye, P. E., 1965. Mineralogy and sedimentation of Recent deep-sea clays in the Atlantic and adjacent seas and oceans. *Geological Society American Bulletin*, 76: 803–832.
- Blake, J. M., Peters, S. C. & Johannesson, K. H., 2017. Application of REE geochemical signatures for Mesozoic sediment provenance to the Gettysburg Basin, Pennsylvania. *Sedimentary Geology*, 349: 103–111.
- Bouch, J. E., Hole, M., Trewin, J. H., Chenery, S. & Morton, A. C., 2002. Authigenic apatite in a fluvial sandstone sequence: evidence for rare-earth element mobility during diagenesis and a tool for diagenetic correlation. *Journal of Sedimentary Research*, 72: 59–67.
- Bouch, J. E., Hole, M. J., Trewin, N. H. & Morton, A. C., 1995. Low-temperature aqueous mobility of the rare-earth elements during sandstone diagenesis: *Geological Society of London, Journal*, 152: 895–898.
- Cave, M. R. & Harmon, K., 1997. Determination of trace metal distributions in the iron oxide phases of red bed sandstones by chemometric analysis of whole rock and selective Leachate data. *Analyst*, 122: 501–512.
- Condie, K. C., 1991. Another look at rare earth elements in shales. *Geochimica et Cosmochimica Acta*, 55: 2527–2531.
- Condie, K. C., 1993. Chemical composition and evolution of the upper continental crust: contrasting results from surface samples and shales. *Chemical Geology*, 104: 1–37.
- Cullers, R. L., 1988. Mineralogical and chemical changes of soil and stream sediment formed by intense weathering of the Danberg granite, Georgia, U.S.A. *Lithos*, 21: 301–314.
- Cullers, R. L., 1994. The controls on the major and trace element variation of shales, siltstones, and sandstones of Pennsylvanian-Permian age from uplifted continental blocks in Colorado to platform sediment in Kansas, USA. *Geochimica et Cosmochimica Acta*, 58: 4955–4972.
- Cullers, R. L., 1995. The controls on the major- and trace-element evolution of shales, siltstones and sandstones of Ordovician to Tertiary age in the Wet Mountains region, Colorado, U.S.A. *Chemical Geology*, 123: 107–131.
- Cullers, R. L., Chaudhuri, S., Kilbane, N. & Koch, R., 1979. Rare earths in size fractions and sedimentary rocks of Pennsylvanian-Permian age from the mid-continent of the U.S.A. *Geochimica et Cosmochimica Acta*, 43: 1285–1302.
- Dickinson, W. R., Beard, L. S., Brakenridge, G. R., Erjavec, J. L., Ferguson, R. C., Inman, K. F. & Ryberg, P. T., 1983. Provenance of North American Phanerozoic sandstones in relation to tectonic setting. *Geological Society American Bulletin*, 94: 222–235.
- Dumoulin, J. A., Slack, J. F., Whalen, M. T. & Harris, A. G., 2011. Depositional setting and geochemistry of phosphorites and metalliferous black shales in the Carboniferous–Permian Lisburne Group, Northern Alaska. *United States of America Geological Survey Professional Paper*, 1776: 1–64.
- Elderfield, H. & Greaves, M. J., 1982. The rare earth elements in seawater. *Nature*, 296: 214–219.
- Feng, R. & Kerrich, R., 1990. Geochemistry of fine-grained clastic sediments in the Archaean Abitibi Greenstone Belt, Canada: Implications for provenance and tectonic setting. *Geochimica et Cosmochimica Acta*, 54: 1061–1081.
- Füchtbauer, H., 1974. *Sediments and Sedimentary Rocks, Part II, Sedimentary Petrology*. Wiley, New York, 464 pp.
- Ghanem, H. & Jarrar, G. H., 2013. Geochemistry and petrogenesis of the 595 Ma shoshonitic Qunai monzogabbro, Jordan. *Journal of African Earth Sciences*, 88: 1–14.

- Gvirtzman, G. & Weissbrod, T., 1984. The Hercynian Geanticline of Heleze and the late Paleozoic history of the Levant. In: Dixon, J. E. & Robertson, A. H. (eds), *The Geological Evolution of the Eastern Mediterranean. Geological Society of London, Special Publication*, 17: 177–186.
- Husseini, M. I., 2000. Origin of the Arabian plate structures: Amar collision and Najd rift. *GeoArabia*, 5: 527–542.
- Jarrar, G. H., Amireh, B. S. & Zachman, D., 2000. The major, trace and rare earth element geochemistry of glauconites from the Early Cretaceous Kurnub Group of Jordan. *Geochemical Journal*, 34: 207–222.
- Jarrar, G. H., Stern, R. J., Saffarini, G. & Al-Zubi, H., 2003. Late- and postorogenic Neoproterozoic intrusions of Jordan: implications for crustal growth in the northernmost segment of the East African Orogen. *Precambrian Research*, 123: 295–319.
- Jones, B. & Manning, A. C., 1994. Comparison of geochemical indices used for the interpretation of Paleoredox conditions in ancient mudstone. *Chemical Geology*, 11: 111–129.
- Kolodner, K., Avigad, D., Ireland, T. R. & Garfunkel, Z., 2009. Origin of Lower Cretaceous ('Nubian') sandstones of Northeast Africa and Arabia from detrital zircon U-Pb SHRIMP dating. *Sedimentology*, 56: 2010–2023.
- Kolodner, K., Avigad, D., McWilliams, M., Wooden, J., Weissbrod, T. & Feinstein, S., 2006. Provenance of north Gondwana Cambrian–Ordovician sandstone: U-Pb SHRIMP dating of detrital zircons from Israel and Jordan. *Geological Magazine*, 143: 367–391.
- Kröner, A., 1984. Late Precambrian plate tectonic and orogeny: A need to redefine the term Pan-African. In: Klerks, J. & Michot, J. (eds), *African Geology*. Musée, R., l'Afrique Centrale, Tervuren, pp. 23–28.
- Kröner, A., Eyal, M. & Eyal, Y., 1990. Early Pan-African evolution of the basement around Elat, Israel, and the Sinai Peninsula revealed by single-zircon evaporation dating, and implications for crustal accretion rates. *Geology*, 18: 545–548.
- Lawrence, R., Cox, R., Mapes, R. & Coleman, D., 2011. Hydrodynamic fractionation of zircon age populations. *Geological Society American Bulletin*, 123: 295–305.
- McBride, E. F., 1987. Diagenesis of the Maxon Sandstone (Early Cretaceous), Marathon region, Texas; a diagenetic quartzarenite. *Journal of Sedimentary Petrology*, 57: 98–107.
- McLennan, S. M., 2001. Relationships between the trace element composition of sedimentary rocks and upper continental crust. *Geochemistry, Geophysics, Geosystems* 2, 2000GC000109.
- McLennan, S. M., Hemming, S., McDaniel, D. K. & Hanson, G. N., 1993. Geochemical approaches to sedimentation, provenance, and tectonics. In: Johnsson, M. J. & Basu, A. (eds), *Processes Controlling the Composition of Clastic Sediments: Boulder, Colorado. Geological Society of America Special Paper*; 284: 21–40.
- Moore, D. M. & Reynolds Jr., R. C., 1989. *X-Ray Diffraction and the Identification and Analysis of Clay Minerals*. Oxford University Press, Oxford, pp. 179–201.
- Morag, N., Avigad, D., Gerdes, E. & Harlavan, Y., 2012. 1000–580 Ma crustal evolution in the Northern-Arabian Shield revealed by U-Pb-Hf of detrital zircons from late Neoproterozoic sediments (Eilat area, Israel). *Precambrian Research*, 208: 197–212.
- Morton, A. C. & Hallsworth, C. R., 1999. Processes controlling the composition of heavy mineral assemblages in sandstones. *Sedimentary Geology*, 124: 3–29.
- Müller, G., 1967. *Methods in Sedimentary Geology, Part I. Sedimentary Petrology*. Schweizerbart, Stuttgart, 283 pp.
- Nance, W. B. & Taylor, S. R., 1976. Rare earth element patterns and crustal evolution—I. Australian post-Archean sedimentary rocks. *Geochimica et Cosmochimica Acta*, 40: 1539–1551.
- Nesbitt, H. W. & Markovics, G., 1997. Weathering of granodioritic crust, long-term storage of elements in weathering profiles, and petrogenesis of clastic sediments. *Geochimica et Cosmochimica Acta*, 61: 1653–1670.
- Nesbitt, H. W. & Young, G. M., 1982. Early Proterozoic climates and plate motions inferred from major element chemistry of lutites. *Nature*, 299: 715–717.
- Nesbitt, H. W. & Young, G. M., 1984. Prediction of some weathering trends of plutonic and volcanic rocks based on thermodynamic and kinetic considerations. *Geochimica et Cosmochimica Acta*, 48: 1523–1534.
- Ni, Sh., Ju, Y., Hou, Q., Wang, Sh., Liu, Q., Wua, Y. & Xiao, L., 2009. Enrichment of heavy metal elements and their adsorption on iron oxides during carbonate rock weathering process. *Progress in Natural Science*, 19: 1133–1139.
- O'Sullivan, D., Marengo, F., Ryder, C. L., Pradhan, Y., Kipling, Z., Johnson, B., Benedetti, A., Brooks, M., McGill, M., Yorks, J. & Selmer, P., 2020. Models transport Saharan dust too low in the atmosphere: a comparison of the MetUM and CAMS forecasts with observations. *Atmospheric Chemistry and Physics*, 20: 12955–12982.
- Pearce, J. A., Harris, N. B. & Tindle, A. G., 1984. Trace element discrimination diagrams for the tectonic interpretation of granitic rocks. *Journal of Petrology*, 25: 956–983.
- Pi, H., Feng, G., Sharratt, B. S., Li, X. & Zheng, Z., 2014. Validation of SWEEP for contrasting agricultural land use types in the Tarim Basin. *Soil Science*. 179: 433–445.
- Powell, J. H., Abed, A. M. & Le Nindre, Y. M., 2014. Cambrian stratigraphy of Jordan. *GeoArabia*, 19: 81–134.
- Rasmussen, B., 1996. Early diagenetic REE-phosphate minerals (florencite, gorceixite, crandallite, and xenotime) in marine sandstones: A major sink for oceanic phosphorus. *American Journal of Science*, 296: 601–632.
- Riboulleau, A., Bout-Roumazielles, V. & Tribouillard, N., 2014. Controls on detrital sedimentation in the Cariaco Basin during the last climatic cycle: insight from clay minerals. *Quaternary Science Review*, 94: 62–73.
- Romans, P. A., Brown, L. L. & White, J. C., 1975. An electron microprobe study of yttrium, rare earth, and phosphorus distributions in zoned and ordinary zircon. *American Mineralogist*, 60: 475–480.
- Roser, B. P. & Korsch, R. J., 1986. Determination of tectonic setting of sandstone-mudstone suites using SiO<sub>2</sub> content and K<sub>2</sub>O/Na<sub>2</sub>O ratios. *Journal of Geology*, 94: 635–650.
- Roser, B. P. & Korsch, R. J., 1988. Provenance signatures of sandstone-mudstone suites determined using discriminant function analysis of major-element data. *Chemical Geology*, 67: 119–139.
- Rudnick, R. & Gao, S., 2003. Composition of the continental crust. In: Holland, H. D. & Turekian, K. K. (eds), *Treatise on Geochemistry*, 3. Elsevier-Pergamon, Oxford, pp. 1–64.

- Saffarini, G. A. & Amireh, B. S., 2016. Distinguishing depositional environments of the Lower Cambrian– Lower Cretaceous siliciclastic sequence of Jordan using geostatistical techniques: A proposal. *Arabian Journal of Geosciences*, 9: 1–16.
- Saint-Marc, P., 1978. Arabian Peninsula. In: Moullade, M. & Nairn, A. E. (eds), *The Phanerozoic Geology of the World 11, The Mesozoic*, A. Elsevier, Amsterdam, pp. 435–462.
- Samuel, M. D., Be'eri-Shlevin, Y., Azer, M. K., Whitehouse, M. J. & Moussa, H. E., 2011. Provenance of conglomerate clasts from the volcano-sedimentary sequence at Wadi Rutig in southern Sinai, Egypt as revealed by SIMS U-Pb dating of zircon. *Gondwana Research* 20: 450–464.
- Sandler, A., Teutsch, N. & Avigad, D., 2012. Sub-Cambrian pedogenesis recorded in weathering profiles of the Arabian-Nubian Shield. *Sedimentology*, 59: 1305–1320.
- Schneider, W., Amireh, B. S. & Abed, A. M., 2007. Succession analysis of the Early Paleozoic sedimentary systems of Jordan. *Zeitschrift der Deutschen Gesellschaft für Geowissenschaften*, 158: 225–247.
- Segev, A., Halicz, L., Steinitz, G. & Lang, B., 1995. Post-depositional processes on a buried Cambrian succession in southern Israel, north Arabian Massif: evidence from new K-Ar dating of Mn-nodules. *Geological Magazine*, 132: 475–385.
- Smith, M. P., Henderson, P., Jeffries, T. R., Long, J. & Williams, C. T., 2004. The rare earth elements and uranium in garnet from the Beinn an Dubhaich Aureole, Skye, Scotland, UK: Constrains on processes in a dynamic hydrothermal system. *Journal of Petrology*, 45: 457–484.
- Speer, J. A., 1980. Zircon. *Reviews in Mineralogy and Geochemistry*, 5: 67–112.
- Stephenson, M. & Powell, J., 2013. Palynology and alluvial architecture in the Permian Umm Irna Formation, Dead Sea, Jordan. *GeoArabia*, 18: 17–60.
- Taylor, S. R. & McLennan, S. M., 1985. *The Continental Crust: Its Composition and Evolution*. Blackwell, Oxford, 312 pp.
- Tucker, M., 2001. *Sedimentary Petrology*, 2<sup>nd</sup> ed. Blackwell Science, Oxford, 262 pp.
- Vermeesch, P., Avigad, D. & McWilliams, M. O., 2009. 500 m. y. of thermal history elucidated by multi-method detrital thermochronology of North Gondwana Cambrian sandstone (Eilat, Israel). *Geological Society of America Bulletin*, 121: 1204–1216.
- Warr, L. N., 2021. IMA-CNMNC approved mineral symbols. *Mineralogical Magazine*, 85: 291–320.
- Wedepohl, K. H., 1995. The composition of the continental crust. *Geochimica et Cosmochimica Acta*, 59: 1217–1232.
- Weissbrod, T. & Nachmias, Y., 1986. Stratigraphic significance of heavy minerals in the Late Precambrian-Mesozoic clastic succession (Nubian Sandstone) in the near East. *Sedimentary Geology*, 47: 263–291.
- White, W. M., 2013. *Geochemistry*. Wiley-Blackwell, West Sussex, 660 pp.
- White, W. M. & Klein, E., 2013. Composition of the oceanic crust. In: Rudnick, R. L. (ed.), *The Crust. Treaties in Geochemistry* 3. Elsevier, Amsterdam, pp. 457–492.
- Wright, J., Schrader, H. & Holser, W. T., 1987. Paleoredox variations in ancient oceans recorded by rare earth elements in fossil apatite. *Geochimica et Cosmochimica Acta*, 51: 631–644.
- Zhao, M.-Y. & Zheng, Y.-F., 2015. The intensity of chemical weathering: Geochemical constraints from marine detrital sediments of Triassic age in South China. *Chemical Geology*, 391: 111–122.

## Supplementary Table 1

Major element abundance (in wt.%) for the individual samples in suites, the means of grain sizes, suites, standards and reference rocks (from Amireh, 2020) and the CIA values.

Element	SiO <sub>2</sub>	Al <sub>2</sub> O <sub>3</sub>	Fe <sub>2</sub> O <sub>3</sub>	CaO	MgO	Na <sub>2</sub> O	K <sub>2</sub> O	TiO <sub>2</sub>	MnO	P <sub>2</sub> O <sub>5</sub>	LOI	Total	CIA
An. Prec.	0.01	0.01	0.01	0.01	0.01	0.01	0.01	0.01	0.01	0.01	0.01	0.01	
Sandstone suite 1 (n = 9)													
SR1	75	11.25	3.35	0.23	0.25	0.11	4.46	1.44	0.02	0.11	3.13	99.46	69
SR5	91.9	3.33	0.09	0.26	0.02	0.03	0.96	0.12	b.d.	0.07	1.27	98.08	71
SD1	91.4	3.62	0.13	0.26	0.07	0.06	1.4	0.63	b.d.	0.06	1.29	98.97	70
SD3	95.8	2.35	0.39	0.15	0.05	0.03	1.08	0.16	b.d.	0.02	0.75	100.8	71
SD7	89.7	3.91	0.15	0.44	0.13	0.06	1.96	0.19	0.01	0.2	1.41	98.21	66
SD9	91.2	3.62	0.58	0.65	0.07	0.05	1.78	0.19	0.01	0.03	1.21	99.44	62
AK2	94.7	2.44	0.07	0.07	0.06	0.09	0.63	0.11	b.d.	0.03	1.12	99.34	74
Ak6	92.1	4.64	0.1	0.2	0.04	0.05	1.2	0.19	b.d.	0.04	1.62	100.22	74
AK11	88.5	5.95	0.17	0.14	0.12	0.1	1.92	0.64	b.d.	0.06	2.2	99.87	75
Mean	90.03	4.57	0.56	0.27	0.09	0.06	1.71	0.41	0.01	0.07	1.56	99.38	70
Sandstone suite 2 (n = 14)													
SR10	95.3	2.39	0.28	0.24	0.01	0.01	0.04	0.09	b.d.	0.1	1.33	99.79	90
AK15	92.1	2.54	0.08	1.71	0.01	b.d.	0.03	0.17	b.d.	1.08	1.49	100.94	82
UI1	95.9	2.62	0.14	0.52	0.01	0.01	0.06	0.08	b.d.	0.32	1.39	101.05	91
UI5	95.5	2.3	0.22	0.58	0.02	0.01	0.02	0.18	b.d.	0.09	2.19	101.15	73
UI9B	94	3.93	0.09	0.48	0.02	0.01	0.04	0.24	b.d.	0.03	2.07	100.92	82
UI17	94.5	1.6	0.56	1.2	0.17	0.06	0.04	0.13	b.d.	0.02	2.07	100.37	54
DS1	95	2.03	0.09	0.03	0.02	0.01	0.02	0.07	b.d.	0.02	1.08	98.37	98
DS2	94.7	2.25	0.05	0.19	0.01	b.d.	0.01	0.18	b.d.	0.01	1.28	98.69	87
DS6	95.2	2.32	0.03	0.02	b.d.	b.d.	0.01	0.14	b.d.	0.03	1.19	98.96	99
DS15	98.1	0.47	0.02	1.36	0.04	b.d.	0.01	0.04	b.d.	0.02	1.71	101.78	25
US1	98.3	0.59	0.18	0.07	0.06	b.d.	0.04	0.06	b.d.	0.02	0.65	99.97	84
US4	97.6	0.37	0.02	1.32	0.01	b.d.	b.d.	0.11	b.d.	0.02	1.48	100.93	22
US10	96.5	1.78	0.03	0.06	0.01	0.01	0.01	0.05	b.d.	0.01	1.04	99.5	94
US12	96.9	0.8	0.04	0.21	0.01	b.d.	0.01	0.13	b.d.	0.03	0.79	98.92	72
Mean	95.69	1.86	0.13	0.57	0.03	0.02	0.03	0.12	b.d.	0.13	1.41	100.1	75
Sandstone suite 3 (n = 24)													
H6	57.4	18.35	7.67	0.41	2.61	0.68	4.34	0.96	0.04	0.12	8.1	100.83	80
H9	82.7	9.02	1	0.59	0.36	0.2	3.61	0.31	0.03	0.02	2.68	100.68	65
D3	91.4	4.08	0.38	0.15	0.14	0.07	1.8	0.48	0.01	0.02	1.14	99.75	64
D5A	91.7	3.12	0.54	0.06	0.12	0.07	1.78	1.45	b.d.	0.04	0.76	99.73	61
D10	89.2	4.45	0.85	0.08	0.24	0.1	2.02	1.02	0.01	0.03	1.41	99.51	65
D19	90.2	4.6	0.9	0.12	0.12	0.14	1.59	0.17	0.01	0.01	1.35	99.27	68
D23	82.3	8.85	0.82	0.56	0.37	1.74	2.9	0.31	0.03	0.03	1.88	99.88	70
DMZ1	91.5	4.26	0.59	0.11	0.22	0.06	1.56	0.57	0.01	0.04	1.24	100.23	69
DMZ10	87.9	2.48	0.56	3.94	0.26	0.05	1.31	0.2	0.13	0.02	3.76	100.67	31
DMZ12	83.4	7.95	0.72	0.41	0.29	0.15	3.91	0.54	0.03	0.02	1.66	99.22	63
DMZ13	91.1	4.18	0.44	0.28	0.17	0.07	1.87	0.67	b.d.	0.02	1.06	99.94	62
TB1	88.5	5.43	0.38	0.82	0.18	0.31	2.99	0.06	b.d.	0.04	1.72	100.53	55
TB4	67.8	12.85	3.42	0.59	1.68	1.9	3.05	0.52	0.02	0.05	7.13	99.12	78
TB9	90.2	3.63	0.56	0.93	0.07	0.31	2.07	0.16	0.02	0.54	0.79	99.36	59
AM1	76.2	10.1	2.74	0.19	1.02	1.55	2.9	0.51	0.02	0.08	3.32	98.74	75
AM5	89.3	4.11	0.71	0.35	0.31	0.15	1.59	0.3	0.02	0.07	2.07	99.05	63

Element	SiO <sub>2</sub>	Al <sub>2</sub> O <sub>3</sub>	Fe <sub>2</sub> O <sub>3</sub>	CaO	MgO	Na <sub>2</sub> O	K <sub>2</sub> O	TiO <sub>2</sub>	MnO	P <sub>2</sub> O <sub>5</sub>	LOI	Total	CIA
AM8	88.6	5.42	1.33	0.19	0.08	0.09	2.31	0.22	b.d.	0.04	1.59	99.96	65
BT2	81.4	8.39	1.59	0.13	0.29	0.14	3.79	0.23	0.03	0.07	2.14	98.33	66
RS3	62	9.1	2.74	6.42	3.22	1.02	3.38	0.85	0.37	0.04	9.73	99.03	46
RS5	75.2	11.9	1.68	0.5	0.74	1.5	4.35	0.64	0.04	0.06	3.03	99.81	68
RS11	74.7	8.25	1.43	4	0.29	0.78	3.68	0.84	0.1	0.09	4.63	98.94	51
KH1	76.8	10.6	2	0.26	0.39	0.7	3.69	1.5	0.01	0.07	3.28	99.42	70
KH2	81.1	6.62	0.45	0.26	0.08	0.63	3.47	1.95	0.01	0.13	1.7	98.89	62
KH4	76.4	7.92	1.53	2.09	0.26	0.53	4.1	1.11	0.01	0.05	4.63	98.76	53
Mean	81.96	7.32	1.46	0.98	0.56	0.54	2.84	0.65	0.05	0.07	2.95	99.57	63
Sandstone suite 4 (n = 11)													
TB13	95.7	1.7	0.64	0.94	0.07	0.04	0.99	0.08	b.d.	0.08	1.02	101.31	55
K1	97.6	0.8	0.37	0.04	0.01	b.d.	0.01	0.02	b.d.	0.01	0.58	99.44	93
K3	99	0.17	0.64	0.01	0.01	b.d.	b.d.	0.15	b.d.	0.01	0.34	100.33	95
K6	99.5	0.83	0.34	0.01	0.01	b.d.	0.03	0.1	b.d.	b.d.	0.57	101.39	94
HM8	95.8	1.46	0.19	0.02	0.01	b.d.	0.02	0.19	b.d.	0.01	0.77	98.47	97
R1	93.4	4.13	0.48	0.03	0.13	0.01	0.17	0.61	0.03	0.02	2.08	101.11	99
R4	98	0.33	0.09	0.01	0.02	b.d.	0.01	0.03	b.d.	b.d.	0.38	98.87	91
R9	99.7	0.06	0.09	0.03	0.01	b.d.	b.d.	0.05	b.d.	0.02	0.33	100.29	88
J25	98.3	0.19	0.07	0.02	0.01	b.d.	0.01	0.03	b.d.	b.d.	0.36	98.99	80
BF1	88.6	6.47	0.35	0.04	0.2	0.05	0.45	1.08	b.d.	0.02	3.13	100.43	97
BF10	90.6	3.11	2.99	0.05	0.09	b.d.	0.11	0.65	b.d.	0.04	1.78	99.45	99
Mean	96.02	1.75	0.57	0.11	0.05	0.03	0.2	0.27	0.03	0.03	1.03	100.01	90
Mudstone suite (n = 12)													
H1	49	27	0.89	0.09	0.32	0.37	2.32	0.9	b.d.	0.16	17.05	98.16	89
BT6	47.4	25.9	10.2	0.04	0.76	0.15	1.46	1.23	0.01	0.21	11.95	99.43	93
LO28	52.22	31.49	0.39	0.69	0.02	0.17	0.06	1.36	b.d.	0.15	12.43	98.98	95
M12	37.16	22.66	10.42	0.02	1.51	0.53	3.58	0.75	0.01	0.33	22.68	99.64	83
LS8	54.87	21.23	6.01	0.1	1.91	0.92	3.45	1.14	0.03	0.09	9.6	99.32	80
PTK1	50	26.07	14.75	0.06	0.04	0.18	0.09	0.39	0.01	0.04	10.15	101.77	98
TM7	50.48	26.72	7.07	0.22	1.11	0.21	3.22	1.25	0.01	0.04	12.08	100.81	86
T40	58.49	20.85	3.86	0.66	1.35	1.04	4.23	1.59	0.01	0.31	10.6	101.34	74
TA13	54.52	22.02	10.72	0.48	0.54	0.32	0.98	1.56	0.01	0.02	10.59	100.85	90
JH17	41.73	30.62	10.29	0.7	1.08	0.38	0.93	1.79	0.15	0.15	16.57	100.9	91
JA10	40.15	14.89	15.08	5.17	3.39	0.12	1.36	1.26	0.06	0.45	17.26	99.25	57
CrZ7	58.5	24.12	3.86	0.26	0.44	0.14	1	1.73	0.07	0.13	10.7	100.88	93
Mean	49.54	24.46	7.8	0.71	1.04	0.38	1.89	1.25	0.03	0.17	13.47	100.11	86
Averages													
CSM	90.69	4.21	0.75	0.26	0.11	0.05	1.56	0.47	0.02	0.07	1.5	99.71	74
US1	98.3	0.59	0.18	0.07	0.06	b.d.	0.04	0.06	b.d.	0.02	0.65	99.97	84
MSM	95.77	1.81	0.19	0.41	0.03	0.03	0.16	0.11	0.01	0.11	1.2	99.86	79
FSM	89.69	4.72	0.7	0.36	0.21	0.32	1.8	0.31	0.02	0.07	1.58	99.83	68
VFSM	79.85	7.85	1.79	1.22	0.68	0.56	2.8	0.86	0.07	0.06	3.61	99.55	66
AvSM	89.19	4.52	0.83	0.6	0.27	0.32	1.56	0.41	0.04	0.08	2	99.82	72
Mud	49.54	24.46	7.8	0.71	1.04	0.38	1.89	1.25	0.03	0.17	13.47	100.11	86
SAS1M	90.03	4.57	0.56	0.27	0.09	0.06	1.71	0.41	0.01	0.07	1.56	99.38	70
QAS2M	95.69	1.86	0.13	0.57	0.03	0.02	0.03	0.12	b.d.	0.13	1.41	100.1	75
SAS3M	81.96	7.32	1.46	0.98	0.56	0.54	2.84	0.65	0.05	0.07	2.95	99.57	63
QAS4M	96.02	1.75	0.57	0.11	0.05	0.03	0.22	0.27	0.03	0.03	1.03	100.01	90



Component	Framework particles %						Cements and authigenic minerals %										Matrix %	Sum
	Qz	Kfs	Pl	RF	Mca	TrHm	Qz	Kln	Ilt	Fe ox.	Cal	Dol	Brt	Fsp	Ap	Ant		
Sandstone suite 3 (n = 24)																		
H6	38	11	0	0	13	1	2	2	2	5	1	0	0	0	0	0	25	100
H9	67	7	0	0	2	0	8	6	0	2	1	3	0	0	0	0	4	100
D3	79	7	0	0	0	0	8	3	0	0	0	0	0	0	0	0	3	100
D5A	77	6	0	0	0	2	7.5	5	0	0	0	0	0	0	0	0.5	2	100
D10	72	9	0	0	0	2	7.7	0	0	5	0	1	0	0	0	0.3	3	100
D19	61	23	0	0	0	0	9.9	0	0	1	0	0	0	1	0	0.1	4	100
D23	50	26	1	0	2	1	5.9	8	0	1	0	2	0	1	0	0.1	2	100
DMZ1	73	8	0	0	1	1	9.9	1	0	1	0	1	0	0	0	0.1	4	100
DMZ10	71	8	0	0	0	0	0.9	0	0	1	10	3	0	0	0	0.1	6	100
DMZ12	70	12	0	0	0	1	4.9	0	0	2	2	1	0	0	0	0.1	7	100
DMZ13	72	15	0	0	1	1	3.9	0	0	1	1	1	0	0	0	0.1	4	100
TB1	66	13	0	0	0	0	9.9	0	0	1	2	2	0	1	0	0.1	3	100
TB4	50	12	0	0	6	1	2.9	0	0	4	3	1	0	0	0	0.1	20	100
TB9	63	20	0	0	0	2	5.9	0	0	1	3	0	0	1	0	0.1	4	100
AM1	47	15	4	0	6	1	2.9	0	0	2	2	0	0	0	0	0.1	20	100
AM5	64	16	1	0	2	0	4.9	0	0	0	1	0	0	0	0	0.1	11	100
AM8	60	21	0	0	0	0	4.9	0	0	2	0	0	0	0	0	0.1	12	100
BT2	56	19	0	0	2	0	3.8	0	0	2	0	0	0	0	0	0.2	17	100
RS3	45	14	0	0	7	1	4.6	3	0	4	13	0	0	0	0	0.4	8	100
RS5	50	26	0	0	4	1	7.9	0	0	1	3	0	0	0	0	0.1	7	100
RS11	59	14	1	0	2	0	4.8	0	0	2	8	0	0	0	0	0.2	9	100
KH1	63	14	0	0	3	2	5.9	0	0	4	3	0	0	0	0	0.1	5	100
KH2	69	13	0	0	1	0	4.9	0	0	1	2	0	4	0	0	0.1	5	100
KH4	67	13	0	0	3	2	3.6	0	0	2	4	0	0	0	0	0.4	5	100
Sandstone suite 4 (n = 11)																		
TB13KG	78	0	0	0	0	0	6.9	0	0	2	2	0	0	0	0	0.1	11	100
K1	87	0	0	0	0	0	6.9	0	0	1	0	0	0	0	0	0.1	5	100
K3	89	0	0	0	0	0	5.9	0	0	1	0	0	0	0	0	0.1	4	100
K6	82	0	0	0	0	0	11.9	0	0	1	0	0	0	0	0	0.1	5	100
HM8	79	0	0	0	0	1	5.8	0	0	6	0	0	0	0	0	0.2	8	100
R1	76	0	0	0	0	1	4.9	0	0	1	0	0	0	0	0	0.1	17	100
R4	88	0	0	0	0	0	9.9	0	0	0	0	0	0	0	0	0.1	2	100
R9	89	0	0	0	0	0	10.9	0	0	0	0	0	0	0	0	0.1	0	100
J25	87	0	0	0	0	0	12	0	0	0	0	0	0	0	0	0	1	100
BF1	70	0	0	0	0	0	7	0	0	1	0	0	0	0	0	0	22	100
BF10S	79	0	0	0	0	0	8.9	0	0	4	0	0	0	0	0	0.1	8	100

Qz – quartz, Kfs – K-feldspars, Pl – plagioclase, RF – rock fragments, Mic – micas, biotite, and muscovite, TrHm – transparent heavy minerals in thin sections, Kln – kaolinite, Ilt – illite, Fe ox. – iron oxide, Cal – calcite, Dol – dolomite, Brt – barite, Fsp – feldspar overgrowth, Ap – apatite, Ant – anatase.

## Supplementary Table 3

## Modal analysis of heavy minerals.

Heavy minerals and ratios	Zrn	Tur	Rt	Ap	Ant	St	Sa	Brt	Grt	Zo	TtHM	Tran./opaq	Tranwt %	Opag (wt%)	THMC (wt%)
Sandstone suite 1 (n = 9)															
SR1	87.5	0	1.4	11.1	0	0	0	0	0		100	0.09	0.56	5.7	6.26
SR5	17	34	2	40	5	0	2	0	0		100	4.2	0.08	0.03	0.11
SD1	39	25	12	20	4	0	0	0	0		100	0.07	0.16	2.1	2.26
SD3	65	23	6	0	6	0	0	0	0		100	0.16	0.24	1.23	1.47
SD7	20	20	0	60	0	0	0	0	0		100	0.16	0.07	0.38	0.45
SD9	33	17	8	25	0	0	17	0	0		100	0.1	0.07	0.65	0.72
AK2	49.6	40	10.4	0	0	0	0	0	0		100	2.25	0.03	0.02	0.05
Ak6	61.6	30.3	6.6	1.5	0	0	0	0	0		100	3.5	0.11	0.03	0.14
AK11	83.8	11.4	4.8	0	0	0	0	0	0		100	5.81	0.16	0.03	0.19
Mean	50.7	22.3	5.7	17.5	1.7	0	2.1	0	0		100	1.8	0.2	1.1	1.3
Sandstone suite 2 (n = 14)															
SR10	13.5	37.1	1.1	46	0	0	2.3	0	0		100	1.94	0.1	0.06	0.16
AK15UI	6.3	8.4	4.2	17.5	2.1	0	0	61.5	0		100	9.71	2	0.21	2.21
UI1	43.4	39.6	17	0	0	0	0	0	0		100	0.56	0.21	0.37	0.58
UI5	50	30	5	0	15	0	0	0	0		100	0.54	0.15	0.27	0.42
UI9B	71.4	14.3	14.3	0	0	0	0	0	0		100	4.5	0.07	0.01	0.08
UI17	30	42.4	23.8	3.8	0	0	0	0	0		100	0.64	0.28	0.44	0.72
DS1	54.2	21.4	24.4	0	0	0	0	0	0		100	1.59	0.03	0.02	0.05
DS2	41.7	32.9	20.3	0	5.1	0	0	0	0		100	0.7	0.13	0.18	0.31
DS6	59	25.3	15.7	0	0	0	0	0	0		100	0.5	0.05	0.1	0.19
DS15	41.5	45.7	12.8	0	0	0	0	0	0		100	2	0.03	0.01	0.04
US1	63.1	16.9	20	0	0	0	0	0	0		100	0.31	0.08	0.26	0.34
US4	55	27.9	17.1	0	0	0	0	0	0		100	0.32	0.06	0.19	0.25
US10	51	32.3	11.5	0	3.1	0	2.1	0	0		100	6.4	0.017	0.003	0.02
US12	65.6	11.5	22.3	0	0	0	0.6	0	0		100	6.28	0.19	0.03	0.22
Mean	46	27.6	15	4.8	1.8	0	0.4	4.4	0		100	2.6	0.2	0.2	0.4
Sandstone suite 3 (n = 24)															
H6	52.9	7.5	32.1	0	0	0	0	0	7.5	0	100	3	0.04	0.01	0.05
H9	11	61	23	0	0	0	0	0	5	0	100	1.88	0.05	0.03	0.08
D3	37.8	24.8	31.5	0	0	0	0	0	5.9	0	100	7.3	0.12	0.02	0.14
D5A	5.1	8.8	1.5	0	84.6	0	0	0	0	0	100	23	0.11	0.01	0.12
D10	36.1	9	14.1	0	40	0	0	0	0.8	0	100	6.6	0.36	0.06	0.42
D19	4.9	36.2	8.2	0	3.3	0	1.6	0	45.8	0	100	1.11	0.05	0.04	0.09
D23	5.7	26.4	15.1	0	22.6	0	0	0	30.2	0	100	0.68	0.04	0.06	0.1
DMZ1	51.8	11.2	33	0	3.1	0	0	0	0.9	0	100	39	0.16	0.01	0.17
DMZ10	23.7	45	20.6	0	8.8	0	0	0	1.9	0	100	10.5	0.07	0.01	0.08
DMZ12	56.5	9.7	26	0	3.9	0	0	0	3.9	0	100	22	0.18	0	0.03
DMZ13	23.9	47	15.5	0	9.7	0	0	0	3.9	0	100	9.1	0.14	0.02	0.16
TB1	2.1	24.5	6.4	0	16	0	0	0	51	0	100	4.7	0.07	0.01	0.08
TB4	24	15	6	9	12	0	0	0	34		100	1.5	0.02	0.01	0.03

Heavy minerals and ratios	Zrn	Tur	Rt	Ap	Ant	St	Sa	Brt	Grt	Zo	TtHM	Tran./ opaq	Tranwt %	Opaq (wt%)	THMC (wt%)
TB9	1.9	15.5	3.4	3.4	10.3	0	0	0	65.5	0	100	1.8	0.2	0.11	0.31
AM1	10.4	15.3	12.9	1.2	2.5	0	0	0	57.1	0.6	100	2.47	0.16	0.07	0.23
AM5	38.2	22.8	16.2	1.2	13.2	0	3	0	5.4	0	100	3.2	0.14	0.05	0.19
AM8	19.3	38.1	16.9	2.4	18.7	0	1.2	0	3.4	0	100	2	0.11	0.06	0.17
BT2	10.9	38.8	14.7	5.4	24	0	0.8	0	5.4	0	100	2.34	0.06	0.03	0.09
RS3	10.3	5.1	15.4	2.6	51.2	0	0	0	10.3	5.1	100	0.44	0.04	0.09	0.13
RS5	40	0	20	0	10	0	20	0	10	0	100	0.59	0.03	0.01	0.04
RS11	0.7	0.7	0.7	0	36.3	0	61.6	0	0	0	100	5	0.16	0.03	0.19
KH1	0.5	0.5	0.5	0.5	1	0	2	0	0	95	100	25.7	0.6	0.02	0.62
KH2	25.5	0.7	2.2	0	16.7	0	1.5	53.4	0	0	100	14	1.32	0.09	1.41
KH4	30	0	0	0	60	0	0	10	0	0	100	0.06	0.005	0.065	0.07
Mean	21.7	19.2	14	1.1	18.7	0	3.8	2.6	14.5	4.4	100	7.83	0.18	0.04	0.21
Sandstone suite 4 (n = 11)															
TB13KG	26.7	41.8	1.2	5.8	2.4	0	17.4	0	4.7	0	100	1.6	0.08	0.02	0.1
K1	39.6	43.4	11.3	0	5.7	0	0	0	0	0	100	0.5	0.09	0.09	0.18
K3	19.7	57.9	14.9	0	7.5	0	0	0	0	0	100	0.91	0.11	0.13	0.24
K6	15.9	74.6	3.2	0	6.3	0	0	0	0	0	100	1.13	0.03	0.03	0.06
HM8	48.5	24.3	7.8	0	19.4	0	0	0	0	0	100	2.94	0.16	0.06	0.22
R1	63.5	11.4	11.4	0	9.1	2.3	2.3	0	0	0	100	1.16	0.18	0.18	0.36
R4	13.4	73.1	6	0	6	1.5	0	0	0	0	100	1.16	0.03	0.02	0.05
R9	39.1	43.6	14.1	0	1.6	1.6	0	0	0	0	100	1.25	0.04	0.03	0.07
J25	19.6	67.9	8.9	0	0	1.8	0	1.8	0	0	100	1.4	0.04	0.02	0.06
BF1	47.7	17.3	29.3	0	0	1.7	0	0	0	0	100	0.55	0.05	0.1	0.15
BF10S	37.7	49.5	11	0	0.9	0.9	0	0	0	0	100	1.58	0.07	0.04	0.11
Mean	34.6	42.3	11.4	1.2	3.5	1.5	3.9	0.7	0.9	0	100	1.3	0.08	0.1	0.1

Zrn – zircon, Tur – tourmaline, Rt – rutile, Ap – apatite (detrital and authigenic), Ant – anatase (detrital and authigenic), St – staurolite, Sa – saussurite, Brt – barite (authigenic), Grt – garnet, Zo – zoisite (authigenic), TtHM – total transparent heavy minerals, Tran – transparent heavy minerals, Opaq – opaque heavy minerals, THMC – total heavy mineral concentration in rock wt.%.

## Supplementary Table 4

Correlation coefficients matrix of major elements, the characteristic trace, rare-earth elements, modal mica, opaque heavy minerals. The significant correlation coefficient value at the 95% significance level is  $\geq 0.26$  ( $n = 58$ ).

	SiO <sub>2</sub>	Al <sub>2</sub> O <sub>3</sub>	Fe <sub>2</sub> O <sub>3</sub>	CaO	MgO	Na <sub>2</sub> O	K <sub>2</sub> O	TiO <sub>2</sub>	P <sub>2</sub> O <sub>5</sub>	Ba	Co	Cr	Cs	Ga	Hf	Nb	Ni	Pb	Rb
SiO <sub>2</sub>	1.00	-0.95	-0.82	-0.43	-0.81	-0.73	-0.86	-0.60	-0.04	-0.80	-0.47	-0.64	-0.80	-0.59	-0.33	-0.44	-0.70	-0.42	-0.86
Al <sub>2</sub> O <sub>3</sub>	-0.95	1.00	0.81	0.17	0.69	0.71	0.87	0.59	0.02	0.80	0.53	0.63	0.86	0.63	0.28	0.47	0.73	0.42	0.90
Fe <sub>2</sub> O <sub>3</sub>	-0.82	0.81	1.00	0.17	0.77	0.52	0.61	0.44	-0.01	0.52	0.58	0.63	0.87	0.62	0.14	0.41	0.77	0.29	0.71
CaO	-0.43	0.17	0.17	1.00	0.51	0.26	0.26	0.11	0.15	0.37	-0.04	0.10	0.02	0.12	0.10	0.00	0.06	0.16	0.19
MgO	-0.81	0.69	0.77	0.51	1.00	0.61	0.51	0.31	-0.03	0.51	0.30	0.50	0.64	0.48	0.11	0.15	0.54	0.21	0.55
Na <sub>2</sub> O	-0.73	0.71	0.52	0.26	0.61	1.00	0.62	0.33	-0.01	0.58	0.17	0.40	0.53	0.42	0.17	0.13	0.42	0.29	0.59
K <sub>2</sub> O	-0.86	0.87	0.61	0.26	0.51	0.62	1.00	0.61	-0.01	0.94	0.42	0.54	0.67	0.50	0.38	0.46	0.60	0.46	0.95
TiO <sub>2</sub>	-0.60	0.59	0.44	0.11	0.31	0.33	0.61	1.00	-0.03	0.54	0.45	0.74	0.50	0.36	0.86	0.75	0.52	0.40	0.58
P <sub>2</sub> O <sub>5</sub>	-0.04	0.02	-0.01	0.15	-0.03	-0.01	-0.01	-0.03	1.00	0.09	0.00	-0.07	-0.02	-0.01	-0.05	0.00	-0.03	0.04	-0.01
Ba	-0.80	0.80	0.52	0.37	0.51	0.58	0.94	0.54	0.09	1.00	0.23	0.47	0.58	0.50	0.42	0.25	0.49	0.44	0.85
Co	-0.47	0.53	0.58	-0.04	0.30	0.17	0.42	0.45	0.00	0.23	1.00	0.42	0.59	0.51	0.14	0.77	0.83	0.17	0.56
Cr	-0.64	0.63	0.63	0.10	0.50	0.40	0.54	0.74	-0.07	0.47	0.42	1.00	0.67	0.48	0.51	0.55	0.63	0.37	0.55
Cs	-0.80	0.86	0.87	0.02	0.64	0.53	0.67	0.50	-0.02	0.58	0.59	0.67	1.00	0.81	0.21	0.47	0.80	0.37	0.81
Ga	-0.59	0.63	0.62	0.12	0.48	0.42	0.50	0.36	-0.01	0.50	0.51	0.48	0.81	1.00	0.19	0.48	0.63	0.27	0.70
Hf	-0.33	0.28	0.14	0.10	0.11	0.17	0.38	0.86	-0.05	0.42	0.14	0.51	0.21	0.19	1.00	0.47	0.24	0.26	0.30
Nb	-0.44	0.47	0.41	0.00	0.15	0.13	0.46	0.75	0.00	0.25	0.77	0.55	0.47	0.48	0.47	1.00	0.56	0.29	0.57
Ni	-0.70	0.73	0.77	0.06	0.54	0.42	0.60	0.52	-0.03	0.49	0.83	0.63	0.80	0.63	0.24	0.56	1.00	0.37	0.69
Pb	-0.42	0.42	0.29	0.16	0.21	0.29	0.46	0.40	0.04	0.44	0.17	0.37	0.37	0.27	0.26	0.29	0.37	1.00	0.44
Rb	-0.86	0.90	0.71	0.19	0.55	0.59	0.95	0.58	-0.01	0.85	0.56	0.55	0.81	0.70	0.30	0.57	0.69	0.44	1.00
Sc	-0.77	0.80	0.85	0.03	0.57	0.41	0.63	0.70	-0.07	0.48	0.79	0.75	0.84	0.62	0.37	0.75	0.83	0.33	0.74
Sr	-0.16	0.11	0.07	0.28	0.12	0.09	0.12	0.13	0.33	0.23	0.14	0.09	0.27	0.67	0.17	0.27	0.15	0.14	0.26
Ta	-0.41	0.44	0.38	-0.02	0.13	0.10	0.44	0.73	0.01	0.22	0.74	0.54	0.43	0.43	0.46	0.99	0.53	0.26	0.54
Th	-0.24	0.27	0.28	-0.04	0.01	-0.02	0.32	0.42	0.03	0.08	0.72	0.16	0.23	0.26	0.16	0.86	0.40	0.16	0.43
U	-0.35	0.37	0.34	0.00	0.08	0.05	0.41	0.62	0.07	0.18	0.73	0.29	0.32	0.31	0.39	0.92	0.47	0.23	0.50
V	-0.77	0.80	0.85	0.03	0.57	0.41	0.63	0.70	-0.07	0.48	0.79	0.75	0.84	0.62	0.37	0.75	0.83	0.33	0.74
Y	-0.40	0.33	0.23	0.29	0.21	0.26	0.39	0.63	0.13	0.40	0.26	0.44	0.42	0.65	0.63	0.52	0.35	0.28	0.45
Zn	-0.58	0.64	0.68	0.03	0.51	0.39	0.48	0.44	-0.05	0.45	0.67	0.61	0.81	0.86	0.20	0.51	0.77	0.26	0.64
Zr	-0.31	0.26	0.13	0.10	0.11	0.16	0.37	0.85	-0.06	0.42	0.15	0.51	0.20	0.21	1.00	0.46	0.25	0.25	0.30
La	-0.46	0.43	0.32	0.12	0.20	0.16	0.54	0.84	0.06	0.52	0.39	0.59	0.45	0.50	0.80	0.69	0.42	0.32	0.57
Ce	-0.46	0.43	0.31	0.14	0.21	0.18	0.54	0.84	0.06	0.54	0.34	0.64	0.44	0.49	0.82	0.65	0.42	0.32	0.55
Nd	-0.47	0.43	0.30	0.17	0.22	0.21	0.53	0.83	0.09	0.57	0.30	0.59	0.45	0.52	0.83	0.59	0.40	0.33	0.55
Yb	-0.32	0.25	0.18	0.27	0.19	0.21	0.30	0.54	0.04	0.33	0.20	0.40	0.39	0.69	0.59	0.45	0.29	0.24	0.38
Lu	-0.35	0.28	0.20	0.26	0.19	0.22	0.33	0.61	0.03	0.35	0.22	0.44	0.40	0.68	0.64	0.50	0.31	0.26	0.40
ΣREE	-0.46	0.42	0.30	0.17	0.22	0.20	0.53	0.83	0.08	0.54	0.34	0.61	0.45	0.54	0.82	0.64	0.41	0.33	0.56
ΣLREE	-0.46	0.43	0.31	0.15	0.21	0.19	0.54	0.84	0.07	0.55	0.34	0.62	0.45	0.51	0.82	0.65	0.42	0.33	0.56
ΣHREE	-0.38	0.31	0.22	0.27	0.20	0.24	0.38	0.63	0.11	0.40	0.24	0.45	0.42	0.66	0.65	0.51	0.34	0.28	0.44
Eu/Eu*	-0.09	0.16	-0.03	0.07	0.02	0.14	0.14	-0.39	0.13	0.16	-0.20	-0.24	0.02	-0.12	-0.48	-0.36	-0.15	0.00	0.11
Mca	-0.83	0.79	0.85	0.29	0.89	0.68	0.58	0.34	-0.01	0.55	0.34	0.60	0.80	0.57	0.09	0.15	0.67	0.29	0.63
Opaq	-0.13	0.16	0.19	-0.06	-0.05	-0.09	0.21	0.28	0.05	-0.04	0.63	0.17	0.14	0.18	-0.01	0.79	0.29	0.11	0.32
Grt	-0.27	0.29	0.21	0.04	0.23	0.49	0.32	-0.09	0.17	0.29	0.04	0.04	0.24	0.13	-0.13	-0.12	0.22	0.09	0.29

Mca – modal micas; Opaq – modal opaque heavy minerals, Grt – modal garnet.

## Supplementary Table 5

Correlation coefficients matrix of major elements, the other characteristic trace, rare-earth elements, modal mica, opaque heavy minerals. The significant correlation coefficient value at the 95% significance level is  $\geq 0.26$  ( $n = 58$ ).

	Sr	Ta	Th	U	V	Y	Zn	Zr	La	Ce	Nd	Yb	ΣREE	ΣLREE	ΣHREE	Eu/Eu*	Mca	Opaq	Grt
SiO <sub>2</sub>	-0.16	-0.41	-0.24	-0.35	-0.77	-0.40	-0.58	-0.31	-0.46	-0.46	-0.47	-0.32	-0.46	-0.46	-0.38	-0.09	-0.83	-0.13	-0.27
Al <sub>2</sub> O <sub>3</sub>	0.11	0.44	0.27	0.37	0.80	0.33	0.64	0.26	0.43	0.43	0.43	0.25	0.42	0.43	0.31	0.16	0.79	0.16	0.29
Fe <sub>2</sub> O <sub>3</sub>	0.07	0.38	0.28	0.34	0.85	0.23	0.68	0.13	0.32	0.31	0.30	0.18	0.30	0.31	0.22	-0.03	0.85	0.19	0.21
CaO	0.28	-0.02	-0.04	0.00	0.03	0.29	0.03	0.10	0.12	0.14	0.17	0.27	0.17	0.15	0.27	0.07	0.29	-0.06	0.04
MgO	0.12	0.13	0.01	0.08	0.57	0.21	0.51	0.11	0.20	0.21	0.22	0.19	0.22	0.21	0.20	0.02	0.89	-0.05	0.23
Na <sub>2</sub> O	0.09	0.10	-0.02	0.05	0.41	0.26	0.39	0.16	0.16	0.18	0.21	0.21	0.20	0.19	0.24	0.14	0.68	-0.09	0.49
K <sub>2</sub> O	0.12	0.44	0.32	0.41	0.63	0.39	0.48	0.37	0.54	0.54	0.53	0.30	0.53	0.54	0.38	0.14	0.58	0.21	0.32
TiO <sub>2</sub>	0.13	0.73	0.42	0.62	0.70	0.63	0.44	0.85	0.84	0.84	0.83	0.54	0.83	0.84	0.63	-0.39	0.34	0.28	-0.09
P <sub>2</sub> O <sub>5</sub>	0.33	0.01	0.03	0.07	-0.07	0.13	-0.05	-0.06	0.06	0.06	0.09	0.04	0.08	0.07	0.11	0.13	-0.01	0.05	0.17
Ba	0.23	0.22	0.08	0.18	0.48	0.40	0.45	0.42	0.52	0.54	0.57	0.33	0.54	0.55	0.40	0.16	0.55	-0.04	0.29
Co	0.14	0.74	0.72	0.73	0.79	0.26	0.67	0.15	0.39	0.34	0.30	0.20	0.34	0.34	0.24	-0.20	0.34	0.63	0.04
Cr	0.09	0.54	0.16	0.29	0.75	0.44	0.61	0.51	0.59	0.64	0.59	0.40	0.61	0.62	0.45	-0.24	0.60	0.17	0.04
Cs	0.27	0.43	0.23	0.32	0.84	0.42	0.81	0.20	0.45	0.44	0.45	0.39	0.45	0.45	0.42	0.02	0.80	0.14	0.24
Ga	0.67	0.43	0.26	0.31	0.62	0.65	0.86	0.21	0.50	0.49	0.52	0.69	0.54	0.51	0.66	-0.12	0.57	0.18	0.13
Hf	0.17	0.46	0.16	0.39	0.37	0.63	0.20	1.00	0.80	0.82	0.83	0.59	0.82	0.82	0.65	-0.48	0.09	-0.01	-0.13
Nb	0.27	0.99	0.86	0.92	0.75	0.52	0.51	0.46	0.69	0.65	0.59	0.45	0.64	0.65	0.51	-0.36	0.15	0.79	-0.12
Ni	0.15	0.53	0.40	0.47	0.83	0.35	0.77	0.25	0.42	0.42	0.40	0.29	0.41	0.42	0.34	-0.15	0.67	0.29	0.22
Pb	0.14	0.26	0.16	0.23	0.33	0.28	0.26	0.25	0.32	0.32	0.33	0.24	0.33	0.33	0.28	0.00	0.29	0.11	0.09
Rb	0.26	0.54	0.43	0.50	0.74	0.45	0.64	0.30	0.57	0.55	0.55	0.38	0.56	0.56	0.44	0.11	0.63	0.32	0.29
Sc	0.08	0.73	0.55	0.63	1.00	0.36	0.74	0.36	0.56	0.53	0.49	0.30	0.52	0.53	0.35	-0.24	0.65	0.45	0.05
Sr	1.00	0.24	0.16	0.20	0.08	0.70	0.45	0.19	0.42	0.44	0.49	0.76	0.51	0.46	0.72	-0.11	0.08	0.13	0.02
Ta	0.24	1.00	0.87	0.93	0.73	0.48	0.45	0.45	0.68	0.64	0.58	0.40	0.63	0.64	0.47	-0.36	0.12	0.82	-0.13
Th	0.16	0.87	1.00	0.96	0.55	0.23	0.25	0.15	0.43	0.36	0.31	0.16	0.35	0.37	0.22	-0.25	-0.04	0.93	-0.08
U	0.20	0.93	0.96	1.00	0.63	0.38	0.31	0.37	0.60	0.55	0.50	0.29	0.54	0.55	0.37	-0.32	0.04	0.85	-0.09
V	0.08	0.73	0.55	0.63	1.00	0.36	0.74	0.36	0.57	0.53	0.49	0.29	0.52	0.53	0.35	-0.24	0.65	0.45	0.05
Y	0.70	0.48	0.23	0.38	0.36	1.00	0.53	0.64	0.74	0.76	0.83	0.98	0.83	0.78	1.00	-0.35	0.22	0.12	0.03
Zn	0.45	0.45	0.25	0.31	0.74	0.53	1.00	0.22	0.46	0.45	0.46	0.55	0.48	0.46	0.53	-0.20	0.63	0.18	0.03
Zr	0.19	0.45	0.15	0.37	0.36	0.64	0.22	1.00	0.81	0.82	0.84	0.60	0.82	0.83	0.66	-0.50	0.09	-0.02	-0.13
La	0.42	0.68	0.43	0.60	0.57	0.74	0.46	0.81	1.00	0.98	0.97	0.70	0.98	0.99	0.77	-0.42	0.21	0.31	-0.06
Ce	0.44	0.64	0.36	0.55	0.53	0.76	0.45	0.82	0.98	1.00	0.98	0.71	0.99	1.00	0.78	-0.39	0.23	0.25	-0.04
Nd	0.49	0.58	0.31	0.50	0.49	0.83	0.46	0.84	0.97	0.98	1.00	0.78	1.00	0.99	0.85	-0.39	0.25	0.17	-0.03
Yb	0.76	0.40	0.16	0.29	0.29	0.98	0.55	0.60	0.70	0.71	0.78	1.00	0.80	0.75	0.99	-0.36	0.19	0.09	-0.02
Lu	0.73	0.45	0.19	0.33	0.34	0.98	0.55	0.65	0.74	0.75	0.82	1.00	0.83	0.77	0.99	-0.39	0.19	0.08	-0.06
ΣREE	0.51	0.63	0.35	0.54	0.52	0.83	0.48	0.82	0.98	0.99	1.00	0.79	1.00	1.00	0.85	-0.40	0.24	0.23	-0.03
ΣLREE	0.46	0.64	0.37	0.55	0.53	0.78	0.46	0.83	0.99	1.00	0.99	0.74	1.00	1.00	0.81	-0.40	0.23	0.24	-0.04
ΣHREE	0.72	0.47	0.22	0.37	0.35	1.00	0.53	0.66	0.77	0.78	0.85	0.99	0.85	0.81	1.00	-0.37	0.21	0.10	0.00
Eu/Eu*	-0.11	-0.36	-0.25	-0.32	-0.24	-0.35	-0.20	-0.50	-0.42	-0.39	-0.39	-0.37	-0.40	-0.40	-0.37	1.00	0.05	-0.18	0.40
Mca	0.08	0.12	-0.04	0.04	0.65	0.22	0.63	0.09	0.21	0.23	0.25	0.19	0.24	0.23	0.21	0.05	1.00	-0.09	0.24
Opaq	0.13	0.82	0.93	0.85	0.45	0.12	0.18	-0.02	0.31	0.25	0.17	0.05	0.23	0.24	0.10	-0.18	-0.09	1.00	-0.10
Grt	0.02	-0.13	-0.08	-0.09	0.05	0.03	0.03	-0.13	-0.06	-0.04	-0.03	-0.04	-0.03	-0.04	0.00	0.40	0.24	-0.10	1.00

Mca – modal micas; Opaq – modal opaque heavy minerals, Grt – modal garnet.

## Supplementary Table 6

## Palaeoredox proxies.

Proxy	Ce/Ce*	Pr/Pr*	Ni/Co	V/ (V+NI)	V/Cr	U/Th	Proxy	Ce/Ce*	Pr/Pr*	Ni/Co	V/ (V+NI)	V/Cr	U/Th
Sandstone suite 1 (n = 9)							Sandstone suite 3						
SR1	0.94	1.04	1.09	0.75	2.78	0.06	TB9	1.06	0.91	5.22	0.37	0.35	0.53
SR5	0.92	1.07	b.d.	1	1.2	0.3	AM1	1.01	1.01	3.59	0.71	1.12	0.24
SD1	1.46	0.78	3.57	0.87	0.31	0.06	AM5	1.06	0.96	6.67	0.49	1.05	0.26
SD3	0.61	1.32	b.d.	1	1.05	0.02	AM8	1.07	0.97	4.19	0.65	0.8	0.36
SD7	0.77	1.14	b.d.	1	2	0.15	BT2	1.11	0.95	3.79	0.73	1.45	0.17
SD9	0.77	1.12	b.d.	1	2.1	0.13	RS3	0.98	1.01	5.5	0.79	0.84	0.21
AK2	0.94	1.05	b.d.	1	0.9	0.21	RS5	1	1	4.38	0.76	0.9	0.2
Ak6	0.98	1.03	b.d.	1	1	0.23	RS11	1.02	1	5.79	0.77	0.72	0.22
AK11	0.98	1.03	b.d.	1	1.7	0.26	KH1	0.97	1.02	3.33	0.76	0.8	0.23
Mean	0.94	1.03	4.04	0.57	1.11	0.07	KH2	0.99	1.02	6.88	0.79	0.59	0.19
Sandstone suite 2 (n = 14)							KH4	0.99	1.01	3.38	0.63	0.62	0.22
SR10	0.96	1.01	10	b.d.	b.d.	0.27	Mean	1.01	1.01	3.86	0.71	0.82	0.21
AK15UI	0.94	1.06	b.d.	1	0.5	0.45	Sandstone suite 4 (n = 14)						
UI1	0.98	1.01	b.d.	1	0.5	0.44	TB13KG	1.21	0.89	b.d.	1	0.8	0.14
UI5	0.97	1.02	b.d.	0.64	0.45	0.3	K1	0.91	1.1	7.14	0.67	1	0.28
UI9B	1.01	1.02	b.d.	1	1.3	0.2	K3	0.97	1	b.d.	1	0.5	0.24
UI17	1.07	0.97	10	0.76	0.8	0.38	K6	0.98	1.02	b.d.	1	0.55	0.23
DS1	1.03	0.97	b.d.	1	1.3	0.26	HM8	0.91	1.11	6.67	0.75	0.9	0.27
DS2	1.06	1	b.d.	0.62	0.8	0.22	R1	1	1	1.35	0.63	1.1	0.42
DS6	1.04	0.97	b.d.	0.75	1.8	0.54	R4	0.95	1.05	b.d.	1	0.6	0.4
DS15	0.96	1.05	3.6	0.4	0.3	0.59	R9	0.95	1.02	b.d.	1	0.5	0.46
US1	1.07	0.99	7.14	0.58	0.35	0.28	J25	0.98	1	b.d.	b.d.	b.d.	0.38
US4	1.1	0.96	b.d.	b.d.	b.d.	0.31	BF1	0.9	1.06	6.25	0.91	0.83	0.27
US10	1.04	1.03	b.d.	0.53	0.4	0.32	BF10S	0.95	1.02	7.14	0.91	1.02	0.21
US12	1.02	1.01	b.d.	0.36	0.25	0.24	Mean	0.97	1.02	3.12	0.67	0.91	0.28
Mean	1	1.03	6.6	0.6	0.63	0.33	Mudstone suite (n = 12)						
Sandstone suite 3 (n = 24)							H1 mud	0.94	1.04	41.48	0.59	1.17	0.37
H6	1.01	1	2.63	0.7	1.08	0.26	BT6mud	0.99	1.09	6.73	0.81	0.96	0.23
H9	1.03	1.01	6.88	0.69	1.2	0.21	LOM28	n.d.	n.d.	1.07	0.94	n.d.	n.d.
D3	1.02	1	4.29	0.74	0.83	0.2	MOM12	n.d.	n.d.	2.07	0.83	n.d.	n.d.
D5A	1.03	0.99	3.81	0.77	0.54	0.19	LS8	n.d.	n.d.	1.45	0.73	n.d.	n.d.
D10	1.01	1.01	4.23	0.73	0.6	0.18	PTAK1	n.d.	n.d.	1.76	0.88	n.d.	n.d.
D19	1.04	0.97	5.63	0.64	0.8	0.23	TM7	n.d.	n.d.	2.47	0.73	n.d.	n.d.
D23	1.01	1	5	0.63	0.85	0.22	TMK40	n.d.	n.d.	0.93	0.8	n.d.	n.d.
DMZ1	1.01	1.01	3.33	0.75	0.83	0.18	TAR13	n.d.	n.d.	1.14	0.78	n.d.	n.d.
DMZ10	1.03	0.97	5	0.65	0.65	0.4	JH17	n.d.	n.d.	0.47	0.86	n.d.	n.d.
DMZ12	1.02	1	3.93	0.72	0.7	0.2	JA10B	n.d.	n.d.	1.14	0.81	n.d.	n.d.
DMZ13	1.02	1.01	3.1	0.76	0.93	0.21	CrZ7	n.d.	n.d.	0.46	0.8	n.d.	n.d.
TB4	0.97	1.03	3.13	0.72	1.08	0.3	Mean	0.97	1.07	5.1	0.8	1.07	0.3